Larsen, H.C., Saunders, A.D., Clift, P.D., et al., 1994
Proceedings of the Ocean Drilling Program, Initial Reports, Vol. 152

9. SITE 917[1]

Shipboard Scientific Party[2]

HOLE 917A

Date occupied: 10 October 1993

Date departed: 26 October 1993

Time on hole: 15 days, 23 hr, 30 min

Position: 63°29.500′N, 39°49.665′W

Bottom felt (drill-pipe measurement from rig floor, m): 519.0

Distance between rig floor and sea level (m): 10.89

Water depth (drill-pipe measurement from sea level, m): 508.1

Total depth (from rig floor, m): 1393.9

Penetration (m): 874.9

Number of cores (including cores having no recovery): 110

Total length of cored section (m): 874.90

Total core recovered (m): 454.88

Core recovery (%): 52.0

Oldest sediment cored:
Depth (mbsf): 874.90
Nature: metaclaystone and metasiltstone
Earliest age: unknown; probably late Paleocene–early Eocene
Measured velocity (km/s): 5.4–6.7

Hard rock:
Depth (mbsf): 41.9–820.74
Nature: basalt
Measured velocity (km/s): 5.3

Basement:
Depth (mbsf): 820.74
Nature: basalt
Measured velocity (km/s): 5.3

Comments: Sediments: Core 152-917A-1R to Section 152-917A-6R-1, 14 cm; -102R-3, 77 cm, to -110R; minor amounts of interbedded sediment recovered in basalt.

Principal results: Site 917 is located on the East Greenland Shelf, approximately 50 km from the coast. The site was selected to penetrate deeply into the featheredge of the seaward-dipping reflector sequences (SDRS). The primary objectives at this site were to determine (1) the Paleogene sedimentation and subsidence history of the shelf; (2) the composition, age, and eruption environment of the SDRS; and (3) the nature of the rock types beneath the SDRS.

Lithologic Unit I is a thin layer (0–28.7 mbsf; 3.2 m recovered in Cores 152-917A-1R to -3R) of Quaternary, glaciomarine silt with dropstones, and gravel of probable glaciomarine origin (Fig. 1). The compacted diamicton recovered at Sites 914 through 916 to the east is absent from the thin Quaternary succession cored at this site. The Quaternary rocks unconformably overlie Unit II (28.7–37.7 mbsf; Core 152-917A-4R), which is an upper middle Eocene (CP14A), dark gray, marine, micaceous sandy siltstone with a high content of volcanic glass and basalt fragments. The benthic foraminiferal assemblage within Unit II indicates a paleowater depth of less than 200 m. A basal volcaniclastic conglomerate (Unit III: Cores 152-917A-5R and -6R; 37.7–41.9 mbsf) lies between Unit II and the basaltic flows. Volcaniclastic sandstones (Unit IV) are found intercalated with the basalts in Section 152-917A-22R-1 (183.4 mbsf), and thin clay-rich horizons occur throughout the volcanic sequence. These, like Unit III, are barren of calcareous nannofossils, indicating that they were not deposited under open marine conditions.

Hole 917A reached basaltic basement at 41.9 mbsf. Ninety-one flow units, plus one intrusive sheet, were recognized in the recovered core. The volcanic succession has been divided into three stratigraphic series: an Upper (41.9–183.4 mbsf), Middle (184.1–376.7 mbsf), and Lower Series (376.7–820.7 mbsf). The Upper and Middle Series are separated by a thin (67 cm recovered) fluvial sandstone interval. The lavas of the Upper Series are predominantly olivine basalts and picrites; those of the Middle Series are more evolved basalts and dacites; and the Lower Series comprises basalts and olivine basalts. Pyroclastic units occur within the Middle Series at 188.0 and 375.0 mbsf.

The entire sequence was erupted subaerially, as evidenced by the common presence of red, oxidized flow tops and occasional reddened soil horizons. Strongly vesicular horizons are present. Hyaloclastite breccia at the base of two flows may have been caused by lava flowing into shallow water or over a wet substrate. Morphologically, both aa and pahoehoe flow types are present, with the more massive aa flows predominating in the Middle and Lower Series. Flow thickness tends to increase downhole; the average flow thicknesses are 4.2 m (Upper Series), 8.1 m (Middle Series), and 12.7 m (Lower Series). Several flows exceed 30 m in thickness, and one is more than 50 m thick.

The lavas are mildly to strongly altered. The distribution of zeolites is not systematic, but the assemblage indicates that the temperature did not exceed 120°C. Zeolites are scarce in the Middle Series, perhaps the result of the increased silica content of these lavas. Calcite is a late-stage alteration mineral and may be associated with fracturing and with tilting of the lava pile. The lower 280 m of the volcanic sequence is highly fractured and faulted; one fault (at 576.5 mbsf) is marked by a mylonite zone. Structures within the basalts and intercalated sediments indicate that the lavas dip at approximately 25°; this is consistent with the seismic profiles that show a seaward dip. Geopetal structures in half-filled amygdales, however, consistently show a shallower dip of about 5°, suggesting that hydrothermal activity continued after regional flexuring.

The Upper Series lavas are predominantly olivine basalts and picrites; the main phenocryst phase is olivine. The sequence of phenocryst phases in the Middle and Lower Series is olivine, olivine + plagioclase, olivine + plagioclase + augite (± magnetite), plagioclase + augite + magnetite (in the dacite). Three dacite flows at the base of the Middle Series contain basalt xenoliths, often with lobate margins, and disequilibrium phenocryst assemblages. These suggest that magma mixing has occurred. The dacites are not peraluminous.

The majority of the lavas have high Zr/Nb values (18–50), although six flows from the Middle and Lower Series have ratios of less than 15. The high Zr/Nb values are comparable to those for depleted mid-ocean ridge basalts (MORB), indicating derivation from a MORB-type source. The Upper Series also has low Ba contents and low Ba/Zr values, similar to those of MORBs. The Lower and Middle Series, however, have high Ba/Zr values, indicating interaction between the magmas and continental lithosphere. The Upper Series lavas show no evidence for such contamination.

---

[1] Larsen, H.C., Saunders, A.D., Clift, P.D., et al., 1994. *Proc. ODP, Init. Repts.,* 152: College Station, TX (Ocean Drilling Program).

[2] Shipboard Scientific Party is as given in the list of participants preceding the contents.

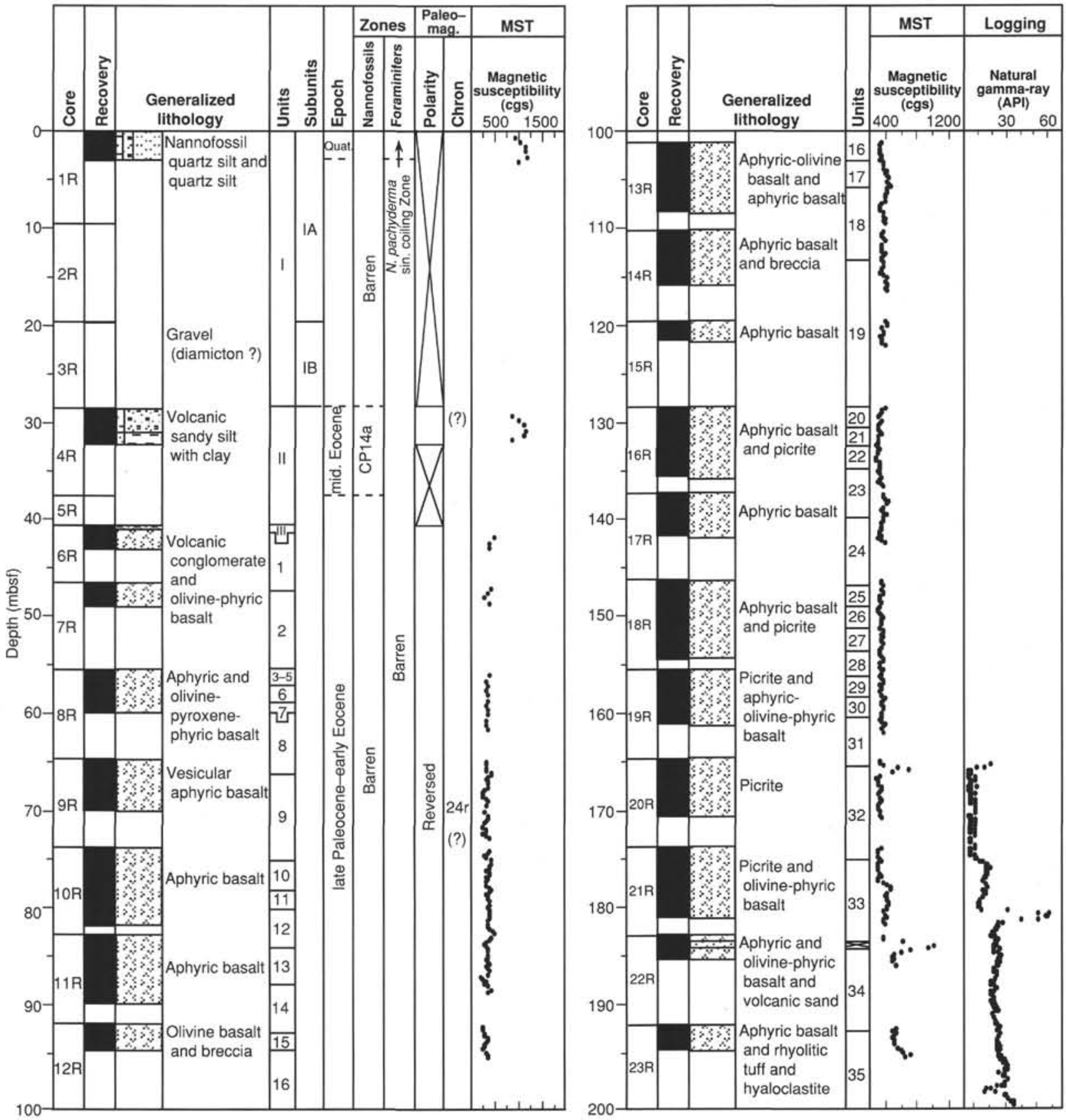

Figure 1. Site summary for Site 917. Note that lithologic Unit IV, comprising several thin sedimentary layers within the basalts, is not shown on this condensed log.

The decrease in the thickness of lava flows, together with the increasing predominance of primitive, picritic, and olivine basalts in the Upper Series, is consistent with the evolution of the magmatic plumbing system. Initially, the magma had long residence times in large magma bodies, but later, the magma traveled rapidly through the crust and was erupted with minimal fractionation.

Underlying the lavas is a thin layer of massive quartzose, coarse-grained sandstone of possible fluviatile or neritic origin (lithologic Unit V; 821.10–821.20 mbsf), of unknown age. Beneath this sandstone, we encountered steeply inclined, low-grade metamorphic, carbonaceous, pyrite-bearing mudstone and sandstone (lithologic Unit VI: 821.2–874.9 mbsf, total depth). Poorly preserved fossils, possibly foraminifers, indicate a marine origin. Trace fossils (*Chondrites*) also indicate deep water (outer shelf?) conditions; bottom conditions may have been euxinic, as indicated by high organic carbon contents (to 4%). The petrography and bulk-rock composition indicate that the rock is, at least in part, of volcaniclastic (basaltic) origin. The steep inclination of the bedding (30° to 90°, with some beds showing overturning) may be related to tilting and slumping associated with pre-SDRS rifting. The age and affinities of this unit are unknown, although some similarities are seen in onshore exposures of Paleocene sediments, such as the Ryberg and Vandfaldsdalen formations in Kangerdlugssuak, East Greenland.

In Hole 917A, paleomagnetic whole-core measurements were obtained only from Core 152-917A-4R, which carries a reverse polarity. Nannoplankton data from this core indicate a CP14a age (middle Eocene); the reverse polarity remanence could represent either Chrons C18r or C19r. Paleomagnetic data were obtained from 76 discrete samples, from 65 of the 92 igneous units. All samples carry a reverse polarity remanence. Stratigraphic arguments, based on the age of the magnetic anomalies in this area, suggest correlation with Chron C24r (upper Paleocene to lower Eocene), but this must await confirmation by shore-based radiometric dating.

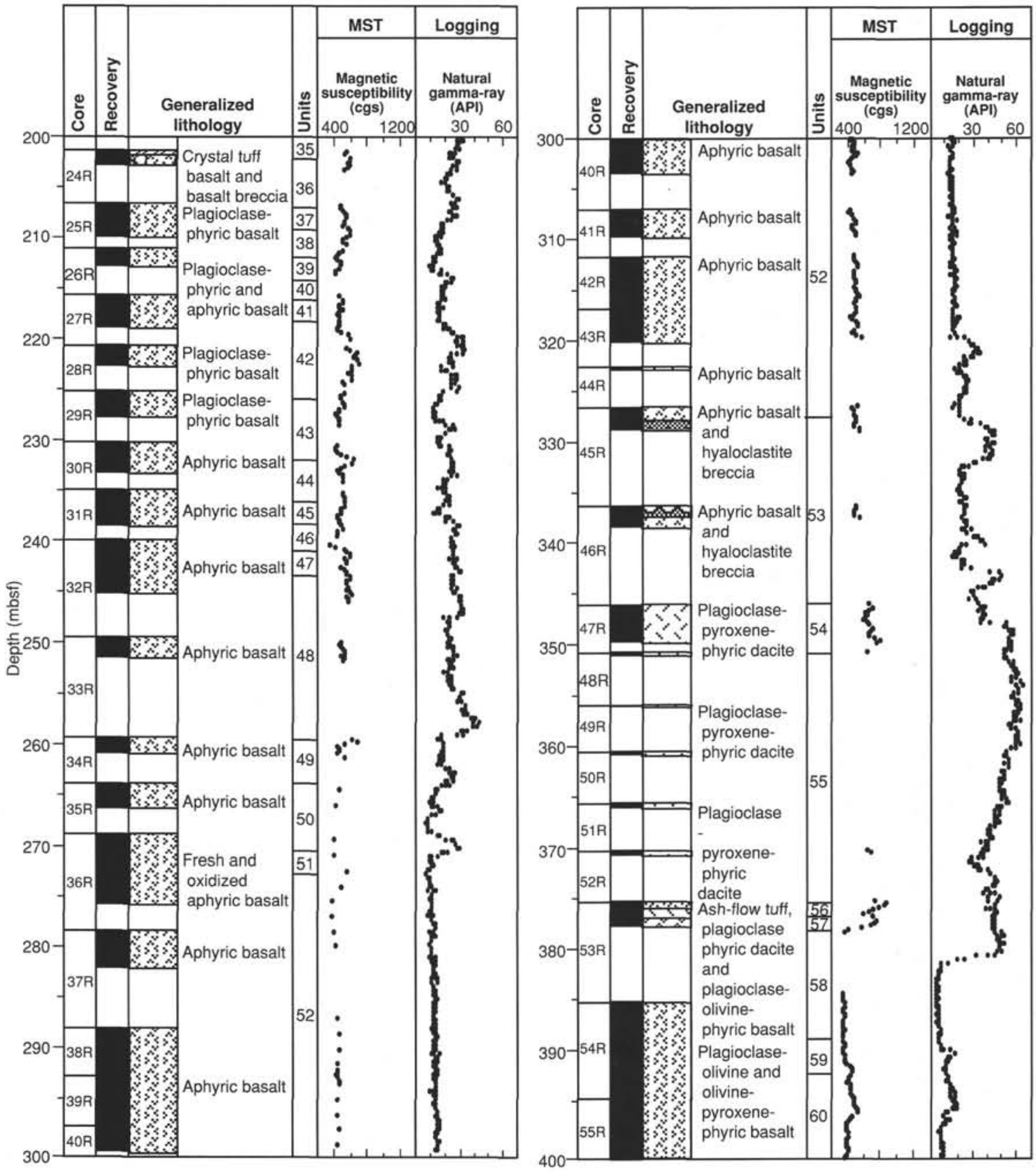

Figure 1 (continued).

Excellent recovery of the basaltic basement has resulted in the generation of a significant database for all the physical-properties measurements. MST data are effective at showing large- and medium-scale variations downhole. The natural gamma signal reflects the gross downcore geochemical trends established by ship-based XRF analysis and downhole logging. MST natural gamma highlights the division between the three series of the basalts: the Upper Series averages 400 TC compared with 500 to 600 TC for the Middle and Lower Series.

More than 100 thermal-conductivity measurements were performed in sedimentary and igneous units. For the soft sediment, full-space thermal-conductivity measurements range between 1.2 and 1.7 W/(m·K). Hard-rock samples were measured using the half-space method. Average thermal conductivities for unaltered basalts range between 1.8 and 2.1 W/(m·K). A broad negative correlation exists between degree of alteration and thermal conductivity.

Hamilton Frame *P*-wave velocity measurements show a wide range (3.0–5.5 km/s) of values in the basalts with significant variations from one flow to another. Velocities of alteration zones and laterites are as low as 2.5 km/s.

The formation microscanner (FMS) and Quad-combo logging tools were deployed successfully in Hole 917A, despite failure of the temperature sonde. The FMS tool provided high-quality image data in the interval from 595.0 to 165.0 mbsf. The differential caliper data show an elliptical hole, with the maximum stress direction along 105°, which is approximately normal to the margin. The synthetic seismogram shows good correlation with the site-survey seismic data. Good correlations also exist between the natural gamma-ray, velocity, resistivity, and caliper logging data and the physical properties and chemical measurements performed on the recovered core. For example, it is possible to distinguish clearly the boundary between the Middle and Lower Series of lavas, to

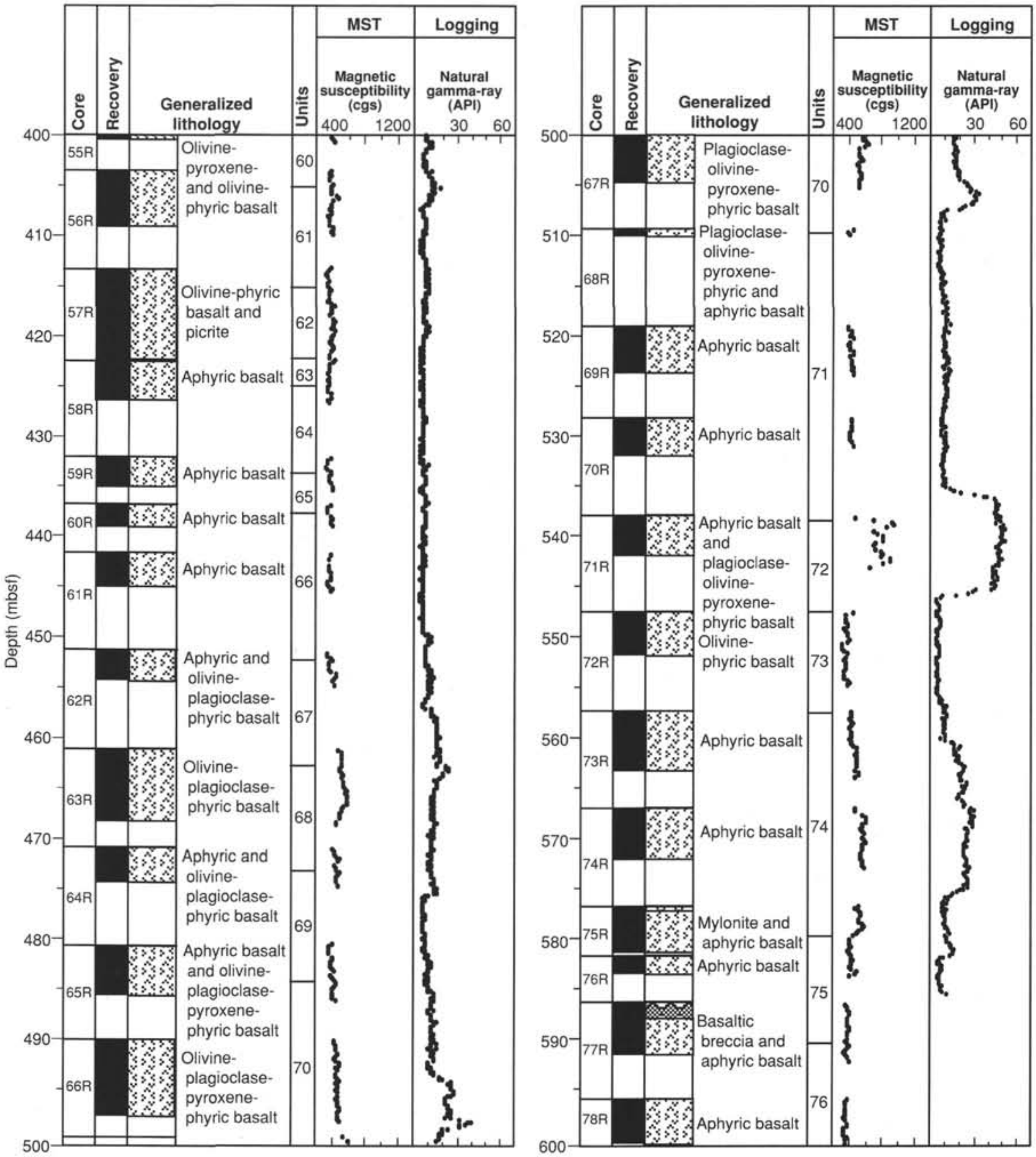

Figure 1 (continued).

distinguish the evolved lavas, and to identify individual units, especially from FMS images.

OPERATIONS

Transit and Hole 917A (EG63-1B)

A Datasonics beacon was recalled and retrieved from Site 916, and the vessel offset in dynamic positioning (DP) mode to a new location approximately 0.5 nmi northwest of Site 916. According to the seismic record, this area contained a thin layer of glaciomarine sediment overlying a thin sandstone layer, which in turn covered basalt. After the vessel stabilized on location, the precision depth recorder depth relative to the dual elevator stool on the rig floor was measured at 517.0 m. A new RBI C-4 (medium hard) bit was fitted to the bottom-hole assembly (BHA), and the drill pipe was run into the water. When Hole 917A was spudded using the rotary core barrel (RCB) at 0400 hr on 10 October, water depth was established relative to driller's datum at 508.1 m.

After the first four cores penetrated glacial till and sediment in approximately 15 hr, the bit contacted basalt at 42 mbsf. This and all coring at Site 917 is documented in Table 1. Surprisingly, the rate of penetration (ROP) increased from 2.3 to 4.3 m/hr as the basalt was penetrated during Core 152-917A-5R. RCB-coring then advanced routinely through basalt and highly altered basalt to a depth of 322.3 mbsf. During the coring of this basalt, the ROP frequently exceeded 5 m/hr, and on two occasions attained 10 m/hr (Cores 152-917A-29R and -32R). On reaching this depth, the core bit had accumulated 68.7 hr of rotation and appeared to be in excellent shape, as indicated by

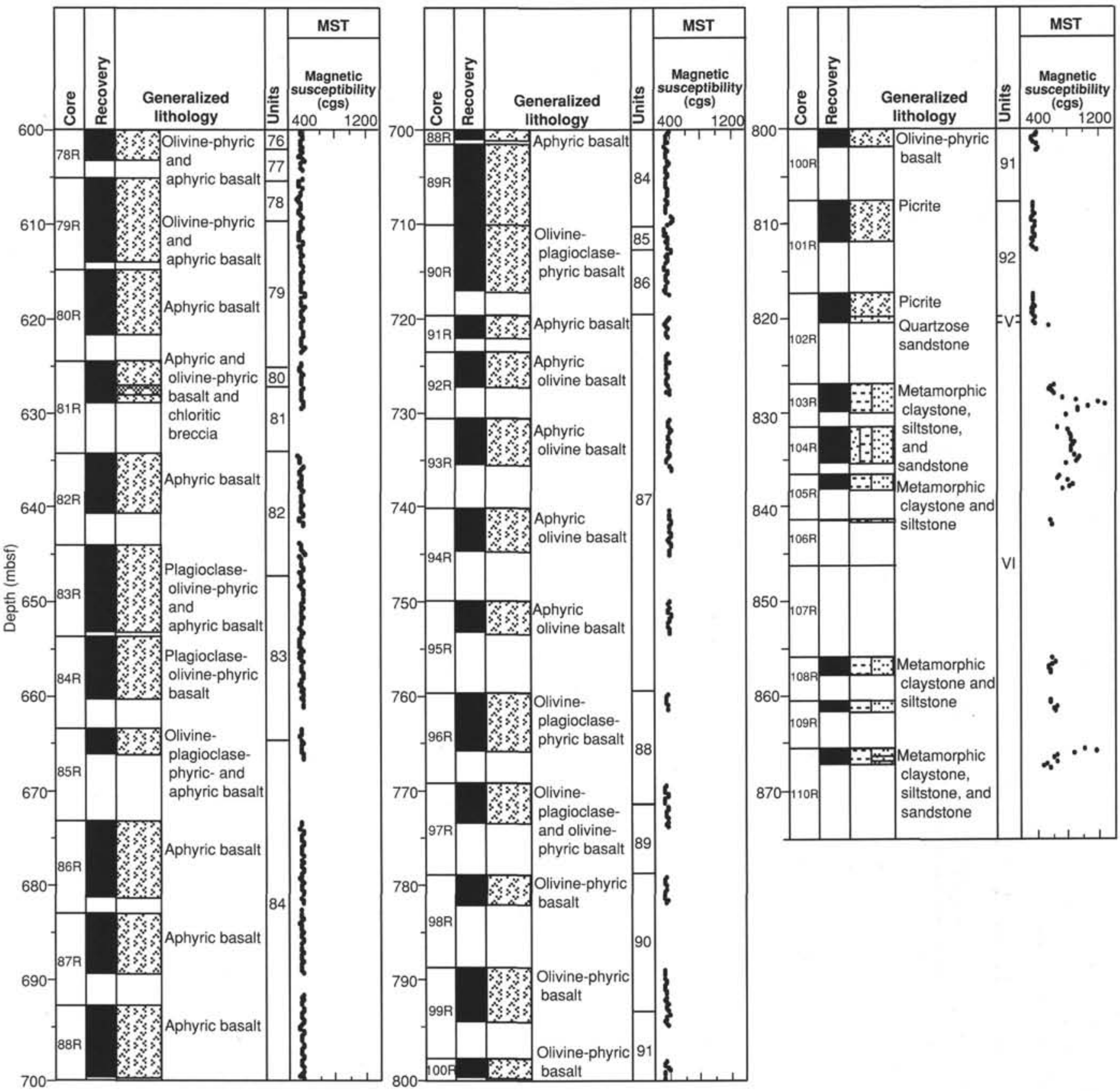

Figure 1 (continued).

uniform torque indications, exceptionally high ROP, and the recovery of full-diameter cores. The bit had penetrated 280 m of basalt with an average ROP of 5.1 m/hr.

Prudence dictated that after such an accumulation of rotating hours, we would be wise to recover the bit, inspect it, and then replace it with a hard-formation-type cutting structure. At 1015 hr on 14 October, the 30-ft knobby was laid down, and the bit pulled up to 91.1 mbsf. During this trip up the hole, little drag was encountered, suggesting that the hole was in excellent condition. The vibration-isolated television (VIT) camera was deployed and lowered to inspect the condition of the top of the hole at the mudline. This inspection revealed that the effluent from the hole had settled uniformly around the top of the hole, making a neat sediment pile that was snug up to the outside of the drill pipe. We had expected that the top of the hole might have been eroded into a large saucer-shaped depression, which would have made the deployment and detection of the free-falling funnel (FFF) difficult. Fortunately, this was not the case, and the VIT was retrieved.

Reentry Number 2, Leg 152

The third FFF of Leg 152 was made up and deployed at 1507 hr. The bit was then pulled out of the hole (POOH) and was on deck at 1700 hr on 14 October. We found it to be in excellent condition, considering that the bit had accumulated 69 hr of rotating time during penetration of 280 m of basalt. The cutting structure of the bit was almost pristine, with no chipped or missing inserts. The jets were not plugged, and the cone bearings were still snug. The bit gauge indicated that the bit was just 1/16 in. under gauge. Based upon the condition of the first bit, we felt that 70 hr rotation was a reasonable expectation of bit life for coring in this basalt.

Table 1. Coring summary, Site 917.

Core	Date (Oct. 1993)	Time (UTC)	Depth (mbsf)	Length cored (m)	Length recovered (m)	Recovery (%)
152-917A-						
1R	10	0730	0.0–9.7	9.7	3.11	32.0
2R	10	1245	9.7–19.7	10.0	0.00	0.0
3R	10	1540	19.7–28.7	9.0	0.06	0.7
4R	10	2015	28.7–37.7	9.0	3.63	40.3
5R	10	2230	37.7–41.7	4.0	0.00	0.0
6R	11	0015	41.7–46.7	5.0	1.42	28.4
7R	11	0300	46.7–55.7	9.0	1.43	15.9
8R	11	0545	55.7–64.8	9.1	4.38	48.1
9R	11	0835	64.8–73.9	9.1	6.30	69.2
10R	11	1115	73.9–82.9	9.0	8.15	90.5
11R	11	1335	82.9–92.0	9.1	6.88	75.6
12R	11	1610	92.0–101.1	9.1	2.90	31.8
13R	11	1915	101.1–110.2	9.1	7.30	80.2
14R	11	2215	110.2–119.4	9.2	5.66	61.5
15R	12	0015	119.4–128.3	8.9	2.14	24.0
16R	12	0215	128.3–137.2	8.9	7.33	82.3
17R	12	0505	137.2–146.1	8.9	4.62	51.9
18R	12	0815	146.1–155.3	9.2	8.33	90.5
19R	12	1125	155.3–164.5	9.2	5.80	63.0
20R	12	1350	164.5–173.6	9.1	5.15	56.6
21R	12	1615	173.6–182.8	9.2	7.43	80.7
22R	12	1805	182.8–191.9	9.1	2.52	27.4
23R	12	2030	191.9–201.0	9.1	2.66	29.2
24R	12	2200	201.0–206.3	5.3	1.59	30.0
25R	12	2300	206.3–210.8	4.5	3.52	78.2
26R	13	0020	210.8–215.3	4.5	1.84	40.9
27R	13	0145	215.3–220.3	5.0	3.47	69.4
28R	13	0315	220.3–224.9	4.6	3.44	74.8
29R	13	0400	224.9–229.9	5.0	2.55	51.0
30R	13	0525	229.9–234.6	4.7	3.09	65.7
31R	13	0630	234.6–239.6	5.0	3.64	72.8
32R	13	1000	239.6–249.2	9.6	5.36	55.8
33R	13	1135	249.2–258.9	9.7	1.94	20.0
34R	13	1320	258.9–263.5	4.6	1.68	36.5
35R	13	1440	263.5–268.5	5.0	2.58	51.6
36R	13	1710	268.5–278.1	9.6	6.87	71.5
37R	13	1955	278.1–287.8	9.7	3.70	38.1
38R	13	2200	287.8–292.4	4.6	5.53	120.0
39R	13	2345	292.4–297.4	5.0	5.64	113.0
40R	14	0330	297.4–307.1	9.7	5.96	61.4
41R	14	0530	307.1–311.7	4.6	2.65	57.6
42R	14	0815	311.7–316.7	5.0	5.17	103.0
43R	14	1050	316.7–322.3	5.6	2.59	46.2
44R	15	0615	322.3–326.3	4.0	0.38	9.5
45R	15	0830	326.3–336.0	9.7	2.19	22.6
46R	15	1105	336.0–345.7	9.7	1.18	12.1
47R	15	1240	345.7–350.3	4.6	3.62	78.7
48R	15	1350	350.3–355.3	5.0	0.16	3.2
49R	15	1500	355.3–360.0	4.7	0.15	3.2
50R	15	1640	360.0–365.0	5.0	0.31	6.2
51R	15	1850	365.0–369.6	4.6	0.55	11.9
52R	15	2045	369.6–374.6	5.0	0.58	11.6
53R	15	2230	374.6–384.3	9.7	2.75	28.3
54R	16	0220	384.3–393.9	9.6	10.02	104.4
55R	16	0530	393.9–403.5	9.6	6.59	68.6
56R	16	0745	403.5–413.2	9.7	5.75	59.3
57R	16	1020	413.2–422.4	9.2	8.98	97.6
58R	16	1320	422.4–432.1	9.7	4.14	42.7
59R	16	1620	432.1–436.7	4.6	2.95	64.1
60R	16	1730	436.7–441.7	5.0	2.11	42.2
61R	16	2030	441.7–451.3	9.6	3.32	34.6
62R	16	2330	451.3–461.0	9.7	3.04	31.3
63R	17	0230	461.0–470.7	9.7	7.21	74.3
64R	17	0600	470.7–480.3	9.6	3.54	36.9
65R	17	0830	480.3–489.9	9.6	5.40	56.2
66R	17	1105	489.9–499.6	9.7	7.73	79.7
67R	17	1440	499.6–509.3	9.7	5.19	53.5
68R	17	1745	509.3–518.9	9.6	0.54	5.6
69R	17	2100	518.9–528.0	9.1	4.70	51.6
70R	17	2330	528.0–537.7	9.7	3.82	39.3
71R	18	0200	537.7–547.3	9.6	4.11	42.8
72R	18	0450	547.3–557.0	9.7	6.82	70.3
73R	18	0700	557.0–566.7	9.7	6.09	62.8
74R	18	0915	566.7–576.3	9.6	5.07	52.8
75R	18	1115	576.3–581.3	5.0	4.79	95.8
76R	18	1330	581.3–585.9	4.6	1.72	37.4
77R	18	1700	585.9–595.5	9.6	5.36	55.8
78R	18	2000	595.5–605.2	9.7	7.81	80.5
79R	18	2300	605.2–614.8	9.6	8.93	93.0
80R	19	0245	614.8–624.5	9.7	6.95	71.6
81R	19	0600	624.5–634.2	9.7	4.30	44.3
82R	19	0830	634.2–643.8	9.6	7.45	77.6
83R	19	1155	643.8–653.5	9.7	9.37	96.6
84R	19	1615	653.5–663.2	9.7	6.78	69.9
85R	20	1530	663.2–672.9	9.7	2.75	28.3
86R	20	1900	672.9–682.1	9.2	8.33	90.5
87R	20	2200	682.1–691.8	9.7	6.95	71.6
88R	21	0200	691.8–701.4	9.6	9.45	98.4
89R	21	0600	701.4–710.1	8.7	8.71	100.0
90R	21	0925	710.1–719.7	9.6	7.19	74.9
91R	21	1035	719.7–723.4	3.7	2.33	63.0
92R	21	1810	723.4–730.4	7.0	4.33	61.8
93R	21	2100	730.4–740.1	9.7	5.33	54.9
94R	22	0000	740.1–749.8	9.7	4.50	46.4
95R	22	0300	749.8–759.4	9.6	3.24	33.7
96R	22	0630	759.4–769.0	9.6	1.36	14.1
97R	22	1005	769.0–778.7	9.7	4.06	41.8
98R	22	1350	778.7–788.4	9.7	2.47	25.4
99R	22	1720	788.4–798.0	9.6	5.91	61.5
100R	22	2015	798.0–807.6	9.6	3.98	41.4
101R	23	2215	807.6–817.3	9.7	4.51	46.5
102R	23	0115	817.3–826.9	9.6	3.13	32.6
103R	24	0400	826.9–831.5	4.6	2.92	63.5
104R	24	0645	831.5–836.5	5.0	4.05	81.0
105R	24	0840	836.5–841.2	4.7	1.76	37.4
106R	24	1025	841.2–846.2	5.0	0.48	9.6
107R	24	1345	846.2–855.8	9.6	0.00	0.0
108R	24	1625	855.8–860.3	4.5	1.66	36.9
109R	24	1900	860.3–865.3	5.0	1.12	22.4
110R	24	2200	865.3–874.9	9.6	1.90	19.8
Coring totals:				874.9	454.88	52.0

At this time, operations were interrupted for 2 hr for the routine task of cutting and slipping 115 ft of drilling line. A new RBI C-7 (hard formation) bit was made up as a mechanical bit release (MBR), the VIT deployed, and the drill string positioned for reentry by 2120 hr. At 2126 hr, the bit reentered the FFF and contacted a hard bridge at 18 mbsf. Before rotating the drill string, the VIT was retrieved, and at 2215 hr, washing and reaming operations were initiated from 18 to 100 mbsf. Approximately 1 hr after reaming began, the bit was able to advance to the bottom of Hole 917A without the need of further rotation. RCB coring resumed in the early hours of 15 October.

RCB-coring advanced from 322.3 to 663.2 mbsf (Cores 152-917A-44R to -84R) in 74.4 hr of rotation. During this interval, 340.9 m of basalt was cored and 182.50 m was recovered (53.5%). The average ROP was 4.6 m/hr, with a high of 12.0 m/hr recorded between 350.3 and 355.3 mbsf. Half interval cores (approximately 5 m) were obtained in zones where highly fractured basalt was encountered to increase the possibility of recovery.

At 1530 hr on 19 October, the top drive was set back and the bit POOH to the surface after the VIT had been deployed and used to verify that the FFF was still visible. The bit was on deck at 1945 hr. Inspection of the used bit verified that the interval of 70 hr was prudent and the type (C-7) was appropriate for coring this highly altered basalt. After the MBR was replaced, the BHA was run to 510.6 m in preparation for reentering the FFF. At this time, operations were terminated as a large iceberg drifted toward the site. This iceberg was measured on radar to be approximately 900 m long by 400 m wide and was seen to be moving in the vessel's direction at 1.4 kt. The iceberg passed the vessel heading south, with the closest point of approach (CPA) measured at 4.8 nmi to the west of location. Its height was estimated to be between 60 and 80 m. A rough calculation of its displacement exceeded 93 million tons.

Reentry Number 3, Leg 152

After a 2-hr delay waiting for this iceberg to pass, the bit reentered the FFF at 0025 hr, 22 October. The bit encountered the same bridge at 18 mbsf that was experienced when changing the first bit. The top drive was kept in place, as the drilling crew had to wash and ream back to the bottom of the hole, because many small bridges were encountered on the way to the bottom of the hole. This frequent washing and reaming protracted the time required to set the bit on the bottom. At 1200 hr, after a chisel deplugger had been dropped and retrieved to ensure that the throat of the bit was clear, coring resumed in Hole 917A.

After coring from 663.2 to 723.4 mbsf (Cores 152-917A-85R to -91R), operations had to be halted because another iceberg was tracked heading toward our location. The top drive was set back and the bit retracted to 393 mbsf. From 1115 to 1200 hr on 21 October, the vessel waited for this large iceberg to pass our location. The iceberg passed west of our location with a CPA of 2.5 nmi. At 1200 hr, the top drive was picked up and the bit washed and reamed to the bottom, where 1 m of fill was detected. After a chisel deplugger had been dropped and retrieved to ensure that the bit throat was clear, coring resumed at 1445 hr on 21 October. RCB-coring advanced with excellent recovery to 807.6 mbsf by 1930 hr on 22 October. A drift survey was conducted at 798 mbsf, and we found that the hole angle deviated from the vertical by 4°.

During the early hours of 22 October, a strong west wind blowing off the Greenland icecap (a local katabatic wind called a *Piteraq* in Greenlandic) drove land-locked ice offshore and toward and past the vessel's location. During the afternoon, many growlers, bergy bits, icebergs, and brash ice were observed in close proximity to the vessel. By evening, one large bergy bit, estimated at 10 m wide and 3 m high, maintained a steady track toward the vessel. By 1930 hr, operations were terminated as once more the drill bit was POOH to a standby position in Hole 917A while the bergy bit was observed. As the drill bit was being POOH to the standby depth, the bergy bit continued to follow a course with a computed CPA to our location of 1 nmi. Safety indicated that the hole had to be vacated, and this was done when the drill bit cleared the seafloor at 2050 hr. The vessel was offset to an ice-free position 2 nmi northeast of our previous location. The bergy bit was tracked by radar and was observed to cross directly over Hole 917A. Because of heavy concentrations of bergy bits of undetermined size that passed our location during darkness, the vessel remained off site until the ice cleared the area.

Reentry Number 4, Leg 152

While standing by for the ice to clear location, the bit was pulled to the surface and another new C-7 bit affixed to the BHA. The MBR was also changed. The vessel reoccupied the site at 0530 hr on 23 October, shortly after which the bit reentered the hole at 1100 hr. After we retrieved the VIT, the bit was rotated past the ledge at 18 mbsf. Hole 917A was then washed and reamed from 18 to 249 mbsf. The top drive was set back, and the drill pipe run in with stands until a bridge was encountered at 509 mbsf, which required that the top drive be picked up. After the hole was washed and reamed from 509 to 807 mbsf, the chisel deplugger was dropped and retrieved.

RCB-coring resumed in Hole 917A at 1845 hr on October 23. At 0300 hr local time, Core 152-917A-103R (826.9–831.5 mbsf) was recovered and found to contain well-lithified dark greenish-gray, laminated volcaniclastic siltstone and sandstone. Coring in Hole 917A apparently had penetrated completely the featheredge of the basaltic SDRS of the East Greenland Margin. Coring continued in this sedimentary material until 2115 hr on 24 October. The total depth of the hole was 874.9 mbsf, of which 779 m were in volcanic rocks.

The hole was flushed with a 40-bbl high-viscosity mud pill. The MBR shifting tool was run in on the wire line, the sleeve was shifted, and the bit was dropped at 2230 hr. The MBR was reset with the second wire-line run; by 2330 hr on 24 October, the pipe was pulled up to logging depth.

Logging Operations

The drill pipe was pulled up to 109.0 mbsf and then run down to 124.0 mbsf. After rigging up the Schlumberger equipment, the first logging run was deployed at 0200 hr. The formation microscanner (FMS) was run in the hole, where it contacted an obstruction at 664 mbsf, which was 211 m above total depth. The hole was logged from 664.0 to 165.0 mbsf, and a good profile of the hole was obtained between 595.0 and 165.0 mbsf. Deviation of the hole was measured at 5° to 6° from vertical. The calipers indicated that a north-south elongation of the hole existed and that numerous cavities were located in the lower part of the borehole wall at about 556 mbsf, as well as in the region between 587 to 581 mbsf. The first logging run was completed by 0700 hr on 25 October.

The second logging run was with the geophysical combination tool without the compensated neutron tool. This tool string was run into the hole at 0700 hr, but it contacted an obstruction at 573.0 mbsf (302 m above total depth). The hole was logged from this depth up to 181.0 mbsf. After the tool was rigged down at 1730 hr, drill pipe was run in the hole in an attempt to clear the bridges, which prevented the logging tools from measuring the bottom of the hole.

Next, the drill pipe was advanced down the hole in stands to a depth of 775 mbsf, where further advance was not possible without rotation. The top drive was picked up, but circulation was not possible because of an apparent blockage in the drill pipe. After several attempts at clearing the obstruction with high pump pressure and a wireline run of the chisel deplugger, the logging program was terminated and pipe was pulled out of the hole.

The BHA was on deck at 0100 hr on 26 October. Nearly 50 m of the BHA was found to be filled with fine-grained basalt cuttings, which had been inhaled while attempting to use the BHA to clear the bridges at the bottom of the hole. After the BHA had been cleared of detritus, the drilling equipment was secured and the beacon recalled. Because of the presence of small bergy bits in the area, which could not be seen on radar, the vessel cautiously offset from this location in DP mode toward Sites 915 and 914 to retrieve beacons before sailing to proposed Site EG63-2 (Site 918).

LITHOSTRATIGRAPHY

Introduction

Site 917 represents the fourth, and most inboard, site in a 6-km-long transect across the central part of the East Greenland Shelf. We divided the recovered sedimentary succession into six lithologic units (Table 2) as follows, in descending order: a Quaternary glaciogenic unit (lithologic Unit I), a middle Eocene volcaniclastic sequence (Unit II), lower Paleogene volcanic conglomerates (Unit III), lower Paleogene volcaniclastic sediment intercalated with basaltic lavas (Unit IV), and a sub-basalt sedimentary sequence (lithologic Units V and VI).

Lithologic Units

Lithologic Unit I: glaciomarine silt with dropstones and gravel
Interval: Sections 152-917A-1R-1, 0 cm, to -3R-1, 7 cm
Depth: 0–28.7 mbsf
Thickness: 28.7 m
Age: Quaternary

This unit has been divided into two subunits: an upper glaciomarine silt with dropstones (Subunit IA), and a lower gravel (Subunit IB).

Lithologic Subunit IA: glaciomarine silt with dropstones
Interval: Sections 152-917A-1R-1 to -1R-CC
Depth: 0–9.7 mbsf
Thickness: 9.7 m
Age: Quaternary

This subunit is made up of three main components: (1) a dominant silty lithology, (2) minor, coarser-grained beds intercalated within the major silty lithology, and (3) gravel.

The dominant silty lithology is composed of, from top to bottom, clayey nannofossil quartz silt mixed sediment (Interval 152-917A-

Table 2. Summary of lithologic units at Site 917.

Lithologic unit	Lithology	Depth (mbsf)	Core intervals	Thickness (m)	Age
I	Glaciomarine silt with dropstones and gravel	0.0–28.7	152-917A-1R-1, 0 cm, to -3R-1, 7 cm	28.70	Quaternary
IA	Glaciomarine silt with dropstones	0.0–9.7	152-917A-1R-1 to -1R-CC	9.70	Quaternary
IB	Gravel	9.7–28.7	152-917A-2R to -3R	19.00	Unknown, presumably Quaternary
II	Volcanic silt with interbeds of calcareous mudstone	28.7–37.7	152-917A-4R-1 to -4R-CC, 10 cm	9.00	late middle Eocene
III	Volcanic conglomerate with reddish mud	37.7–41.9	152-917A-5R to -6R-1, 14 cm	4.20	Unknown
IV	Volcaniclastic rock intercalated with basaltic lava	165.4–165.9, 183.4–184.1, 194.6–195.4, 201.0–202.1, 406.4–406.5, and 453.5–453.6	152-917A-20R-1, 90–140 cm, -22R-1, 60–128 cm, to -23R-2, 120 cm, to -23R-3, 47 cm -24R-1, 0–110 cm, -56R-3, 21–29 cm, and -62R-2, 111–118 cm	0.50 0.68 0.73 1.10 0.08 0.07	Unknown
V	Quartzose sandstone	821.1–821.2	152-917A-102R-3, 76–90 cm	0.14	Unknown
VI	Metamorphosed claystone, siltstone, and sandstone	821.2–874.9 (t.d.)	152-917A-103R-1 to -110R	53.70	Unknown

1R-1, 0–15 cm), nannofossil quartz silt mixed sediment (Interval 152-917A-1R-2, 0–70 cm), and quartz silt with dropstones (Interval 152-917A-1R-2, 110–129, and -1R-3, 25–128 cm). These sediments are very soft and show no bedding. Clayey nannofossil quartz silt includes 25% calcareous nannofossils with foraminifers. Siliceous fossils are dominated by sponge spicules. Diatoms and radiolarians constitute less than 1% of the sediment. The content of biogenic material decreases downcore from a maximum of 50% in the nannofossil quartz silt to 0% in the quartz silt with dropstones.

The minor beds, in the form of four beds intercalated with the dominant lithology, are composed of sandy silt with nannofossils. These beds can be distinguished visually from the dominant lithology by their olive grayish color and coarse-grained size. All the beds contain nannofossils, even if the adjacent dominant beds are barren of them. The boundaries of these beds have been strongly disturbed by drilling.

The coarse fractions of sediment in lithologic Subunit IA consist of 37%–79% quartz, 1%–10% accessory minerals (pyroxene, amphibole), 1%–5% feldspar, and 1%–5% rock fragments. Quartz grains decrease and other components (feldspar, amphibole, pyroxene, and rock fragments) increase downcore.

Dropstones occur only below Section 152-917A-1R-2, 120 cm, and above the base of the unit. They are principally angular, 1 to 4.5 cm in diameter, and include five clasts of basalt, three clasts of dolerite, one clast of granite, and two clasts of quartzite, identified in hand specimens (Table 3). Clearly, Tertiary basalts are an important constituent of these gravels and appear to be more abundant than clasts of metamorphic rocks that presumably were derived from the Precambrian basement exposed to the west of the drill site.

Lithologic Subunit IB: gravel
Interval: Cores 152-917A-2R to -3R
Depth: 9.7–28.7 mbsf
Thickness: 19.0 m
Age: unknown, presumably Quaternary

Only one large drilling fragment of washed gravel was recovered in Core 152-917A-3R, and it was dolerite, 7 cm long, that probably had eroded from onshore Greenland or from submarine outcrops. The associated matrix, if present, presumably was washed out during drilling. This gravel is thought to have originated as an ice-rafted dropstone, or may have originally been associated with the overlying diamicton or with older glacial deposits.

Table 3. Summary of hand specimen descriptions of gravel recovered in lithologic Unit I, Site 917.

Core, section	Depth (cm)	Rock type	Size (cm)
152-917A-			
1R-2	120	Quartzite	1.5 × 2.0
1R-2	128	Basalt	2.0 × 2.5
1R-2	142	Altered basalt	1.0 × 1.8
1R-2	146	Granite	1.0 × 1.0
1R-2	147	Basalt	1.0 × 1.9
1R-2	150	Quartzite	1.5 × 1.8
1R-3	5	Basalt	1.0 × 2.5
1R-3	70	Basalt	1.3 × 2.7
1R-3	126	Dolerite	1.5 × 4.5
1R-3	128	Dolerite	7.0 cm long
1R-3	135	Dolerite	15 cm long
3R-1	0	Dolerite	7.0 cm long

Although nothing was recovered from Core 152-917A-2R, we place the upper boundary of this subunit at the top of the unrecovered interval.

Lithologic Unit II: volcanic silt with interbeds of calcareous mudstone
Interval: Sections 152-917A-4R-1, 0 cm, to -4R-CC, 10 cm
Depth: 28.7–37.7 mbsf
Thickness: 9.0 m
Age: late middle Eocene

The dominant lithology in this unit is a greenish-black, massive, homogeneous volcaniclastic silt. These beds are slightly to moderately bioturbated and contain burrows filled with silty sand and are locally pyrite-cemented. A few planar and wavy laminae disturbed by burrows were observed. Calcareous shell fragments, foraminifers, and nannofossils are rare. The dominant provenance for this sediment is volcanic as it contains altered volcanic glass (15%–35%), basaltic rock fragments (15%–20%), phillipsite (5%–10%), plagioclase feldspar (3%–5%), opaque minerals (3%–5%), and clinopyroxene (1%). Benthic foraminifers from the volcanic silt indicate a shelf environment (0–200 m water depth; see "Biostratigraphy" section, this chapter). The minor lithology in this unit is a moderately bioturbated mudstone cemented with calcite. The mudstone contains 3% quartz, 3% feldspar, and 3%

rock fragments with 90% micritic matrix. The micrite was derived in part from the dissolution of calcareous nannofossils.

Lithologic Unit III: volcanic conglomerate with reddish mud
Interval: Core 152-917A-5R to Section 152-917A-6R-1, 14 cm
Depth: 37.7–41.9 mbsf
Thickness: 4.2 m
Age: unknown, presumably late Paleocene to late middle Eocene

Although nothing was recovered from Core 152-917A-5R, we placed the top of lithologic Unit III at the top of the unrecovered interval. This unit is composed of, from top to bottom, calcite-cemented conglomerate, volcaniclastic conglomerate, and reddish mud. This lithologic unit overlies basalt. The upper conglomerate occurs as one 4-cm subrounded pebble. The lower, volcanic conglomerate has granule- to pebble-sized clasts set in a dusky reddish clayey matrix. All clasts in the conglomerate are basaltic.

Lithologic Unit IV: volcaniclastic sediments intercalated with basaltic lava
Interval: 152-917A-20R-1, 90–140 cm (igneous Unit 32A); 152-917A-22R-1, 60–128 cm (igneous Unit 34A); 152-917A-23R-2, 120 cm, to -23R-3, 47 cm (igneous Unit 35); 152-917A-24R-1, 0–110 cm (igneous Unit 35); 152-917A-56R-3, 21–29 cm (igneous Unit 61); and 152-917A-62R-2, 111–118 cm (igneous Unit 67)
Depth: 165.4–165.9, 183.4–184.1, 194.6–196.4, 201.0–202.1, 406.4–406.5, and 453.5–453.6 mbsf
Thickness: 0.5, 0.68, 0.73, 1.10, 0.08, and 0.07 m
Age: unknown; presumed to be latest Paleocene to early Eocene

Lithologic Unit IV is composed of six intervals of volcaniclastic rocks and weathered horizons intercalated with the volcanic succession of basaltic lava. The beds consist of reddish brown volcaniclastic conglomerate, breccia, lapillistone, sandstone, siltstone, claystone, and tuff. All lithologies are composed predominantly of volcanic fragments with rare siliciclastic fragments.

Volcanic sandy siltstone (Unit 32A "Igneous Petrology" Section, this Chapter) in Interval 152-917A-20R-1, 90–130 cm, has granule- to cobble-sized fragments of basalt in a sandy siltstone matrix. The upper 11 cm has been crudely laminated. A fining-upward sequence occurs at Section 152-917A-22R-1, 60-128 cm (Fig. 2). This sequence (Unit 34A, "Igneous Petrology" section, this chapter) is made up of, from base to top, (1) massive, clast-supported volcaniclastic soft-pebble conglomerate, (2) medium- to very coarse-grained, cross-bedded volcaniclastic sandstone, (3) horizontal, parallel laminated siltstone, and (4) slightly bioturbated, massive claystone. The volcaniclastic conglomerate overlies another volcaniclastic claystone. These intervals appear to be an alluvial sequence from a coarse (channel?) deposit to a fine (overbank?) deposit. A few volcanic claystones occur as reddish weathered rinds on the lava flows in Intervals 152-917A-56R-3, 21–29 cm, and 152–917A-62R-2, 111–118 cm. They were developed in a subaerial environment. The absence of marine fossils and the rare presence of wood fragments suggest that all of the sediments of Unit IV are nonmarine and are pedogenic or alluvial.

Lithologic Unit V: quartz sandstone
Interval: Section 152-917A-102R-3, 76–90 cm
Depth: 821.06–821.20 mbsf
Thickness: 14 cm
Age: unknown

Lithologic Unit V is a thin quartz sandstone bed that lies between the base of the basalt flows and the top of lithologic Unit VI. The sandstone is strikingly different from the bounding units. Contacts above and below the sandstone were not recovered. The sandstone is lithified, and bedding is weakly developed. Thin section studies show that the rock is composed almost entirely of quartz grains, about 95% of which are singular grains and 5% are multiple grains. A few

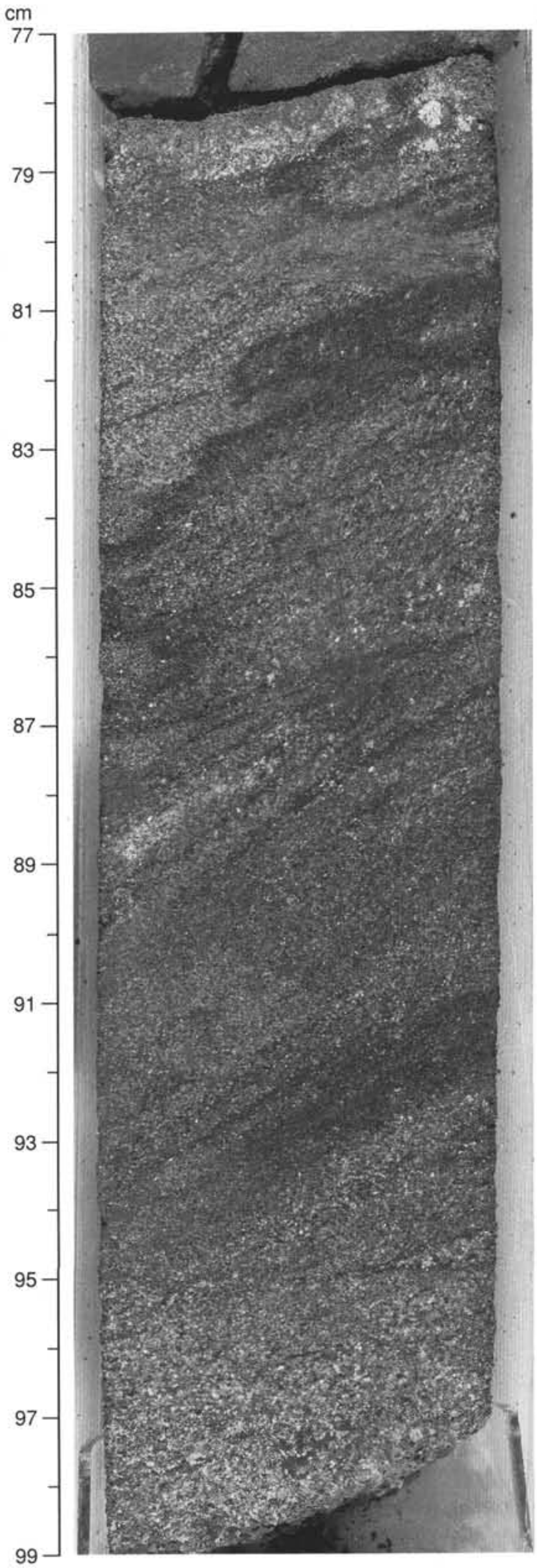

Figure 2. Alluvial sediment intercalated with lava flows (Interval 152-917A-22R-1, 77–99 cm). Pebbles decrease in size from 93 to 98 cm upward and are cross-laminated from 95 to 86 cm. Very fine sediment occurs in the upper centimeter.

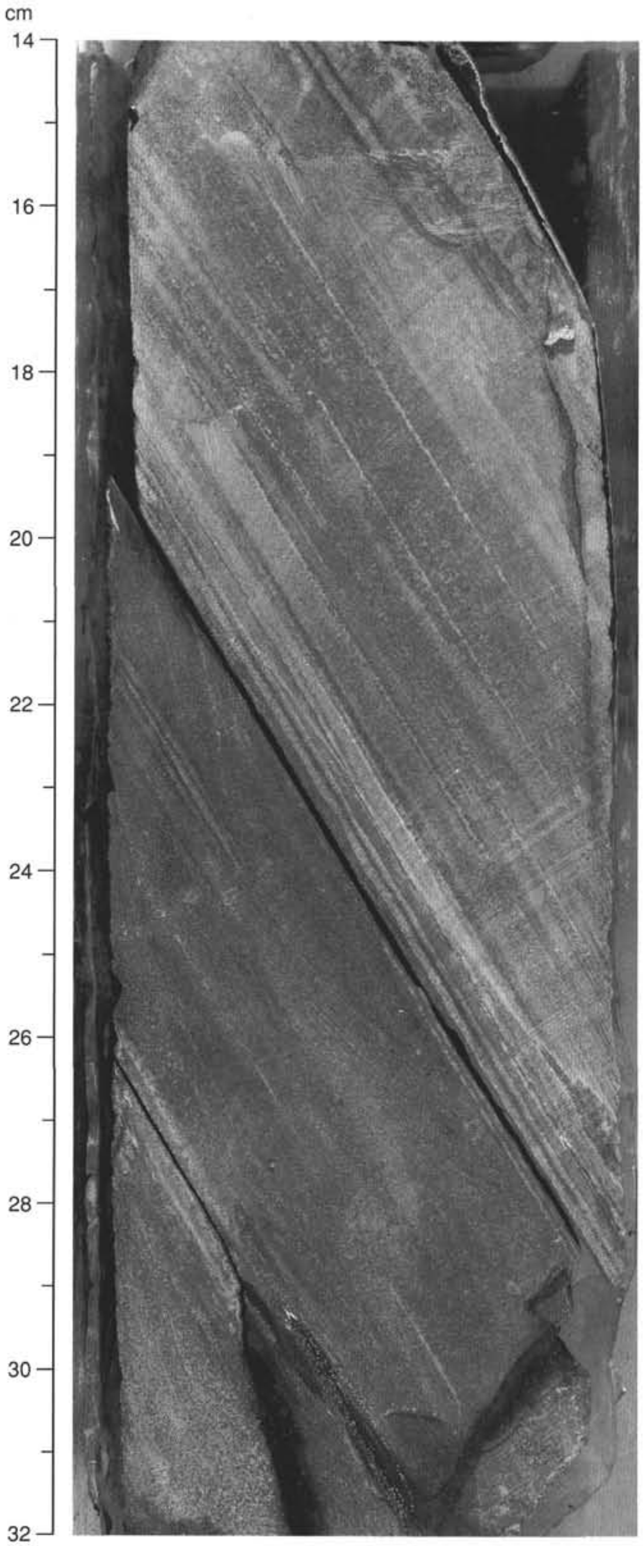

Figure 3. Thinly bedded metaclaystone and metasiltstones (Interval 152-917A-103R-3, 14–32 cm).

multiple grains have sutured internal boundaries. Rusty red clay fills intergranular spaces. The subangular to well-rounded quartz grains are moderately well sorted, and most grains range in size from about 0.5 to 2.0 mm. The maturity of the sandstone implies intense chemical weathering of the source rock region, multiple episodes of transport, or derivation from a mature source area.

The faint bedding in the sandstone dips about 20°, similar to the regional dip of the overlying lavas with which it may be concordant, although it is not known whether or not the dip is in the same direction. The much higher dip of the underlying lithologic Unit VI implies a marked unconformity between lithologic Units V and VI. The depositional environment of lithologic Unit V is not known, and it could be either a marine nearshore facies or a terrestrial fluvial deposit.

The age of lithologic Unit V is not known; however, it may be related to the coarse-grained arkosic sandstone that separates the onshore Late Cretaceous–early Paleocene Ryberg Formation from the slightly younger late Paleocene Vandfaldsdalen Formation, or it might be a unit within the lower parts of the Vandfaldsdalen Formation itself (Soper et al., 1976; Nielsen et al., 1981). Further correlation must await shore-based studies.

Lithologic Unit VI: metamorphosed claystone, siltstone, and sandstone
Interval: Section 152-917A-103R-1 to Core 152-917A-110R
Depth: 821.2–874.9 mbsf
Thickness: 53.7 m (base not recovered, true stratigraphic thickness unknown)
Age: unknown

Lithologic Unit VI is metamorphosed claystone, siltstone, and subordinate sandstone (Fig. 3). The claystone and siltstone beds are thinly laminated with individual laminae that range from 1 to 12 mm. Sandstone beds are as thick as 3 cm. Intense burrowing by *Chondrites* has destroyed most primary bedding features; however, a few beds have ripple marks, cut-and-fill structures, and fining-upward, graded bedding.

Beginning at the top, beds dip at about 30° to 40° in Section 152-917A-103R-1, increasing to 55° to 65° in Section 152-917A-103R-2. Below this interval, beds consistently show very steep to vertical dips. Interpretations of a seismic-reflection profile that crosses near Site 917 (see "Background and Scientific Objectives" section, "Site 914" through "Site 917" chapters, this volume) show that the borehole penetrated the sequence at a point where a shallow-dipping (about 20°) normal fault, flows of the thick basalt unit (in the hanging wall), and sedimentary rocks of lithologic Units V and VI (in the footwall) all meet. This suggests that the dip variation in the beds of lithologic Unit VI, from 30° to 60° within the uppermost 2 m, may occur only close to the fault. If so, the general dip of lithologic Unit VI is somewhere between 65° and 90°.

These rocks were possibly deposited in a marine environment, as suggested by the faint structures in one thin section interpreted as possible relicts of foraminifers. The rocks may have been distal turbidite deposits, based on cut-and-fill features and graded bedding. The absence of retrievable (shipboard) fossils precludes an age determination without further study.

Abundant burrows (*Chondrites*?) are filled with coarser-grained minerals and stand out as both spherical and irregularly shaped forms, with some as long as 1.5 cm. Albite and minor secondary quartz has formed along the edges and chlorite in the middle of some burrows. Other burrows contain albite and minor quartz only. Veins of albite, chlorite, carbonate, and prehnite cut the rocks. Albite/chlorite pseudomorphs of euhedral feldspar laths suggest that feldspar crystals may have been common in some of the coarser grained laminae, and a thin section from one of the coarse-grained siltstones contains chlorite-rich pseudomorphs after mafic(?) volcanic rock fragments.

Studies of 14 thin sections and XRD data from two rocks indicate that the major minerals are albite (5%–50%), secondary quartz (trace–

Table 4. Shipboard X-ray fluorescence major-element analyses of Site 917 sedimentary rocks (lithologic Unit VI).

Core, section, interval (cm)	SiO_2	TiO_2	Al_2O_3	Fe_2O_3	MnO	MgO	CaO	Na_2O	K_2O	P_2O_5	Total	LOI
152-917A-												
103R-1, 54–59	57.95	2.11	17.81	10.91	0.18	4.17	0.43	5.13	0.02	0.00	98.71	4.73
104R-2, 93–95	54.31	2.19	19.18	14.04	0.20	4.25	0.40	3.34	1.37	0.05	99.33	4.45

Notes: Values are in weight percent. LOI = loss on ignition. Analysts were Don Sims and Mary Ann Cusimano.

5%; generally minor and intergrown with albite), and chlorite (5%–35%; clinochlore). Other minerals include epidote, prehnite (estimated 40% in one sample), ilmenite, leucoxene, pyrite, iron-rich carbonate, clay, green biotite (in two samples), and pumpellyite(?). Carbon is common, particularly in the burrows. One sample from the very top of lithologic Unit VI (Sample 152-917A-103R-1, 3–5 cm), contains more than 4% organic carbon. The carbon content decreases irregularly with depth. Major- and trace-element analyses (Tables 4 and 5) reveal high contents of iron, magnesium, titanium, chromium, and nickel and suggest that the original sediments were derived from basic igneous material (e.g., basalt or basaltic tephra). High Na_2O contents combined with low amounts of CaO (Table 4) suggest the replacement of calcic plagioclase by albite. The high (for most sediments) contents of iron and magnesium can be related to the chlorite content of the rocks. The low SiO_2 contents suggest that sediments derived from crystalline Precambrian rocks were not deposited in Unit VI.

Based on the mineral compositions (albite apparently replaced calcic plagioclase and possibly glass; chlorite, biotite, and pumpellyite(?) replaced mafic constituents), oxides of major elements and contents of trace elements (particularly low amounts of SiO_2 and high amounts of MgO, Fe_2O_3, Ni, Cr, and Ti), and textural studies (albite pseudomorphs of plagioclase and chlorite pseudomorphs of probable mafic rock fragments), we presume that the original sediments were derived from a basaltic terrain. From these observations, we tentatively conclude that the rocks were subjected to low-grade metamorphism. There is no tectonic fabric, and the metamorphic minerals have grown without any directional or shear stress. It is unlikely that the rocks of Unit VI were ever buried to a depth that is required by regional greenschist facies metamorphism (2–3 kbar) at normal geothermal gradients. It is more likely that a generally high heat flow led to temperatures similar to those during albite–epidote facies metamorphism. Crustal and lithospheric thinning, in combination with magma storage at depth and proximity to feeder dikes, may all have contributed to a greater regional heat flow.

Summary and Conclusions

Drilling penetrated less than 30 m of a Quaternary glaciogenic unit (lithologic Unit I), constituting an upper glaciomarine, quartz-rich silt with dropstones (lithologic Subunit IA) and a lower gravel of probable glaciogenic origin (lithologic Subunit IB). The relatively thin accumulation of glaciogenic sediment does not include the compacted diamicton found to the east (Sites 914, 915, and 916), and shows that Quaternary sediment thins westward, as predicted by the seismic data. Nannofossils dominate the upper part of Subunit IA, while dropstones occur in the lower part. Lithologic Subunit IA comprises three members: (1) a dominant silty member, (2) four minor sandy beds intercalated with the major member, and (3) gravel.

The Quaternary sediment unconformably overlies upper middle Eocene volcaniclastic sediments (lithologic Unit II). The hiatus extends from the late middle Eocene to the late Pleistocene. Lithologic Unit II is characterized by a high content of volcanic glass and basaltic rock fragments. Benthic foraminifers from the volcaniclastic silt (lithologic Unit II) indicate a shallow marine environment (0-200 m water depth; see "Biostratigraphy" section, this chapter). The Eocene volcaniclastic sequence unconformably overlies a basaltic lava succession that is capped by a basal volcaniclastic conglomerate (lithologic Unit III). Older volcaniclastic sediments (lithologic Unit IV) intercalated with the basaltic flows of the main SDRS were deposited in a nonmarine environment, as evidenced by the absence of marine fossils, the occurrence of wood fragments, red paleosols, and because of the alluvial facies of the sediment. These findings indicate subsidence at Site 917 between latest Paleocene and middle Eocene time.

Table 5. Shipboard X-ray fluorescence trace-element analyses of Site 917 sedimentary rocks (lithologic Unit VI).

Core, section, interval (cm)	Ba	Cr	Nb	Ni	Rb	Sr	V	Y	Zr	Cu
152-917A-										
103R-1, 54–59	56	133	8	96	4	48	655	24	120	5.4
104R-2, 93–95	294	145	9	101	43	33	659	27	123	247

Note: Values are in parts per million. Analysts were Don Sims and Mary Ann Cusimano.

Lithologic Unit VI is a sub-basalt sedimentary sequence that may be correlative to the Late Cretaceous to Tertiary, pre-basaltic sediments exposed onshore from 66° to 75°N along the East Greenland Margin (e.g., Soper et al., 1976; Larsen, 1980; Nielsen et al., 1981). The best exposed sub-basalt sediment sequence occurs near Kangerdlugssuaq (68°N) in East Greenland, where it has been divided into three major formations: Upper Cretaceous Sorgenfri Formation, Upper Cretaceous and early Paleocene (Danian) Ryberg Formation, and late Paleocene (Thanetian) Vandfaldsdalen Formation. At this time, we are not able to correlate lithologic Unit VI directly to any of the rocks reported from East Greenland. The Rydberg Formation seems a possible correlative, but the high content of arkosic material reported by Soper et al. (1976) and Nielsen et al. (1981) casts some doubt on that correlation. The high contents of organic carbon in rocks of the Rydberg Formation, however, are similar to the high contents in rocks from lithologic Unit VI of Hole 917A. The younger part of the Vandfaldsdalen Formation (above the Schjelderup Member) also may be correlative. It contains significant amounts of volcanic rocks, including breccia, hyaloclastite, lava flows, and tuff (Nielsen et al., 1981). In general, the hyaloclastites thicken seaward, and some built seaward-prograding deltas that may be a proximal facies of the siltstones and claystones in lithologic Unit VI. A better attempt at correlation will have to await additional sedimentological and biostratigraphic data.

BIOSTRATIGRAPHY

Calcareous Nannofossils

Three samples from Hole 917A were examined for nannofossils. Sample 152-917A-1R-CC yielded a few specimens of reworked *Coccolithus pelagicus* and a Cretaceous species. A sample from 152-917A-4R-CC contains a small number of nannofossils. Age-diagnostic species found include *Chiasmolithus solitus*, *Reticulofenestra bisecta*, and *R. umbilicus*. This assemblage is indicative of Zone CP14a in the middle Eocene (Fig. 4). Sample 152-917A-6R-1, 12 cm, a sediment layer within the basalt sequence, was examined and found to be barren of nannofossils. This suggests that this sediment layer is not an open-marine deposit.

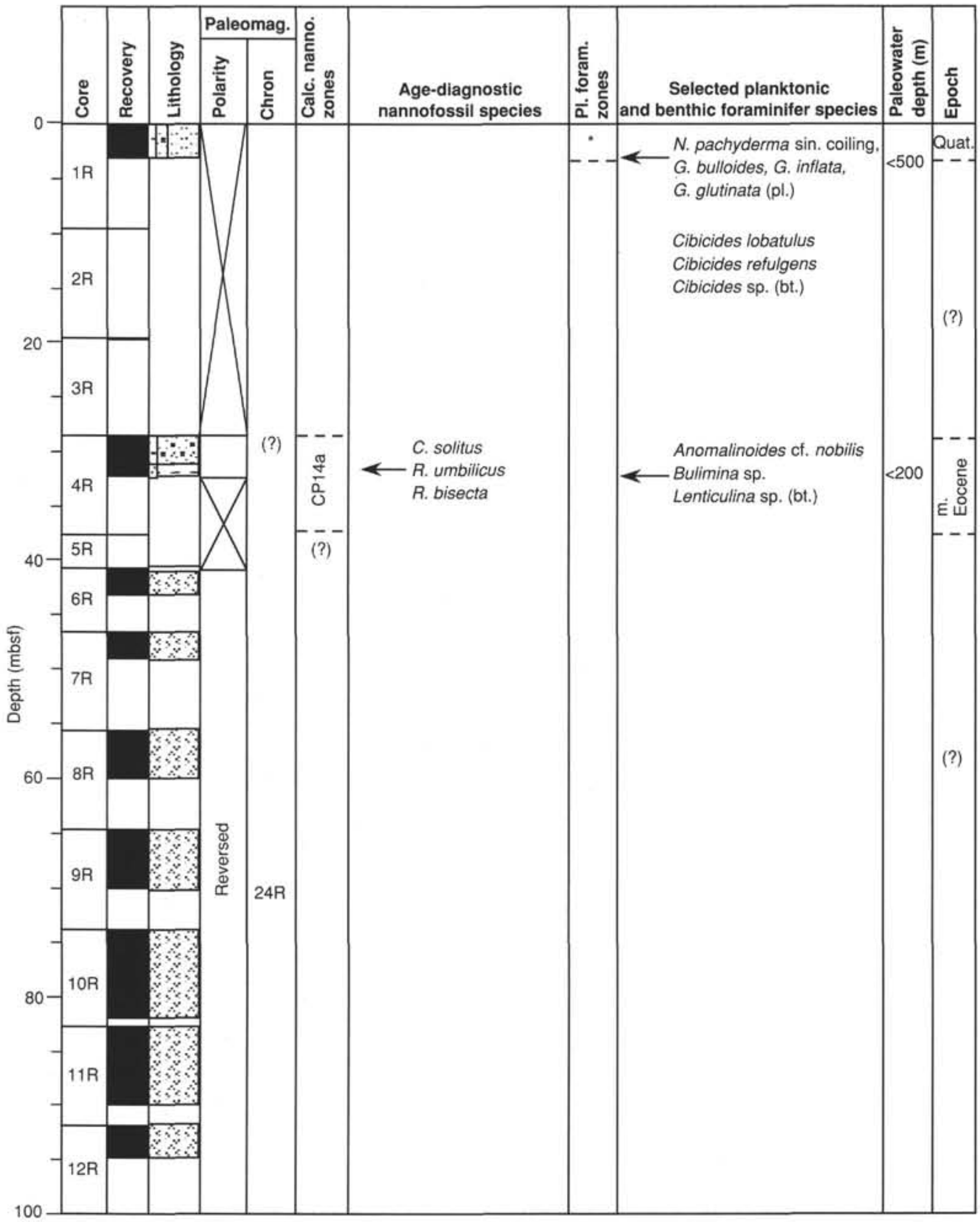

Figure 4. Biostratigraphic summary of Hole 917A. Paleowater depths inferred by benthic foraminiferal species also are shown. pl. = planktonic foraminifers, bt. = benthic foraminifers, * = *N. pachyderma* sinistral-coiling Zone.

Planktonic Foraminifers

Only one sample, Sample 152-917A-1R-CC, was suitable for planktonic foraminifer analysis. It contains moderately preserved and common sinistrally coiled specimens of *N. pachyderma*, along with a few dextrally coiled specimens of *N. pachyderma*, and *G. buloides, G. inflata, G. glutinata, G. juvenilis*, and *Turborotalita quinqueloba*. This assemblage can be attributed to the *N. pachyderma* sinistral-coiling Zone, which ranges from Pleistocene to Holocene (Fig. 4).

Benthic Foraminifers

Benthic foraminifers were identified in Samples 152-917A-1R-CC and -4R-CC. In Sample 152-917A-1R-CC, moderately preserved benthic faunas make up about one-half of the total foraminiferal assemblage. *Cibicides lobatulus*, *Cibicides refulgens*, and *Cibicides* spp. constitute about 70% of the benthic fauna in this section. The species component resembles that found in Samples 152-915A-1R-1, 0–2 cm, and -5R-1, 90–92 cm. They have been interpreted as post-glacial and interglacial faunas, respectively (see "Biostratigraphy" section, "Site 915" and "Site 916" chapters, this volume). The assemblage in Sample 152-917A-1R-CC, therefore, may be a post-glacial or interglacial fauna.

Sample 152-917A-4R-CC contains few, poorly preserved benthic specimens of *Anomalina*(?) sp., *Anomalinoides* cf. *nobilis*, *Bulimina* sp., and *Lenticulina* sp. The combination of *Anomalinoides nobilis* and some species of *Bulimina*, and *Lenticulina* spp. has been reported from some samples of DSDP Holes 552A, 553A, and 555A on the Rockall Plateau in the North Atlantic. The paleowater depth inferred from foraminiferal assemblages in those samples is shallower than

200 m (Murray, 1984). The assemblage in this section, therefore, may also suggest a paleowater depth of 0 to 200 m (Fig. 4).

PALEOMAGNETISM

As a result of poor recovery in the thin sedimentary cover (<42 m) in Hole 917A, paleomagnetic studies of sedimentary rocks were conducted only on Core 152-917A-4R. Initial natural remanent magnetization (NRM) intensities range between 20 and 160 mA/m. Alternating field (AF) demagnetization to 30 mT decreased the intensities typically by 75% of the initial values and isolated a reverse polarity magnetization. Nannoplankton data from this core (see "Biostratigraphy" section, this chapter) indicate an age of CP14a (late middle Eocene). Thus, the reverse polarity remanence associated with Core 152-917A-4R may represent either Chrons C18r or C19r.

Investigations were conducted on the lavas in Hole 917A to determine their (1) magnetic polarity and (2) magneto-mineralogical variations within the succession. To this end, AF demagnetization of both the NRM and anhysteretic remanent magnetization (ARM) was performed. In addition, bulk magnetic susceptibility was measured. These data are summarized in Table 6.

Paleomagnetic data from the volcanic sequence are based on the analysis of seventy-six 8 cm^3 specimens from Cores 152-917A-6R to -101R (the lavas have NRM intensities that exceed the measuring range of the whole-core cryogenic magnetometer, thus discrete specimens were used in the paleomagnetic analyses). One or more specimens were collected from 65 of the 92 petrologic units recovered during drilling (see "Igneous Petrology" section, this chapter).

Figure 5 is a plot of initial NRM intensity vs. depth. High values (20–48 A/m) were recorded in three samples from the upper part of the lavas succession (152-917A-6R-1, 94–96 cm; -7R-1, 140–143 cm; -10R-5, 121–125 cm). In the interval from 40 to 377 mbsf, corresponding to the Upper and Middle Series defined by petrologists (see "Igneous Petrology" section, this chapter), NRM intensities are 3.5 ± 2.0 A/m. The lower part of the sequence (377–820 mbsf: Lower Series) is characterized by relatively low intensities (2.0 ± 1.5 A/m). A large amount of scatter (± 2.9 A/m) is noteworthy in the upper 100 m of the Lower Series (377–477 mbsf); stable magnetic directions could not always be determined within this interval (see below).

The NRM was then AF demagnetized, typically to 80 or 100 mT, and the response was analyzed from Zijderveld (1967) plots of the data. Samples from Cores 152-917A-6R to -43R carry a single component of magnetization (see Fig. 6A). Below this core, samples carry an additional secondary remanence, which is considered to be a drilling-induced or viscous component. This overprinting was typically removed by the 20 mT demagnetization (see Fig. 6B), however, in some cases, fields of up to 60 mT were required. The low coercivity component is downward and is steep to subvertical. Typically, it amounts to about 20% to 40% of the initial NRM. Characteristic directions were determined using linear regression on at least four successive demagnetization directions (usually in the range of 20–80 mT). In practically all cases, inclinations were negative, indicating a reverse polarity remanence throughout (Fig. 7). This is consistent with the estimated age of the ocean floor in this area (Chron C24r). However, exceptions to this general pattern exist; the inclinations in lava flow Units 61B, 62, and 63 (Cores 152-917A-57R to -58R) are shallow and positive (10° to 30°, see Fig. 6C). Such behavior can be interpreted in two ways. First, assuming that these paleomagnetic directions are primary, the signal might record short-term anomalous geomagnetic field behavior within Chron C24r (e.g., Cande and Kent, 1992). Second, a steep negative primary remanence may be completely masked by a shallow positive high-coercivity, drilling-induced component. Post-cruise studies on samples from this interval will aim to determine the origin of the remanence, and will include thermal demagnetization and geomagnetic paleointensity experiments.

Further interpretation of paleomagnetic inclination data (without any declination control) from Site 917 is problematic. Typically, in a suite of declination-oriented paleomagnetic samples from high latitudes (inclinations >75°), it is likely that declinations will range between 0° and 360°. Thus, before any paleomagnetic-based estimates can be made of both formation latitude and time relations between extrusion and tilting of the lava, samples will have to be oriented about a vertical axis. We anticipate that orientation will be provided by relating core piece fractures to formation microscanner images. However, identifying microtectonic features from the high-resolution downhole logs and then orienting the shipboard paleomagnetic measurements will require several weeks of dedicated effort, which will have to be completed after the cruise.

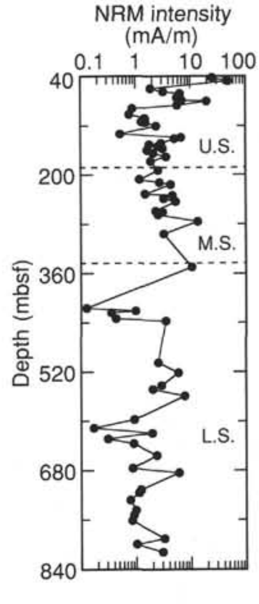

Figure 5. Intensity of NRM plotted vs. depth in Hole 917A. The stratigraphy of the lava succession is shown also (see "Igneous Petrology" section, this chapter). U.S. = Upper Series; M.S. = Middle Series; L.S. = Lower Series.

Several types of magnetic measurements were performed on the volcanic rock samples from Hole 917A to assess the reliability of the NRM data and to establish possible changes in magnetic properties as the lavas accumulated.

The bulk magnetic susceptibility (see Table 6 and Fig. 8) has been measured in low-frequency mode (0.47 kHz). Its mean value is 1.63 $\times 10^{-2}$ SI, which is low compared to that normally associated with oceanic basalts (typically around 2.7×10^{-2} SI; Pariso and Johnson, 1991). We observed a slight decrease in susceptibility with depth (Fig. 8). This behavior is positively correlated with that of the initial NRM intensity values.

The Koenigsberger (1938) ratio (Q ratio, see Table 6 and Fig. 9) is defined as the ratio of a rock's natural remanence to its induced magnetization in the present-day Earth's magnetic field, and can be expressed as

$$Q = (\mu^{\circ} \cdot \mathrm{NRM})/(\chi \cdot H),$$

where μ° = the magnetic permeability, χ = the bulk magnetic susceptibility, and H = the present-day Earth's magnetic field at the sampling locality. The geomagnetic field intensity at Site 917 was estimated to be 54 µT (from Merrill and McElhinny, 1983). The mean value of the Q ratio from the lavas in Hole 917A is 5.4, which indicates that the remanent magnetization dominates the induced magnetization. This, in turn, suggests that the aeromagnetic anomaly data obtained from the area adjacent to Site 917 are a reliable measure of the original magnetic polarity of the ocean floor. No significant variation of Q ratio is seen with depth within the lava pile.

Table 6: Magnetic results obtained using discrete samples from the volcanic pile of Hole 917A.

Core, section, interval (cm)	Piece	Depth (mbsf)	NRM (A/m)	MDF-NRM (mT)	St. inc. (°)	Suscept. (SI)	Q ratio	ARM (A/m)	MDF-ARM (mT)	NRM / ARM	Unit
152-917A-											
6R-1, 94–96	9	42.64	25.00	43.6	–44.2	3.22E–02	18.09	9.34	26.7	2.68	1
7R-1, 140–143	22	48.10	48.23	35.5	–44.7	4.73E–02	23.75	16.71	30.3	2.89	2
8R-4, 14–16	2	60.19	1.87	78.2*	–46.0	8.80E–03	4.95	2.32	19.7	0.81	6
9R-1, 15–19	3	64.95	3.16	36.2	–51.1	1.76E–02	4.19	3.67	ND	0.86	7
9R-3, 58–63	7A	68.19	6.45	28.8	–69.1	2.37E–02	6.33	4.28	ND	1.51	8
10R-1, 66–68	1F	74.56	5.68	23.9	–76.0	2.11E–02	6.27	4.26	ND	1.33	9
10R-4, 52–56	2B	78.57	6.90	29.2	–80.9	2.52E–02	6.36	4.43	ND	1.56	10
10R-5, 121–125	5A	80.76	19.71*	29.1	–79.0	3.20E–02	14.33	7.53	24.6	2.62	11
11R-4, 31–35	1B	87.07	5.75	33.8	–80.3	1.69E–02	7.93	3.29	25.5	1.75	13
12R-1, 35–39	4A	92.35	0.87	20.6	–39.0	1.72E–02	1.18	2.53	10.9	0.35	14
13R-1, 77–81	4	101.87	0.77	30.2	–74.9	7.41E–03	2.41	1.09	17.9	0.70	16
13R-5, 107–111	10	108.06	1.49	29.5	–65.5	6.53E–03	5.31	1.81	12.0	0.82	17
14R-3, 97–101	7	113.62	1.29	31.3	–50.7	6.60E–03	4.54	1.33	13.5	0.97	18
14R-4, 83–88	2A	114.52	1.50	32.7	–52.1	7.31E–03	4.78	1.20	ND	1.26	18
15R-2, 5–9	1A	120.70	2.38	26.2	–68.8	1.05E–02	5.26	2.69	ND	0.88	19
16R-4, 59–63	8A	133.13	0.52	31.8	–46.6	3.38E–03	3.60	0.66	ND	0.79	21
17R-2, 72–76	2	138.89	6.65	28.5	–43.8	3.32E–02	4.67	7.07	ND	0.94	23
17R-4, 73–77	3B	141.42	5.09	27.1	–38.8	2.36E–02	5.03	5.31	ND	0.96	24
18R-3, 32–36	1	148.90	2.93	34.1	–60.8	9.30E–03	7.34	1.85	28.8	1.59	25
18R-4, 95–99	7A	150.94	1.76	19.7	–60.0	1.70E–02	2.41	4.08	14.4	0.43	26
18R-6, 97–101	5A	153.91	2.56	32.3	–61.5	8.86E–03	6.72	2.30	25.5	1.11	27
19R-2, 41–46	1B	157.11	3.13	38.9	–63.6	8.95E–03	8.13	2.18	31.1	1.44	30
19R-4, 44–48	2B	160.03	1.62	39.9	–61.3	6.11E–03	6.17	1.45	30.8	1.11	31
20R-1, 21–26	2B	164.71	2.09	38.5	–62.3	6.35E–03	7.67	1.43	30.4	1.46	31
20R-5, 36–41	4	170.50	3.60	51.3	–46.8	7.73E–03	10.86	2.23	33.6	1.62	32B
21R-3, 138–142	5	177.87	1.89	26.5	–21.7	3.34E–02	1.32	4.71	17.4	0.40	33
23R-1, 68–73	9	192.58	2.56	10.2	ND	5.40E–02	1.10	15.48	9.3	0.17	34B
25R-1, 82–86	9A	207.12	1.17	35.5	–65.0	2.69E–02	1.01	6.55	19.5	0.18	36
26R-2, 5–11	1	212.32	2.69	25.8	–65.9	1.70E–02	3.68	4.79	21.6	0.56	38
27R-1, 70–75	5B	216.00	4.38	26.9	–62.3	1.84E–02	5.53	4.47	28.8	0.98	40
30R-1, 110–115	15	231.00	1.49	22.0	–62.1	1.77E–02	1.95	5.35	13.2	0.28	43
30R-3, 37–41	6	233.02	4.65	55.7	–63.1	2.37E–02	4.57	6.52	31.1	0.71	44
31R-3, 106–110	11A	238.66	3.26	27.1	–60.8	9.18E–03	8.26	3.21	15.5	1.01	46
32R-3, 134–137	13	243.90	5.36	60.8	–55.3	1.92E–02	6.50	7.12	23.9	0.75	47
34R-1, 19–21	4	259.09	2.29	25.1	–61.9	2.45E–02	2.17	ND	ND	ND	49
34R-2, 41–46	4A	260.75	3.09	16.0	–54.3	5.44E–02	1.32	6.37	13.2	0.48	49
35R-2, 26–31	1B	265.06	2.55	15.5	–75.5	1.40E–02	4.25	5.55	9.0	0.46	50
36R-6, 34–40	1B	275.56	13.39	31.6	–69.1	2.72E–02	11.44	7.67	26.7	1.75	52
39R-3, 95–100	6C	296.14	3.22	34.8	–76.8	1.83E–02	4.10	2.17	26.2	1.49	52
47R-3, 80–82	5D	349.43	10.46	38.5	–78.9	1.37E–02	17.79	11.78	32.7	0.89	54
54R-5, 16–18	1A	389.84	0.32*	29.9*	–74.8	1.12E–02	0.66*	1.57	8.6	0.20*	58
55R-4, 11–14	1B	398.05	5.98*	5.3*	ND	5.27E–02	2.64*	7.76	6.7	0.77*	60
57R-3, 81–83	1	416.30	0.13	>70.0*	ND	2.45E–03	1.21	0.35	26.7	0.37	61B
57R-6, 89–91	2C	420.70	0.99	43.2*	ND	1.33E–02	1.72	3.54	28.3	0.28	62
57R-7, 20–22	1A	421.49	1.05*	6.3*	ND	4.89E–03	4.99*	0.88	27.6	1.19*	62
58R-2, 33–37	1B	423.89	0.36	31.3*	ND	1.17E–02	0.71	ND	ND	ND	63
59R-1, 102–109	2F	433.12	0.43	36.6*	–70.6	6.36E–03	1.57	2.00	21.3	0.22	64
60R-1, 75–77	2F	437.45	3.49	28.5*	–29.2	2.53E–02	3.20	6.92	26.7	0.50	65
61R-2, 54–56	1	443.16	0.03*	>90.0*	ND	3.70E–03	0.16*	0.84	18.1	0.03*	66
64R-1, 125–127	5	471.95	4.04*	3.5*	ND	1.70E–02	5.54*	3.63	5.1	1.11*	68
67R-4, 106–110	5A	504.99	2.53	42.2*	–79.5	1.61E–02	3.66	3.03	19.7	0.83	70
69R-2, 90–94	3D	521.20	5.90	34.6*	–70.1	1.19E–02	11.53	3.04	26.7	1.94	71
71R-4, 32–34	3	542.12	2.94	39.2*	–64.8	1.07E–02	6.39	2.62	29.9	1.12	72
72R-1, 100–102	3E	548.30	2.04	51.5*	–66.5	1.11E–02	4.27	3.37	36.2	0.61	73A
73R-2, 42–44	1D	558.83	7.68	23.7	–78.2	7.42E–02	2.41	12.77	21.3	0.60	74A
78R-2, 136–137	4B	597.99	0.93	34.6	–68.5	3.65E–03	5.96	6.35	26.2	0.15	76
79R-2, 91–95	1E	607.35	1.24*	39.2*	–62.3	1.11E–02	2.60*	3.41	8.8	0.36*	78
79R-5, 90–92	1E	611.37	0.17	>99.0	ND	1.40E–02	0.28	35.68	8.4	0.01	79
80R-4, 102–106	1D	619.91	1.97	26.5	–58.7	7.46E–03	6.13	1.35	18.1	1.46	79
81R-3, 97–99	1D	628.25	0.31	42.7	–68.1	2.41E–03	2.99	0.31	30.2	1.00	80
82R-2, 109–111	1C	636.66	0.91	34.6	–70.8	5.84E–03	3.63	0.88	26.0	1.04	82
83R-2, 129–131	1D	646.59	0.95*	3.5*	–65.7	8.24E–03	2.67*	1.14	8.1	0.83*	82
84R-2, 95–97	3D	655.95	2.40	28.3*	–66.3	1.83E–02	3.05	2.94	17.6	0.82	83
86R-3, 66–70	1D	675.99	0.86	41.3*	–70.6	4.96E–03	4.03	0.73	23.9	1.18	84
87R-2, 31–33	1A	683.59	5.98	47.6	–73.4	1.32E–02	10.58	4.44	33.6	1.35	84
89R-2, 6–8	1B	702.35	0.43*	57.1*	–73.6	6.43E–03	1.57*	0.93	21.6	0.46*	84
90R-1, 41–45	2A	710.51	1.22	47.3*	–80.1	3.01E–03	9.43	1.09	35.5	1.12	85
90R-5, 52–56	1B	715.60	1.12	45.7*	–77.2	5.44E–03	4.81	1.04	33.9	1.08	86
92R-4, 5–10	1	727.44	0.78	35.5	–55.7	7.00E–03	2.60	1.11	25.1	0.70	87
94R-4, 8–10	1A	744.11	0.98	34.1	–49.6	8.78E–03	2.60	1.21	21.3	0.81	87
95R-2, 61–63	1D	751.91	0.89	43.6	ND	6.56E–03	3.17	0.95	24.8	0.94	87
96R-1, 123–125	10A	760.63	0.84	29.0*	–77.0	1.22E–02	1.60	2.02	18.3	0.41	88
97R-2, 42–44	1B	770.67	9.38*	16.7*	ND	5.70E–03	38.31*	1.15	26.0	8.16*	89
99R-2, 78–80	1F	790.55	3.26	23.2	–78.3	1.47E–02	5.15	28.91	19.5	0.11	90
100R-1,104–108	1F	799.04	1.02	12.3	–73.9	1.31E–02	1.82	2.18	7.2	0.47	91
101R-4, 81–85	5	812.24	3.02	25.1	–78.1	1.83E–02	3.83	4.59	22.5	0.66	92

Note: NRM = natural remanent magnetization; MDF-NRM = median destructive field of the NRM; St. inc. = stable inclination; Suscept. = bulk volume susceptibility; Q ratio = Koenigsberger ratio; ARM = anhysteretic remanent magnetization; MDF-NRM = median destructive field of the ARM; Unit = identified petrological unit ("Igneous Petrology" section, this chapter); ND = not determined; * values tentative = samples have a significant secondary magnetization.

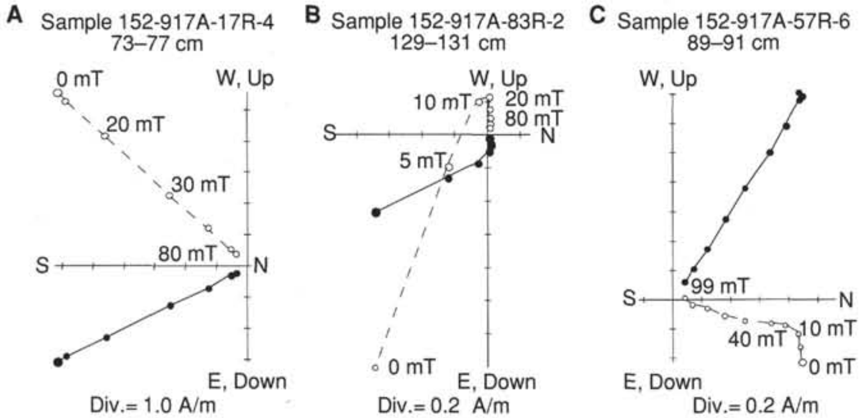

Figure 6. Examples of response to AF demagnetization of lava specimens from Hole 917A. In the Zjiderveld (1967) diagrams, solid symbols = points on the horizontal projection plane and open symbols = points on the vertical plane. Demagnetization step values are shown adjacent to the vector plotted or the vertical plane. **A.** A single component reverse polarity sample from the upper part of the volcanic pile of Hole 917A. **B.** A sample from the lower part of the volcanic sequence in Hole 917A. The sample carries a two component remanence. Demagnetization reveals the reverse high-coercivity (primary) magnetization at 20 mT. **C.** A sample representative of igneous Units 61B to 63. Note the shallow positive inclination of the high-coercivity component.

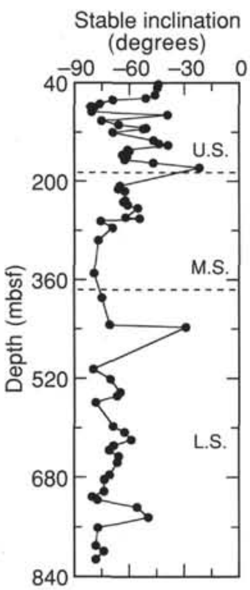

Figure 7. Stable magnetic inclination plotted vs. depth in Hole 917A. The stratigraphy of the lava succession is shown also (see "Igneous Petrology" section, this chapter). U.S.= Upper Series; M.S.= Middle Series; L.S.= Lower Series.

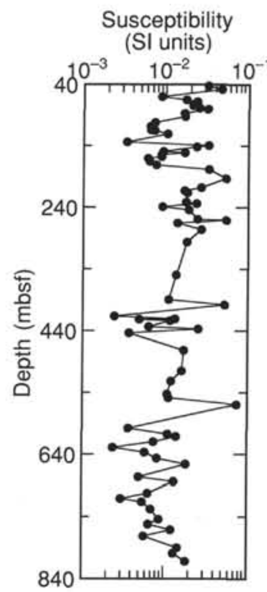

Figure 8. Bulk magnetic susceptibility plotted vs. depth in Hole 917A.

The anhysteretic remanent magnetization (ARM) of the lava samples also was measured. Specimens were subjected to a direct magnetic field of 0.1 mT with an AF field peak of 90 mT. ARM and NRM intensities are similar (Table 6): the mean NRM/ARM ratio is 0.96. ARM and initial NRM intensities are positively correlated despite wide fluctuations in both parameters (Fig. 10). The median destructive field of the ARM (mean value = 21.9 mT) is consistently lower than that of the NRM (mean value = 31.5 mT), however, both are positively correlated. No obvious downhole trends are identified (Fig. 11).

Presently, data from the measurement of a number of magnetic parameters for lava samples from Hole 917A do not permit any fine-scale variations with depth (time) to be identified. Complementary shore-based experiments will be necessary to investigate whether such variations exist and how they relate to the petrology and evolution of the lavas in Hole 917A.

SEDIMENTATION RATES

No meaningful age-vs.-depth diagram can be constructed for Site 917 sediments because of the lack of age information. The identification of a middle Eocene nannofossil assemblage in Core 152-917A-4R, however, facilitates correlations of sediment sequences at different sites, based on seismic-profile data. Detailed studies of the latter data might permit the construction of a useful age-vs.-depth diagram for this site.

IGNEOUS PETROLOGY

Lithological Units

Volcanic rocks were cored from the top of the lava pile at 41.9 mbsf down to its base at 820.7 mbsf, and 55.7% of the 778.8-m sequence was recovered. The rocks are predominantly basaltic, but range in composition from picrite to acid welded tuff. They were divided into 92 volcanic units (Table 7), including one inclined intrusive sheet, on the basis of examination of hand specimens. Flow tops were preserved in 78 units, but had to be inferred in the others. Thus, at least 91 flows are represented in the sequence. The units were classified into nine lithological types primarily on the basis of examination of hand specimens.

The term "picrite" is used here to denote a rock-type conspicuously rich in olivine phenocrysts (≥15% by volume visible in hand specimen, although a larger proportion often is reported in thin section). The term is used in a descriptive sense only and carries no implication of an

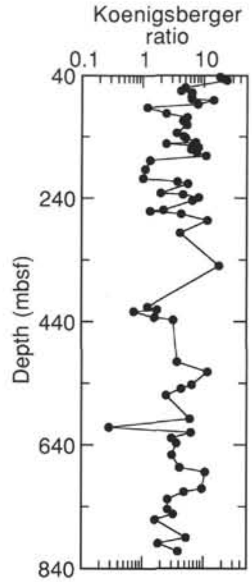

Figure 9. Koenigsberger ratio (Q ratio; see text) plotted vs. depth in Hole 917A.

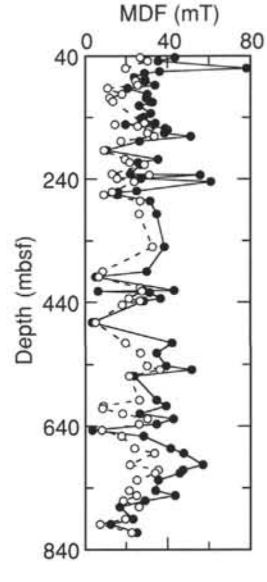

Figure 11. Comparison between median destructive fields (MDF) of NRM and ARM intensities plotted vs. depth in Hole 917A (respectively, NRM and ARM with solid and open symbols).

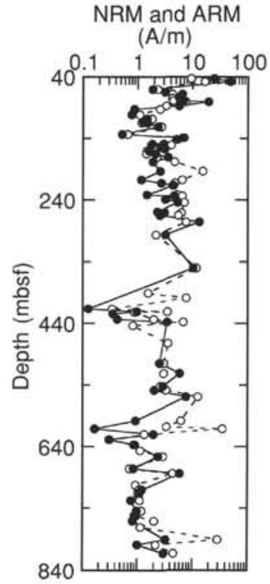

Figure 10. Comparison between natural and anhysteretic remanent magnetizations plotted vs. depth in Hole 917A (respectively, NRM and ARM with solid and open symbols).

unusually MgO-rich parental liquid. Accumulation of olivine phenocrysts must have occurred in all picrite units. Olivine-phyric basalt is less olivine-rich than picrite, but has not necessarily crystallized from a less-magnesian liquid. Typically, it contains <1% to 15% olivine phenocrysts visible in hand specimen. Aphyric olivine basalt is by far the most common rock type encountered at Site 917 (39 flow units) and is defined by the presence of olivine visible in hand specimen. Groundmass olivine is easily recognized on account of its alteration to red iddingsite or green clay minerals. Some aphyric olivine basalts are very olivine-rich and clearly represent highly magnesian liquids.

Olivine-plagioclase-phyric basalts are often difficult to recognize because the plagioclase phenocrysts tend to be small and tabular and grade in size down to that of groundmass plagioclase. Only rocks with plagioclase phenocrysts readily visible in hand specimen are included in this category. The total phenocryst content typically varies from 1% to 10% by volume but estimates based on hand-specimen examination are invariably lower than those based on thin sections. Sparse, but large, euhedral phenocrysts of black augite were seen in three basalt units (Units 60, 70, and 72) accompanied, in each case, by olivine and plagioclase phenocrysts. Basalt with conspicuous phenocrysts of plagioclase, but without visible olivine phenocrysts, is rare. Sparsely porphyritic basalt with occasional tabular plagioclase phenocrysts, slightly larger than the groundmass plagioclase, is more common.

Aphyric lavas without obvious olivine tend to be pale-colored and clearly are more evolved than aphyric olivine basalt. These are frequently flow-banded. The term "basalt" was applied to such rocks when describing cores, although many are too evolved for this term to be applied strictly.

Three dacite flow units (Units 54, 55, and 57) were identified on the basis of their texture and phenocryst assemblage. They are aphanitic with a spherulitic texture in places and contain small phenocrysts of feldspar and pyroxene. Pyroclastic units include welded and non-welded tuffs.

Stratigraphic Units

A stratigraphic log of the distribution of rock types within the volcanic sequence is shown in Figure 12, and the depths to the upper and lower boundaries of each unit are presented in Table 7. It is apparent from the log that unit thicknesses vary from less than 1 m to more than 50 m. This variation is real and reflects original variation in flow thickness. The flow units in the upper part of the sequence tend to be thin (generally <10 m), whereas thicker flows (>20 m) are found in the lower part. This variation is shown in Figure 13. Thin flows are present throughout the sequence but with the exception of a single huge flow (Unit 52) at 272 mbsf, the upper envelope of the flow-size distribution increases smoothly downward through the succession.

The distribution of rock types also varies through the lava pile. The volcanic succession can be divided into three clearly defined stratigraphic series: an upper picrite and olivine basalt series, a middle evolved series, and a lower basaltic series. Here, we refer to these as the Upper, Middle, and Lower Series, respectively (Table 8). A 67-cm sandstone horizon at 183.4 mbsf (Unit 34A) marks the base of the Upper Series and separates strikingly olivine-rich flows above from virtually olivine-free flows below. The flows beneath the sediment

Table 7. Location of tops and bases of igneous units in Hole 917A.

Unit	Top of core (Hole 917A) (cm)	Base of core (Hole 917A) (cm)
Upper Series		
1	6R-1, 28	7R-1, 52
2	7R-1, 52	7R-2, 44
3	7R-2, 44	7R-2, 55
4	8R-1, 0	8R-1, 55
5	8R-1, 55	8R-1, 106
6	8R-1, 106	8R-4, 68
7	8R-4, 68	9R-1, 85
8	9R-1, 85	9R-4, 145
9	9R-4, 145	10R-3, 120
10	10R-3, 120	10R-4, 85
11	10R-4, 85	10R-6, 49
12	10R-6, 49	11R-2, 15
13	11R-2, 15	11R-5, 16
14	11R-5, 16	12R-1, 148
15	12R-2, 0	12R-3, 35
16	12R-3, 35	13R-2, 123
17	13R-2, 123	13R-6, 27
18	13R-6, 27	14R-4, 122
19	14R-4, 122	15R-2, 150
20	16R-1, 0	16R-1, 32
21	16R-1, 32	16R-6, 29
22	16R-6, 29	16R-6, 90
23	16R-6, 90	17R-3, 80
24	17R-3, 80	18R-1, 8
25	18R-1, 8	18R-4, 25
26	18R-4, 25	18R-5, 19
27	18R-5, 19	18R-7, 60
28	18R-7, 35	19R-1, 45
29	19R-1, 45	19R-1, 128
30	19R-1, 128	19R-2, 60
31A	19R-2, 60	19R-5, 80
31B	20R-1, 0	20R-1, 90
32A	20R-1, 90	20R-1, 130
32B	20R-1, 130	21R-3, 70
33	21R-3, 70	22R-1, 61
Middle Series		
34A	22R-1, 61	22R-1, 130
34B	22R-1, 130	23R-2, 122
35A	23R-2, 122	23R-2, 138
35B	23R-3, 0	23R-3, 41
35C	23R-3, 41	23R-3, 45
35D	24R-1, 0	24R-1, 10
35E	24R-1, 10	24R-1, 110
36	24R-1, 110	25R-2, 20
37	25R-2, 20	25R-3, 62
38	25R-3, 62	26R-2, 60
39	26R-2, 60	27R-1, 5
40	27R-1, 5	27R-1, 131
41	27R-1, 131	27R-3, 99
42	27R-3, 99	29R-1, 145
43	29R-1, 145	30R-2, 62
44	30R-2, 20	31R-1, 20
45	31R-1, 20	31R-2, 68
46	31R-2, 68	32R-2, 74
47	32R-2, 74	32R-4, 115
48	32R-4, 115	33R-2, 85
49	34R-1, 0	34R-2, 69
50	35R-1, 0	36R-1, 13
51	36R-1, 13	36R-3, 25
52	36R-3, 25	45R-1, 12
53	45R-1, 12	46R-2, 15
54	47R-1, 0	48R-1, 8
55	48R-1, 8	52R-1, 63
56	53R-1, 0	53R-1, 115
57	53R-1, 115	53R-2, 138
Lower Series		
58	53R-2, 138	54R-6, 76
59	54R-6, 76	54R-7, 15
60	54R-7, 15	56R-3, 14
61A	56R-3, 14	56R-3, 30
61B	56R-3, 30	57R-3, 125
62	57R-3, 125	57R-7, 135
63	58R-1, 0	58R-3, 140
64	58R-4, 0	59R-2, 37
65	59R-2, 37	60R-1, 101
66	60R-1, 101	62R-2, 112
67A	62R-2, 112	62R-2, 120
67B	62R-2, 120	63R-1, 9
68	63R-1, 9	64R-3, 132
69	64R-3, 132	65R-4, 118
70	65R-4, 118	68R-1, 22
71	68R-1, 22	71R-1, 44
72	71R-1, 44	71R-4, 112
73A	72R-1, 0	72R-4, 90
73B	72R-4, 90	72R-6, 56
74A	73R-1, 0	74R-5, 56
74B	75R-1, 0	75R-1, 42
74C	75R-1, 42	75R-2, 63
75A	75R-2, 63	77R-1, 10
75B	77R-1, 10	77R-3, 27
75C	77R-3, 27	77R-3, 100
76	77R-3, 100	78R-6, 110
77	78R-6, 110	77R-7, 116
78	77R-7, 116	79R-3, 65
79	79R-3, 65	81R-1, 9
80	81R-1, 9	81R-3, 112
81A	81R-3, 112	81R-3, 150
81B	81R-4, 0	82R-1, 5
82	82R-1, 5	83R-5, 20
83	83R-5, 20	85R-2, 75
84	85R-2, 75	89R-7, 65
85	89R-7, 65	90R-2, 29
86	90R-2, 29	90R-6, 130
87	91R-1, 0	95R-3, 54
88	96R-1, 0	97R-1, 11
89	97R-1, 11	97R-4, 72
90	98R-1, 0	99R-5, 21
91	99R-5, 21	100R-4, 37
92	101R-1, 0	102R-3, 78

Table 8. Summary of the three stratigraphic series within the volcanic succession at Site 917.

Series	Depth (mbsf)	Series thickness (m)	Number of units	Mean unit thickness (m)	Rock types (number of units in parenthesis)
Upper	41.9–183.4	141.5	34	4.2	Aphyric olivine basalt (19), olivine-phyric basalt (10), picrite (5).
Middle	184.1–376.7	193.4	23	8.1	Aphyric basalt (12), plagioclase-phyric basalt (6), dacite (3), tuff (2).
Lower	376.7–820.7	444.0	35	12.7	Aphyric olivine basalt (16), olivine-plagioclase-phyric basalt (8), olivine-plagioclase-pyroxene-phyric basalt (4), olivine-phyric basalt (3), aphyric basalt (2), picrite (2).

horizon comprise more evolved types that persist downsection until, beneath the dacite flows and welded tuff at the base of the Middle Series (Units 54 to 57), the rocks become more basic again. Olivine-rich basalt dominates the Lower Series. The natural division into three series is clearly shown in the variation of Ni concentration with depth for a representative suite of volcanic rocks analyzed by shipboard XRF (Fig. 14). The low Ni contents of the olivine-poor Middle Series lavas contrast strikingly with the higher Ni contents of the lavas of the Upper and Lower Series. This division into three series is also is apparent in the MST natural gamma signal of the core (Fig. 15), and the base of the Middle Series is readily identifiable in the downhole gamma-ray log (Fig. 16).

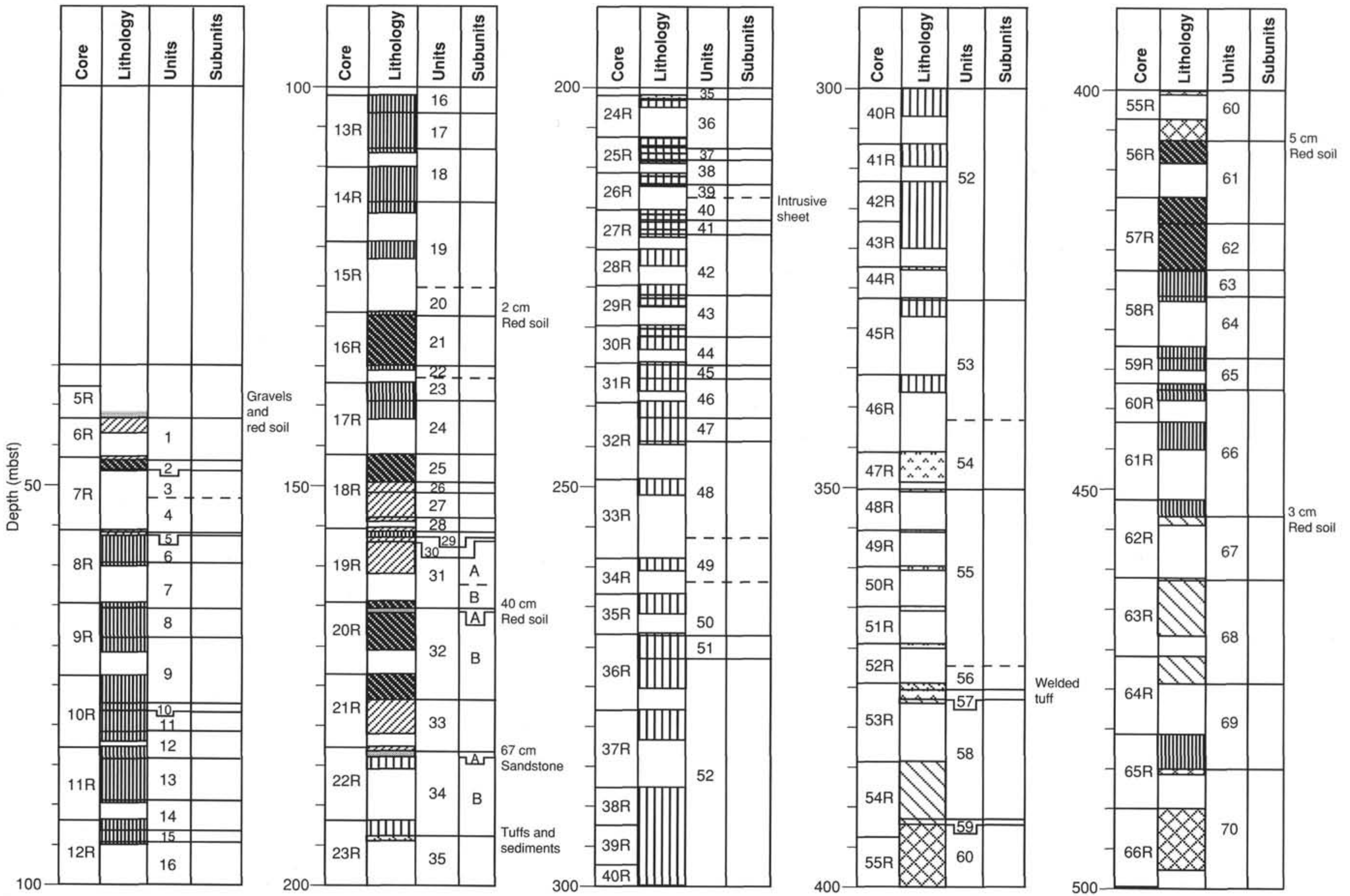

Figure 12. Stratigraphic log showing the volcanic succession cored at Site 917.

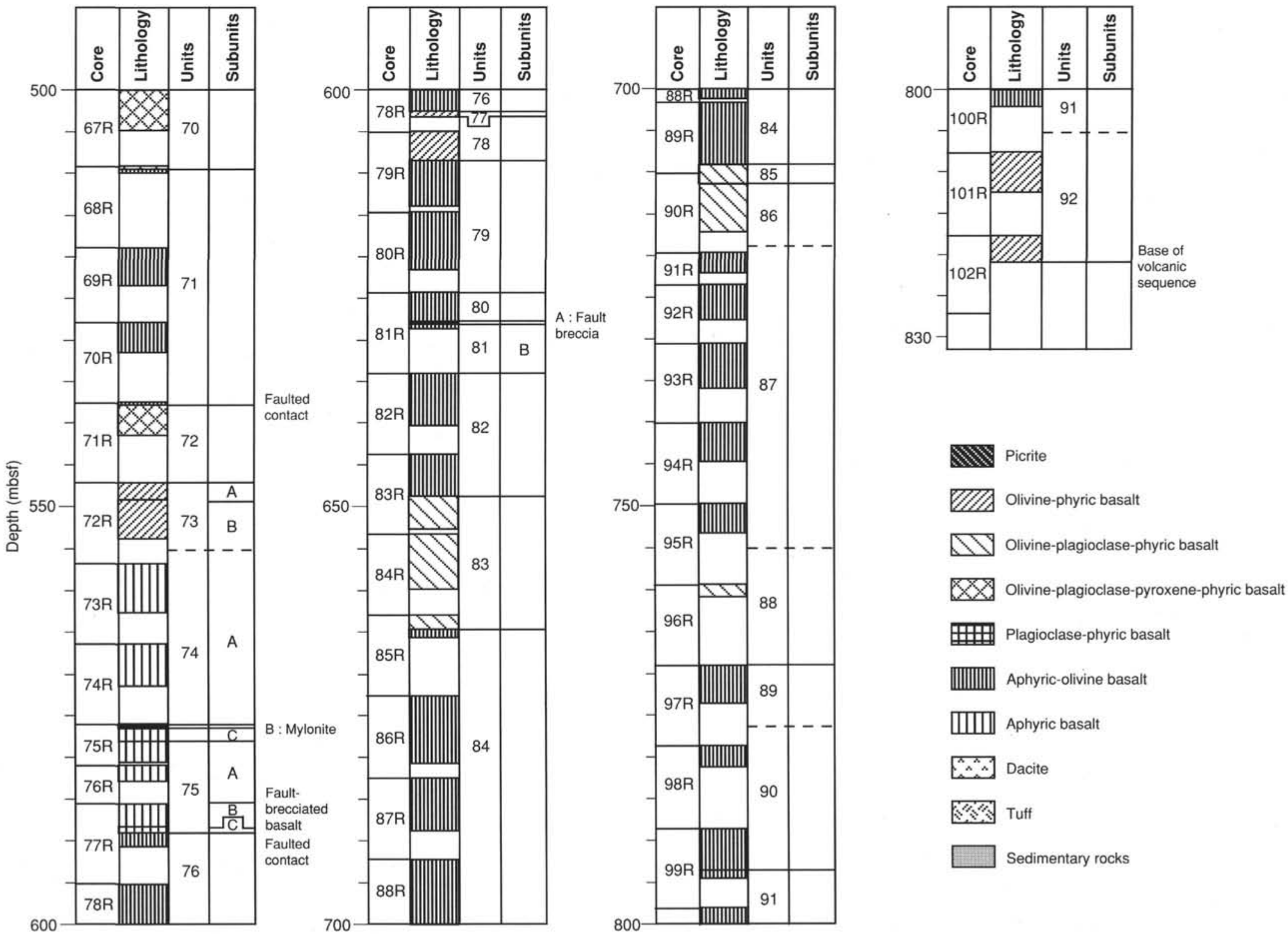

Figure 12 (continued).

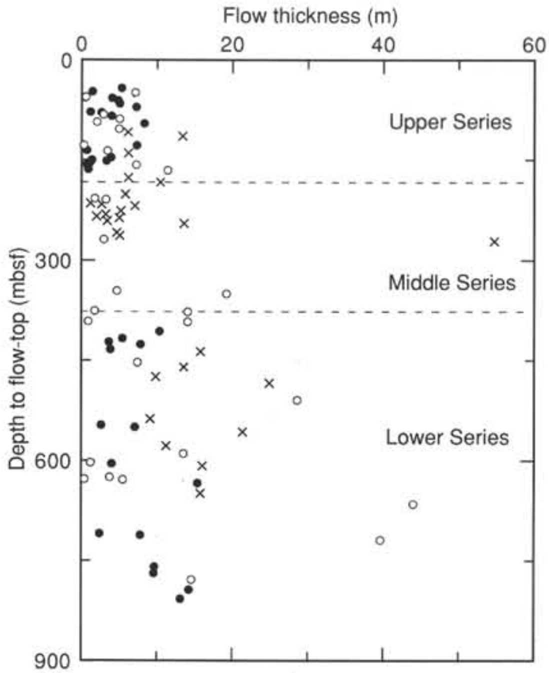

Figure 13. Flow thickness and flow morphology vs. estimated depth to flow top at Site 917. Some flows could not be classified as either pahoehoe or aa lavas. A closed circle indicates pahoehoe, x indicates aa, and an open circle indicates unknown. Estimates of depth and thickness are based on recovered core and are subject to some uncertainty (see Fig. 12).

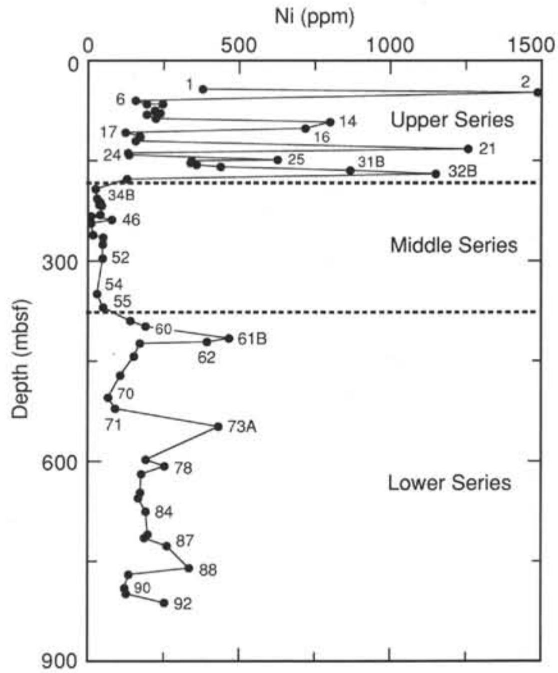

Figure 14. Diagram of Ni vs. depth. Ni content is a good indicator of the degree of differentiation of a lava unit. Lines are drawn between successive analyzed units, although not all units have been analyzed. The Lower Series is interrupted by several faults with unknown offset (between Units 71 and 72, within Units 74 and 75, and between Units 80 and 81). Selected units are numbered.

Flow Morphology and Lithology

Many of the lavas drilled in Hole 917A are recognizable as pahoehoe or aa lavas. Pahoehoe lavas typically form thin flows with chilled, finely vesicular tops and bases. They have zones near the tops and bases with concentrations of larger, often spherical to irregular or pipe-shaped vesicles, while the central parts may be massive, much less vesicular, and not particularly fine-grained. Aa lavas typically form relatively thick flows with flow-brecciated, often scoriaceous tops and sometimes also flow-brecciated bases. Many aa lavas exhibit flow-banding defined by flattened vesicles or by alternating darker and lighter bands in the fine-grained groundmass. In some cases, however, a flow may exhibit mixed features. Good examples of pahoehoe lavas are those of Unit 13 (Core 152-917A-11R) and Units 25 through 31 (Cores 152-917A-18R and -19R); examples of aa lavas are those of Unit 18 (Cores 152-917A-13R and -14R) and Unit 70 (Cores 152-917A-66R and -67R) (see the photographs in the "Cores" section of the volume).

The entire volcanic succession appears to have erupted under subaerial conditions. Reddened, oxidized flow tops occur throughout the sequence, and a few horizons of red soil have developed on flow tops. A welded ash-flow tuff is also clearly subaerial. Furthermore, the absence of pillow lavas and large hyaloclastite units indicates that deep water was not present. Two units (Units 52/53 and 92) have brecciated, glassy basal parts, which suggests that shallow water was present intermittently.

The Upper, Middle, and Lower Series show significant differences in the dominant flow morphologies, as illustrated in Figure 13 and described below.

Upper Series

The 34 lava units of the Upper Series (Units 1 through 33, with Units 31A and 31B counting as two separate units), from 41.9 to 183.4 mbsf, have thicknesses that range from 0.5 m (Unit 5) to 11.4 m (Unit 32), with an average thickness of 4.2 m (Table 8). Of these, 20 flows are clearly pahoehoe lavas, four show typical aa features, three show mixed features, and six cannot be classified, mostly because of poor recovery (Fig. 12).

The lavas of the Upper Series are subaerial, with reddened, oxidized flow tops. However, a sequence of six thin pahoehoe flows at 146 to 157 mbsf (Units 25–30) show no reddening of the tops. Nor do they show signs of the presence of water and most probably were emplaced in rapid succession, perhaps during the same eruption.

Weathering features in the form of strong reddening, obliteration of igneous structures, and gradual transformation into red soil are seen in the tops of Units 1, 21, and 32B (Fig. 17). Thus, at least two periods of quiescence occurred during the formation of the Upper Series. Significantly, both Units 21 and 32B are picrites, whereas Unit 1 is olivine-phyric, but overlies a picrite (Fig. 14). The eruption of two of the three most Ni-rich lavas in the Upper Series was thus followed by a period of quiescence or a shift in the position of the center of volcanic activity. A similar situation may perhaps be envisaged for the third Ni-rich lava (Unit 2), but the amount of volcanic rock removed from the top of the pile by erosion is not known.

Middle Series

The 23 volcanic units of the Middle Series (Units 34–57, excluding the dike Unit 39), 184.1 to 376.7 mbsf, have thicknesses ranging from 2.0 m (Unit 45) to 54.8 m (Unit 52); the average thickness is 8.1 m (including Unit 52) or 6.3 m (excluding Unit 52). These lavas are almost exclusively typical aa flows, with thick, highly brecciated, scoriaceous tops. Several also have brecciated bases, and a few are flow-brecciated throughout. Flow-banding is common in the central parts of flows, and this feature is especially well-developed in the very thick lava Unit 52 (see the photographs of Cores 152-917R-36R to -43R in "Cores" Section, this volume).

Unit 35 is a complex sedimentary-volcanic horizon having five subunits. Its total thickness is 6.5 m, but recovery was poor, and no

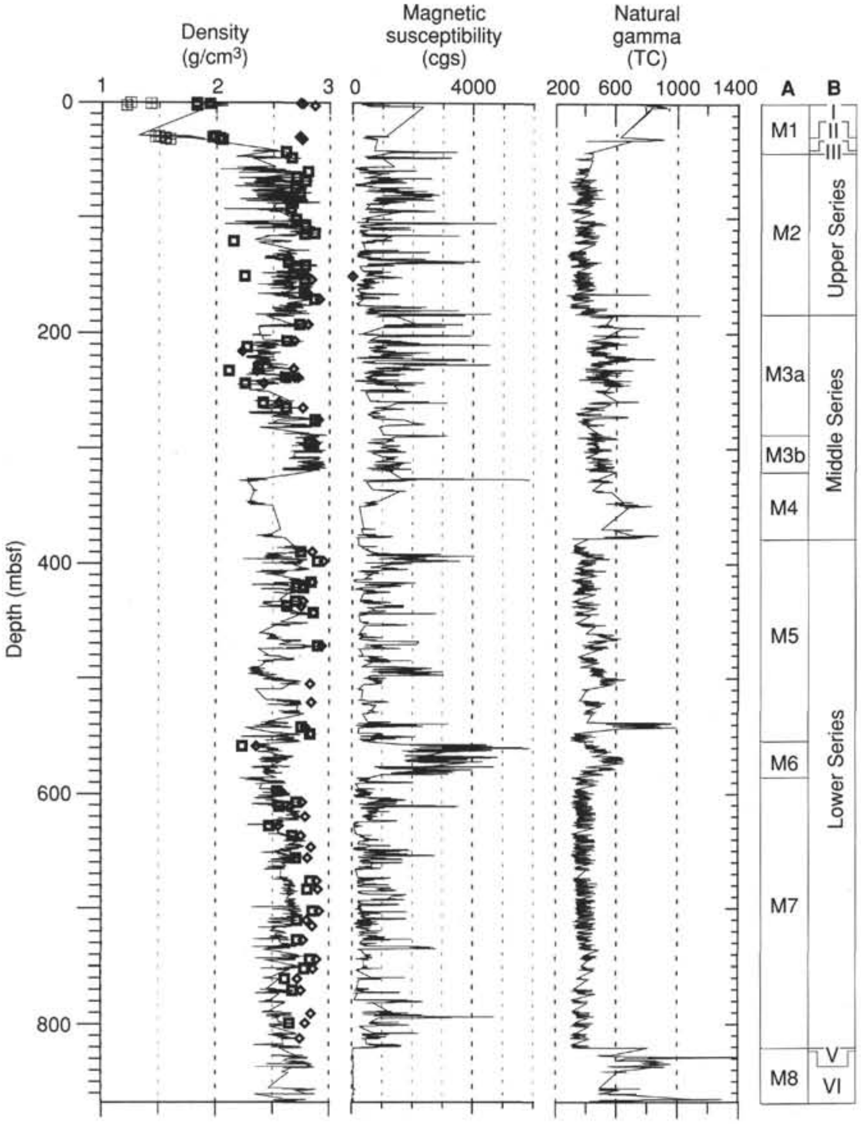

Figure 15. Composite plot of MST and discrete index-property data for sediments, volcanic rocks, and metasediments recovered at Site 917. MST data comprise GRAPE wet bulk density (empirically corrected for reduced diameter as a result of RCB-coring; see "Physical Properties" section, "Explanatory Notes" chapter, this volume) magnetic susceptibility, and natural gamma. Discrete measurements include wet bulk density (open squares), grain density (open diamonds), dry density (hachured squares), water content (open circles), and porosity (filled squares). Column A denotes mechanical units as defined in the text. Column B denotes lithologic/petrologic unit/series, as defined in the "Lithostratigraphy" and "Igneous Petrology" sections (this chapter).

boundaries between the subunits were preserved. From the bottom upward, the recovered rocks are (1) 1 m of oxidized basaltic breccia/conglomerate that grades into the underlying flow top, but also contains rounded, transported clasts and probably represents somewhat reworked flow-top rubble; (2) 10 cm of crystal tuff with close-lying 1- to 3-mm feldspar crystals in a vitric, banded tuff matrix (Fig. 18); (3) 5 cm of red soil; (4) 40 cm of hyaloclastite tuff/breccia, with phenocrysts of feldspar and pyroxene; and (5) 10 cm of dark reddish-brown sediment with fragments of feldspar and pyroxene and a single 1-cm fragment of pink rhyolitic(?) rock. The record may be interpreted as a few individual bursts of explosive magmatic activity, separated by periods of quiescence, of which three are recorded in the core. The two soil horizons, however, might also represent lahar deposits related to the eruptive activity. No sediment horizons, other than those in Unit 35, were observed in the Middle Series.

Units 54 through 57 at the base of the Middle Series are dacitic. Their total thickness is 35 m, but recovery was poor, and no boundaries between the units were preserved. Unit 54 is a strongly vesicular lava having very flattened vesicles and 3- to 5-mm-diameter devitrification spherules in hydrated glass (Figs. 19 and 20). Unit 55 is massive and densely spherulitic. Both these units are mixed rocks. Unit 54 contains 10% lithic clasts 0.5 to 5 cm across that range from highly lobate with crenulated margins to subangular (Figs. 19 and 20). They consist of olivine-plagioclase-pyroxene-phyric basalt and gabbro. Unit 55 contains similar clasts, but much fewer, which suggests that Units 54 and 55 may have been produced during successive stages of the same eruption. Unit 56 is a brick-red welded ash-flow tuff (Fig. 21), and Unit 57 is a massive dacite lava. No xenoliths were observed in these two units, and they may perhaps also have been produced during one eruption.

The lavas and tuffs of the Middle Series are subaerial, with reddened, oxidized tops on most of the flows. Units 46 through 49 show no reddening of the flow tops and may have been extruded in rapid succession. Unit 53 is a water-lain hyaloclastite deposit that has been interpreted as a basal facies of the very thick lava Unit 52. It immediately overlies the dacitic units, and it is conceivable that thick, dacitic eruption products from a nearby central volcano gave rise to local topographic variations and formation of lakes.

Unit 39 has been interpreted as an inclined dike because of its generally homogeneous character and the presence of a glassy, chilled margin along its upper contact. The lower contact was not recovered. In the FMS log, this unit can be seen to dip more steeply than the lava flows (see "Downhole Measurements" section, this chapter).

Lower Series

The 35 lava units of the Lower Series (Units 58–92), 376.7 to 820.7 mbsf, have thicknesses that range from 0.9m (Unit 59) to 44 m

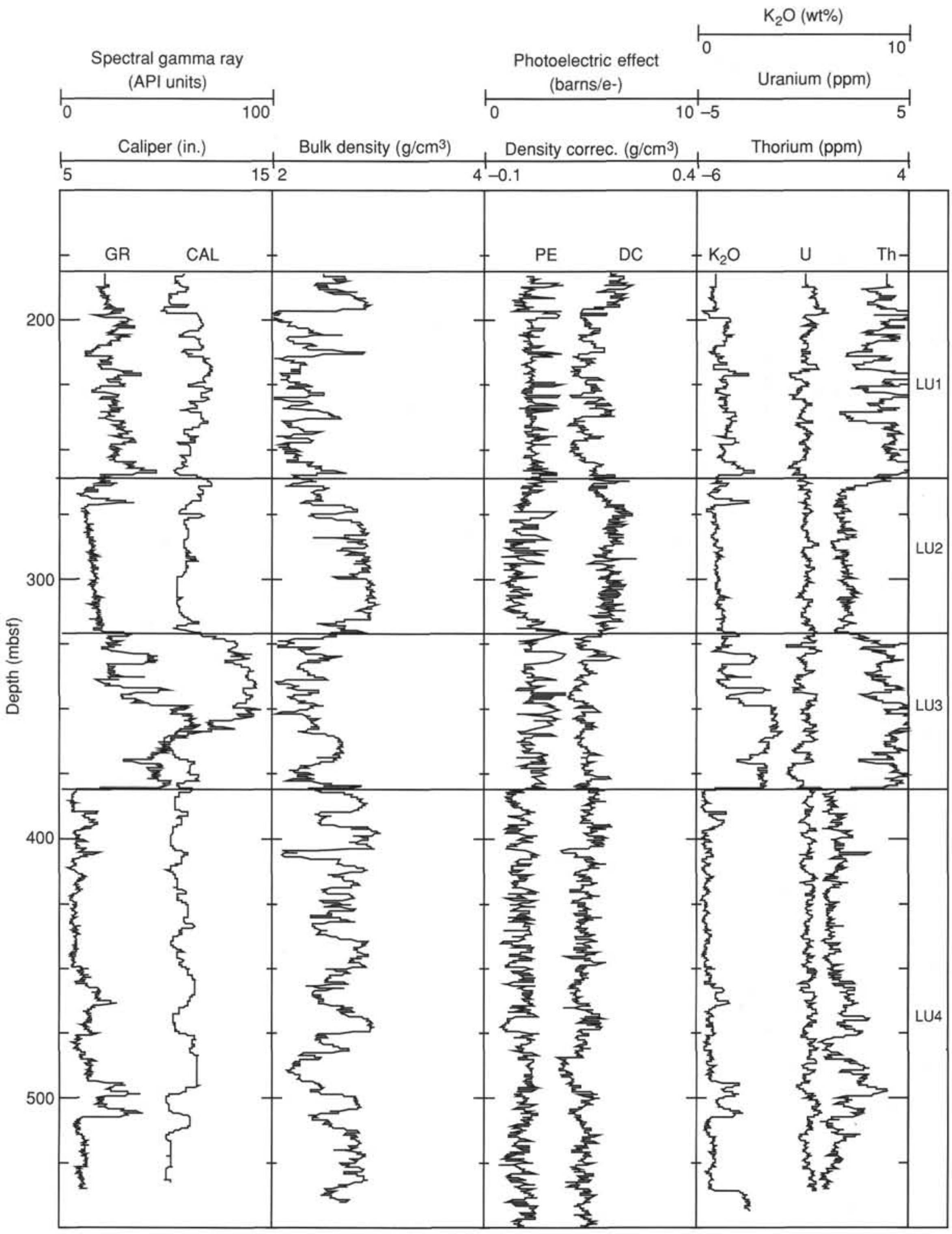

Figure 16. Summary log from NGT (gamma-ray) and HLDT (density) tools.

(Unit 84); the average thickness is 12.7 m (Table 8). The Lower Series consists of alternating sequences of thin pahoehoe and thicker aa lavas; 15 lavas are of pahoehoe type and nine are of aa type (Fig. 13). Several flows, such as the two thick Units 84 and 87, show mixed or nondiagnostic features. These two flows have flow-brecciated tops, typical of aa lavas, and massive, relatively coarse-grained central parts, as found in pahoehoe lavas. The two units have a well-developed ophitic texture and also have abundant rounded segregation patches up to 3 cm in diameter (Fig. 22).

The lavas of the Lower Series were subaerially erupted and most have reddened flow tops. However, a number of the lowest flows do not have red top zones, although the tops may be flow-brecciated (Units 84, 87–89, and 92). This may indicate rapid eruption or perhaps the presence of water. The basal Unit 92 exhibits intense primary

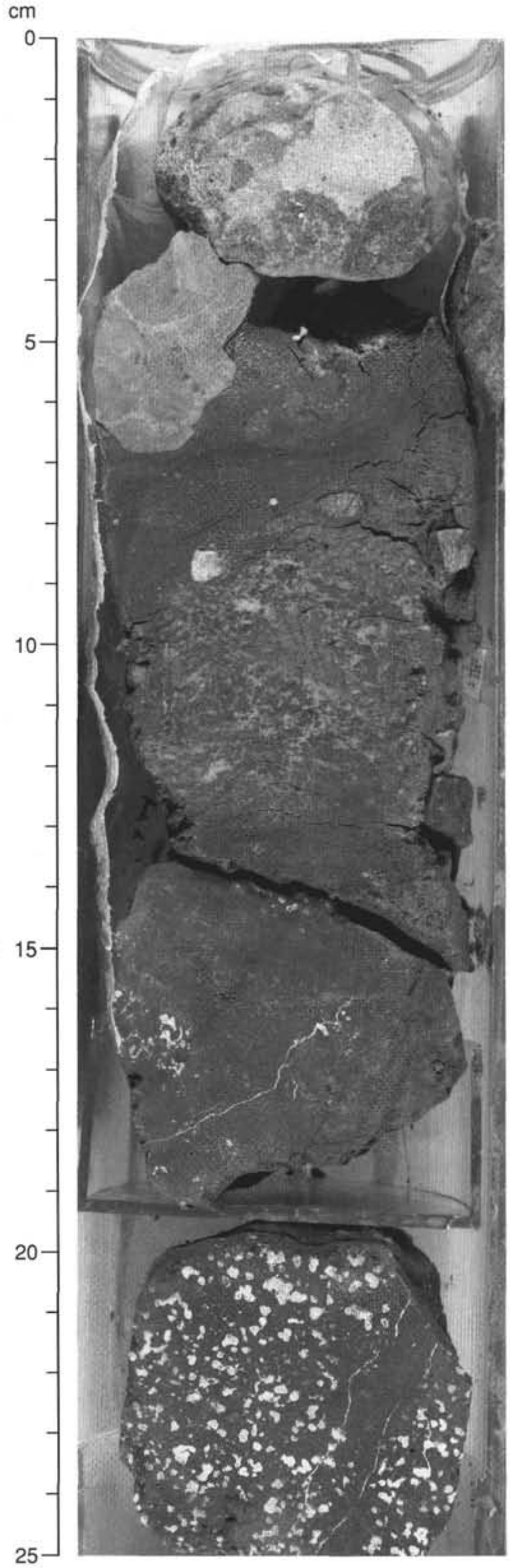

Figure 17. The top of the volcanic succession at Site 917 (Interval 152-917A-6R-1, 0–25 cm). Unit 1 starts at 20 cm, which is probably near the original flow top, although the chilled crust is missing. Above 20 cm, a dark reddish-brown soil horizon can be seen, and above 6 cm, two rounded pebbles are in contact with the soil.

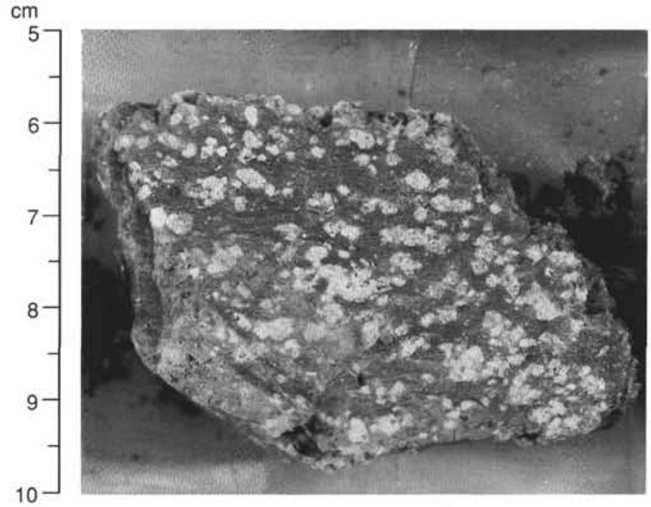

Figure 18. Crystal tuff, Unit 35D, with 1- to 3-mm feldspar crystals in a finely banded, vitric tuff matrix (Interval 152-917A-24R-1, 5–10 cm).

brecciation in the lowest 3.5 m of the flow, probably because it flowed into shallow water. Two thin horizons with weathering and formation of red soil layers occur toward the top of the Lower Series, above Units 61B (Fig. 23) and 67B.

Structure

Tilting

Post-depositional tilting of the lava succession may be deduced from the dips of structures, such as sedimentary bedding and lava flow boundaries, vesicular zones, flow-banding, and flattened vesicles. These structures may not necessarily have been horizontal originally and should thus be used with caution. However, if several of these structures show consistent dips over large depth intervals, one might conclude that the lava pile had been tilted. In Hole 917A, two inter-basaltic sedimentary horizons with preserved bedding (at 165–166 mbsf, Section 152-917A-20R-1, and at 183–184 mbsf, Section 152-917A-22R-1) show dips of 22° to 25°, whereas a tuff horizon (at 375–376 mbsf, Section 152-917A-53R-1) shows near-horizontal bedding (Fig. 21). In several lava flows, the flow-banding forms regular, parallel, evenly spaced bands having consistent dips of 15° to 30° (e.g., Unit 18, Core 152-917A-14R; Unit 52, Cores 152-917A-37R to -43R; Unit 58, Core 152-917A-54R; and Unit 70, Core 152-917A-67R; see the photographs in the "Cores" Section, this volume). Flattened vesicles give similar readings to the flow-banding, whereas flow boundaries and vesicular zones are largely irregular. The evidence from the visual inspection of the cores as a whole suggests that the lava pile has been tilted about 25°. This is consistent with the dips observed in the logging data (see "Downhole Measurements" section, this chapter).

Geopetal structures in half-filled vesicles were encountered between 200 and 240 mbsf. The flat surfaces of the vesicle fillings have a slight dip of about 5° (Fig. 24). This may have been caused by the slight deviation from the vertical of the drill string (6°). In any case, it indicates that the green clay in these vesicles was deposited after the main tilting of the lava pile.

Fracturing and Faulting

Fractures are found throughout the lava pile. They have variable orientations, and many are steep, with dips around 70° often noted. These fractures are lined and filled with secondary minerals, such as green clays, zeolites, and calcite (see "Alteration," this section).

The fracturing is more intense in the lower parts of the lava pile than in the upper. Notable fracturing, often with slickensides developed on the clay fillings, occurs between 290 and 320 mbsf (all in

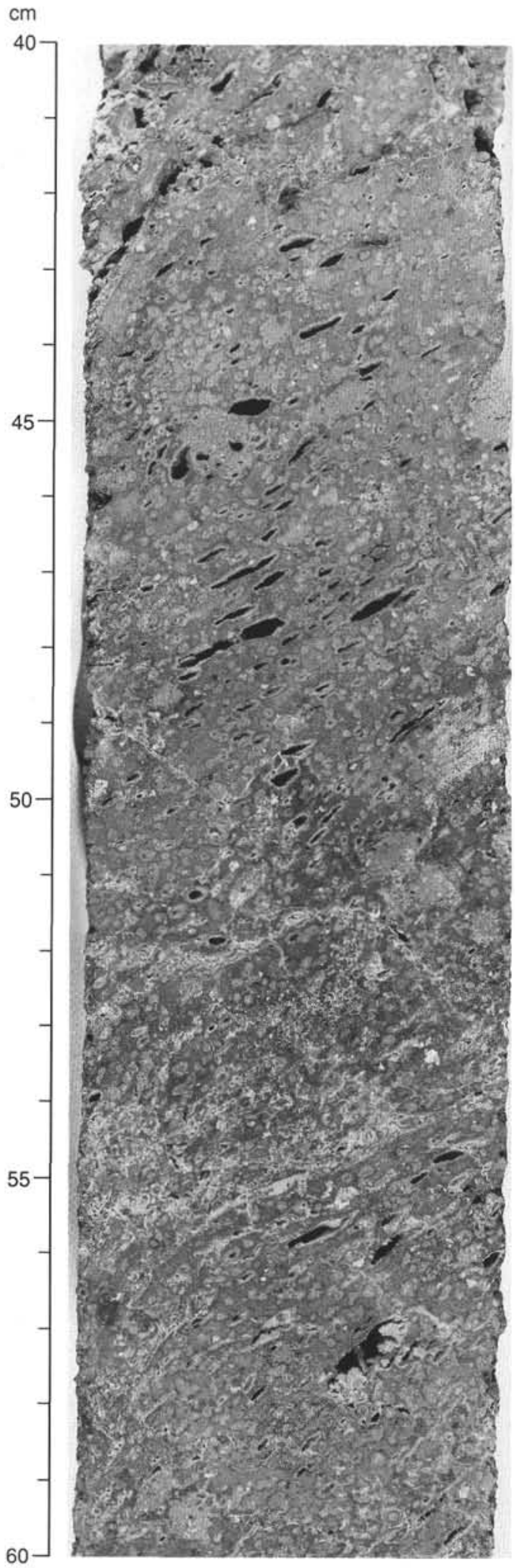

Figure 19. Dacite lava, Unit 54 (Interval 152-917A-47R-1, 40–60 cm). The top part of the lava has numerous flattened, empty vesicles, which give it a fabric dipping 20° to 30°. The original glass is hydrated and devitrified into scattered 2- to 3-mm spherules, often with a tiny vesicle in the center. The rock contains several 0.5- to 1-cm lithic clasts that are seen as light gray patches.

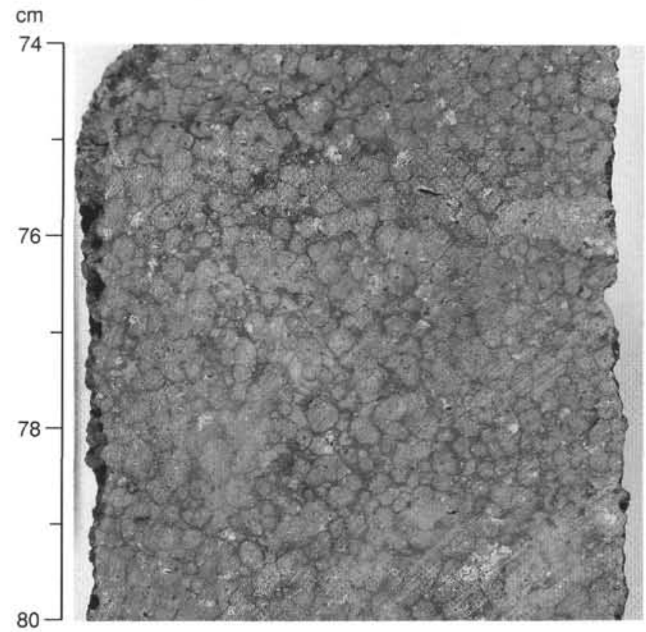

Figure 20. Dacite lava, Unit 54 (Interval 152-917A-47R-3, 74–80 cm). Near the base of the lava, no vesicles are seen and the devitrification spherules have coalesced into close-lying clusters. An elongate, 1-cm lithic clast is seen to the right at 76 cm.

Unit 52), between 443 and 445 mbsf (Unit 66), between 520 and 540, 565 and 600, 620 and 660, and below about 700 mbsf. Below 785 mbsf, fracturing and formation of slickensides is intense. In the more intensely fractured parts, the fractures often form two steep conjugate sets that tend to split the core apart (e.g., Core 152-917A-100R). The slickensides indicate mostly dip-slip movements, in some cases with a component of strike-slip, but evidence for major displacements is not apparent in the fractured rocks.

Zones in which the rocks have disintegrated into breccia or been transformed into mylonite have been interpreted as faults. Such zones occur at 538, 576 to 577, 586 to 590, and 628 to 629 mbsf. Figure 25 shows the pattern of curved fractures adjacent to the fault breccia at 538 mbsf. At 576 to 577 mbsf, a mylonite having a prominent streaky fabric and having pseudotachylyte with a waxy lustre and conchoidal fracture was observed. The breccia zones at 586 to 589 and 628 to 629 mbsf consist of completely altered angular basaltic clasts in a chloritic matrix. The rocks adjacent to the breccia zones and mylonite have been highly fractured and sheared.

The fault zone at 538 mbsf gives an anomalously high natural gamma signal (Fig. 15), whereas the other faulted zones show no such anomaly.

The observations from the core are in accordance with the seismic section (see "Pre-cruise Site Surveys" chapter, this volume), which indicates several faults below 520 mbsf. Two of the four fault zones in the core occur within single flow units and thus cannot represent major displacements of the sequence. If, however, deformation also occurred through microfaults in the fractured rocks, a considerable amount of deformation may still have taken place. It is also possible that additional faults are represented by intervals of no recovery, especially in the lowest part of the volcanic succession, where no faults were observed despite intensive fracturing. On the basis of the recovered core material, it is not possible to decide whether the contact between the volcanic rocks and the underlying sediments is faulted or is a primary depositional contact. If it is faulted, drilling encountered the sediments where these are intersected by a large, post-basaltic, 25° west-dipping normal fault (i.e., at the very crest of a faulted basement block; see "Seismic Stratigraphy" section, "Shelf Summary" chapter, this volume). If it is depositional, the drilling has

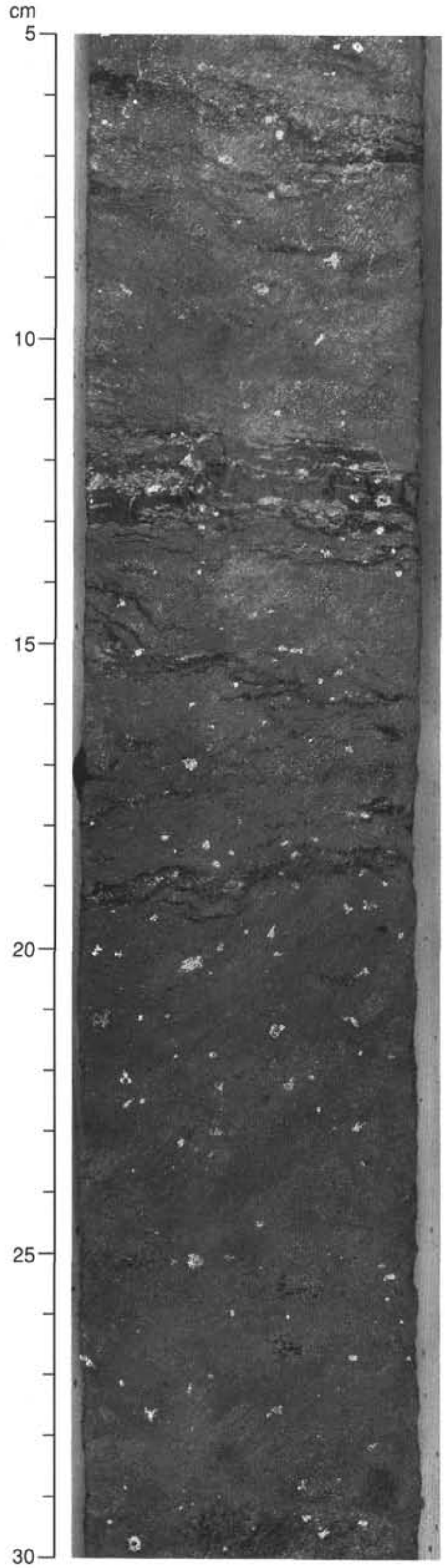

Figure 21. Ash-flow tuff, Unit 56 (Interval 152-917A-53R-1, 5–30 cm). The highly oxidized tuff is brick red with eutaxitic texture marked by streaky bands of dark and white. It contains scattered white feldspar phenocrysts.

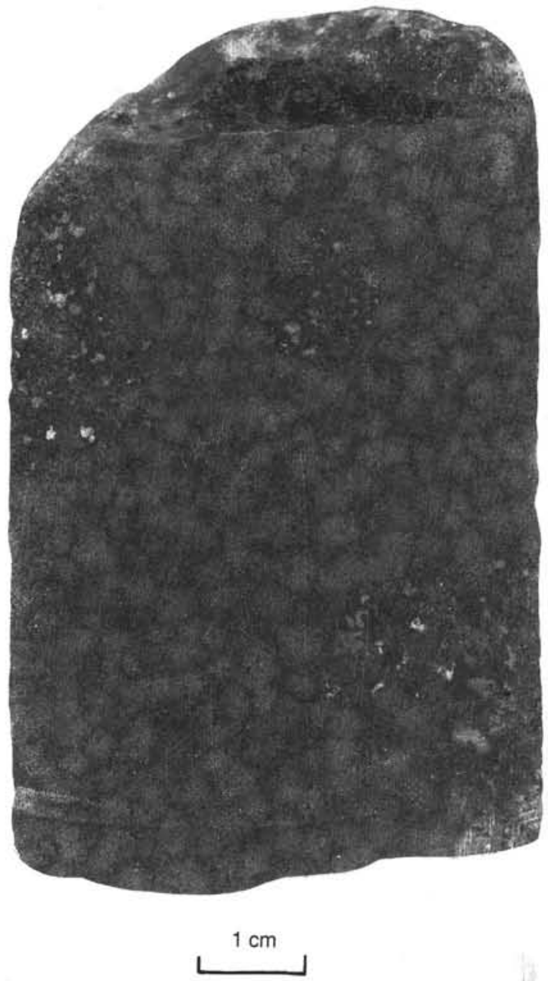

Figure 22. Aphyric-olivine basalt, Unit 84 (Interval 152-917A-88R-1, Piece 5). This very thick unit has a spotted appearance over large intervals because of its ophitic texture with large pyroxene oikocrysts. The rock also has 1- to 3-cm rounded, finely vesicular segregation patches, of which three are seen in the photograph.

encountered the sediments east of the basement crest, and the fault must cut the lowest part of the drilled volcanic succession. In either case, about 300 to 400 m of the oldest part of the volcanic succession has not been drilled.

Petrology

Sixty-six of the flow units were examined in thin section to determine their precise mineralogy and degree of alteration. Detailed descriptions are given in the "Thin Section Descriptions" Section (this volume). These studies emphasize the variety of rock types that occur within the volcanic sequence and support the division of the stratigraphy into three distinct series. The nine igneous rock types defined in the visual core descriptions were confirmed, and their descriptions and occurrences are summarized below. The thin section descriptions frequently report higher modal proportions of phenocrysts than do the core descriptions.

Picrite

The picrites recovered at Site 917 (Figs. 26 and 27) contain more than 25% modal olivine phenocrysts, some with a platy habit. A phenocryst is defined here as a crystal, larger than 0.5 mm, within a finer groundmass. Thin-section descriptions generally report a higher pro-

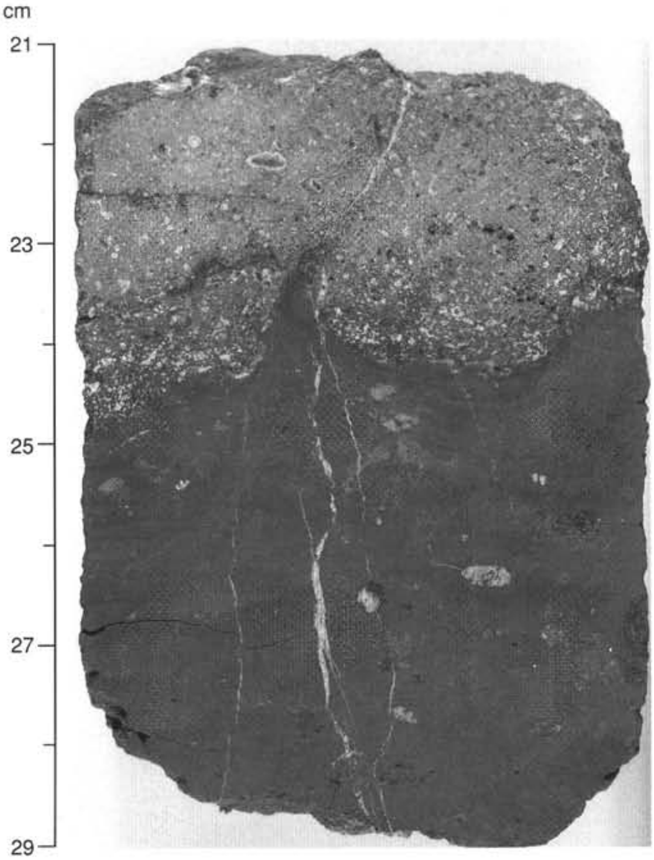

Figure 23. Red soil, Unit 61A (Interval 152-917A-56R-3, 21–29 cm). The 5-cm-thick preserved piece is brick red and shows faint, wispy, near-horizontal bedding. It contains fragments of altered feldspar and olivine crystals. The overlying lava (Unit 60) has produced load casts into the soil.

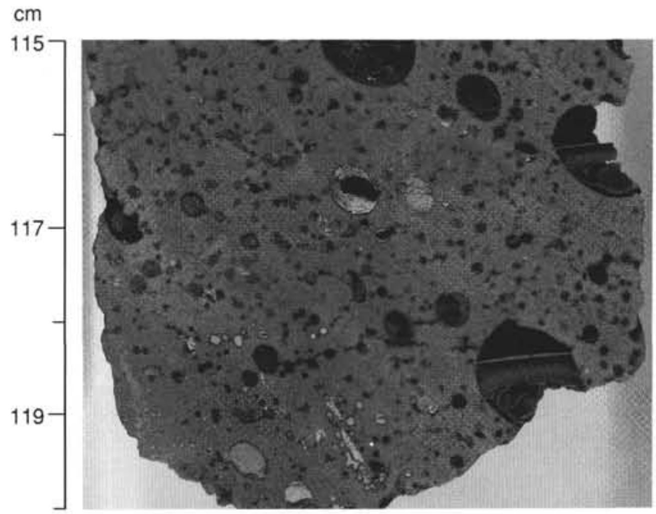

Figure 24. Geopetal structures (Interval 152-917A-25R-2, 115–120 cm). The two 1-cm vesicles to the right are half-filled with green clay, and the originally horizontal surfaces of the fillings dip around 5°. The apparent dip may reflect the deviation of the drill string from vertical.

portion of phenocrysts than are visible in hand specimen. Picrites are confined to the Upper and Lower Series. Five picrite units in the Upper Series are evenly distributed throughout the sequence and have 25% to 48% euhedral to subhedral olivine phenocrysts in a groundmass of plagioclase, clinopyroxene, and minor opaque oxide minerals. Two picrite units (Unit 61B, Fig. 27, and Unit 62) that occur near the top of the Lower Series are petrographically similar to those of the Upper Series.

Olivine-phyric Basalt

Olivine-phyric basalts contain, in thin section, less than 25% olivine phenocrysts in a matrix of plagioclase laths, subophitic clinopyroxene, and minor opaque oxide minerals. They constitute 30% of the units in the Upper Series and are a minor component of the Lower Series. Olivine phenocrysts are subhedral to euhedral and range in abundance from 15% to 22% in the Upper Series and from 8% to 10% in the Lower Series.

Aphyric Olivine Basalt

Aphyric olivine basalts are defined by the occurrence of groundmass olivine visible in hand specimen (this usually corresponds to more than 5% in thin section). These rocks generally are equigranular and are composed of subhedral olivine, plagioclase laths, ophitic to intergranular clinopyroxene, minor opaque oxide minerals, and up to 10% devitrified or altered glass. This rock type (Fig. 28) is dominant in the Upper Series (60% of the units), is absent from the Middle Series, and is common in the Lower Series. Olivine abundance is 5% to 18% in the units of the Upper Series, with the higher abundances in the uppermost part. Aphyric olivine basalts occur throughout the Lower Series, with olivine contents ranging from 10% to 20%. Excellent ophitic textures can be observed near the base of the Lower Series (Units 84, 87, 89, and 90), with clinopyroxene oikocrysts up to 5 mm in diameter.

Olivine-plagioclase-phyric Basalt

Olivine-plagioclase-phyric basalts contain more than 1% each of olivine and plagioclase phenocrysts and are confined to the Lower Series. The phenocrysts are euhedral to subhedral and are set in a groundmass of olivine, plagioclase laths, ophitic to subophitic clinopyroxene, and minor opaque oxide minerals. Phenocryst abundances are 1% to 5% olivine and 1% to 8% plagioclase. Total olivine content (phenocrysts and groundmass) is as high as 17% (Unit 86). Units 58 and 68 contain rare clinopyroxene phenocrysts. Plagioclase phenocrysts in Unit 58 are embayed. A large clast of altered gabbro is also found in this unit.

Olivine-plagioclase-clinopyroxene-phyric Basalt

Olivine-plagioclase-clinopyroxene-phyric basalts contain more than 1% each of olivine, plagioclase, and clinopyroxene phenocrysts in a matrix of olivine, plagioclase laths, clinopyroxene, and minor opaque oxide minerals. They are petrographically similar to the olivine-plagio-clase-phyric basalts, but are restricted to three units (Units 60, 70, and 72) in the Lower Series. All phenocrysts are euhedral to subhedral, with 7% to 12% plagioclase ($An_{55\text{-}60}$; up to 2 mm), 1% to 8% olivine, and 1% to 2% clinopyroxene (up to 2 mm), and show slight embayment.

Plagioclase-phyric Basalt

Plagioclase-phyric basalts are composed of plagioclase phenocrysts in a very fine-grained to glassy matrix and are restricted to the upper half of the Middle Series (Units 36–41, 43). Plagioclase abundance does not exceed 1%, and all phenocrysts exhibit disequilibrium textures (rounding, embayment). Rare clinopyroxene phenocrysts occur in Units 41 and 43.

Aphyric Basalt

Aphyric basalts contain less than about 5% olivine. They are absent from the Upper Series, dominant in the Middle Series and rare in the Lower Series (Units 74 and 75). All are relatively glassy

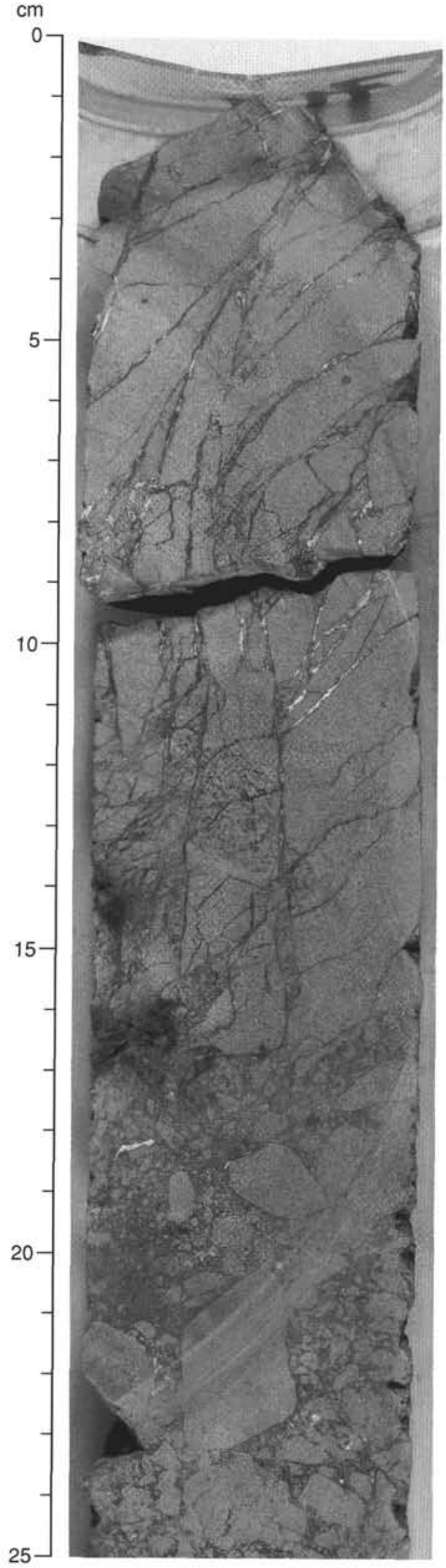

Figure 25. Intensely fractured and brecciated lava, Unit 71 (Interval 152-917A-71R-1, 0–25 cm). The curved microfaults coalesce into vertical fractures that detach downward into the brecciated fault zone below 16 cm.

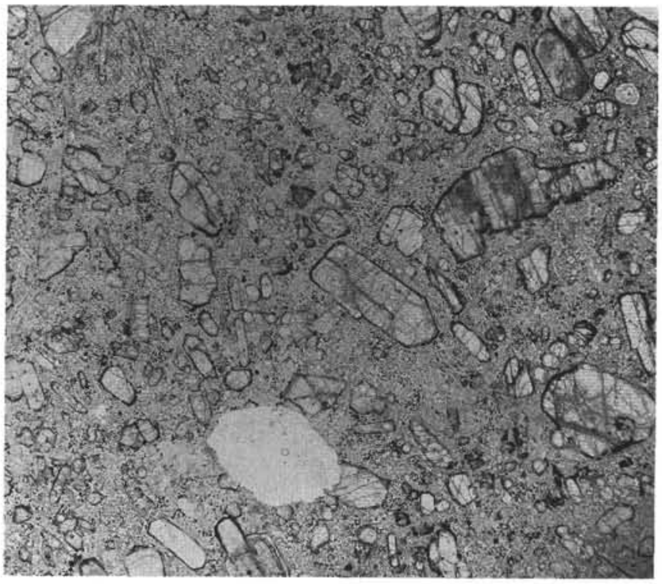

Figure 26. Photomicrograph of picrite (Interval 152-917A-20R-5, 36–38 cm [Piece 4]) from Upper Series Unit 32B, showing slightly rounded, euhedral olivine phenocrysts with chromite inclusions in a fine-grained matrix of plagioclase, augite, and altered olivine. Plane-polarized light; field of view is 23 mm wide (photograph by Barry C. Cochran).

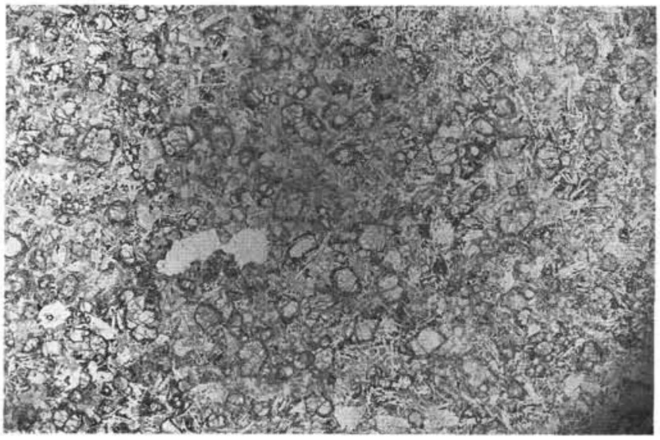

Figure 27. Photomicrograph of picrite (Sample 152-917A-57R-3, 85–86 cm [Piece 1]) from Lower Series Unit 61B, showing euhedral to subhedral olivine phenocrysts in a matrix of plagioclase, augite, and altered olivine. Plane-polarized light; field of view is 34 mm wide (photograph by Barry C. Cochran).

(30%–85% devitrified or altered glass) with plagioclase laths and very small clinopyroxene grains. Some contain occasional embayed plagioclase and clinopyroxene phenocrysts. The aphyric basalts and plagioclase-phyric basalts are petrographically similar and appear to be related by slight differences in plagioclase content.

Dacite and Tuff

Dacites (Fig. 29) and tuffs are restricted to the Middle Series. Unit 35B is a tuff composed of 26% zoned and slightly embayed plagioclase phenocrysts (An_{45-50}; up to 3 mm) and 5% clinopyroxene phenocrysts in a devitrified glassy matrix. Unit 54 (Fig. 29) is composed of a glassy, spherulitic matrix with 6% embayed plagioclase phenocrysts, 4% clinopyroxene, and rare xenocrysts of olivine and quartz. Clasts of medium-grained basaltic material incorporated into the

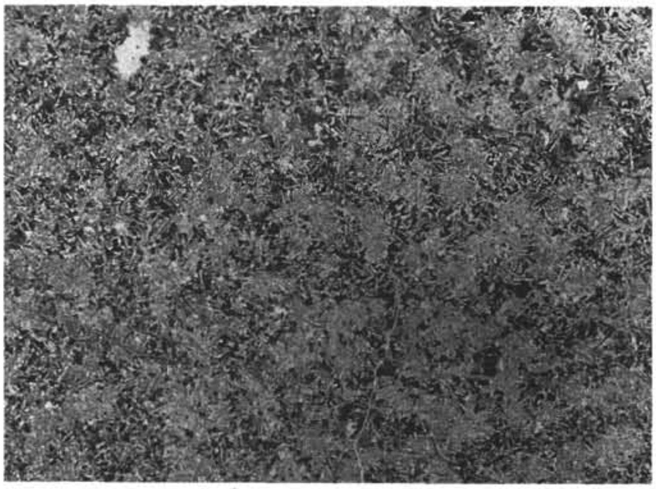

Figure 28. Photomicrograph of aphyric-olivine basalt (Sample 152-917A-99R-2, 73–74 cm [Piece 1F]) from Lower Series Unit 90, showing well-developed ophitic texture. The light gray patches are augite oikocrysts; dark gray interstitial material is altered glass. Plane-polarized light; field of view is 20 mm wide (photograph by Barry C. Cochran).

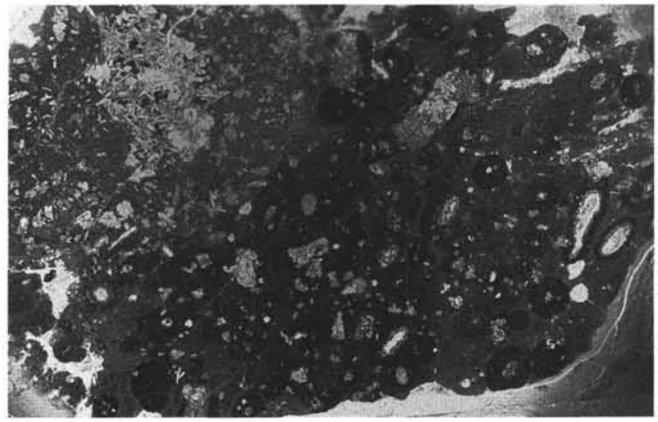

Figure 29. Photomicrograph of dacite (Sample 152-917A-47R-2, 70–72 cm [Piece 7B]) from Middle Series Unit 54, showing spherulitic texture. The upper left portion of the photomicrograph is occupied by a basalt inclusion. Plane-polarized light; field of view is 32 mm wide (photograph by Barry C. Cochran).

dacite have crenulated margins, suggesting an origin through magma mixing. Unit 56 is an oxidized dacite tuff with a few sieve-textured and rounded plagioclase and clinopyroxene phenocrysts.

Alteration

Volcanic rocks recovered from Hole 917A present variable degrees of alteration. Zeolites, green- and brown-colored clays, and calcite are the main secondary minerals (Fig. 30). All three minerals occur as vesicle fillings and in veins or fractures. Alteration products of the groundmass are clays and zeolites. Secondary minerals from the vesicles and veins were identified by hand lens or binocular microscope observations, standard shipboard XRD studies and thin section. Alteration of the phenocrysts and groundmass components was deduced only from thin-section study.

Apart from heavily weathered and brecciated zones found in some parts of the succession, most phenocrysts and groundmass minerals are relatively fresh. An exception is olivine, which commonly has a reddish Fe-hydroxide coating and is generally altered to clays (green or brownish smectites or colorless illite). Fresh olivine is preserved only in two picrites (Units 31B and 61B) and in an aphyric-olivine basalt (Unit 87). Plagioclase and glass are also frequently altered to clay or zeolite.

The massive and thicker lava flows of the Middle and Lower Series are generally fresher than the thin and more vesicular pahoehoe flows of the Upper Series. The most altered part of the sequence lies just above the sedimentary layer at 183.4 mbsf, which marks the boundary between the Upper and Middle Series. The picrite of Unit 32B and olivine-phyric basalt of Unit 33 have been completely altered to clays and zeolites and have a greasy feel. Rocks near the fault zone at 576 mbsf also have been strongly altered.

Green and brown clays are present in most basalts, as vesicle linings and alteration products of olivine, plagioclase, and glass. In the vesicles, as well as in groundmass alteration, clays are always overgrown by zeolite. The XRD patterns of the green material filling the vesicles of flows (Units 6, 21, 31, and 34) indicate that the clay is mainly smectite; however, because the powders analyzed were not pure, further XRD and transmission electron microscope (TEM) studies will be needed to determine the exact nature of the clay minerals. The presence of goethite peaks in the smectite XRD pattern from Units 32B and 67 indicates that clay alteration occurred in an oxidizing environment. The differences in color from dark brownish-

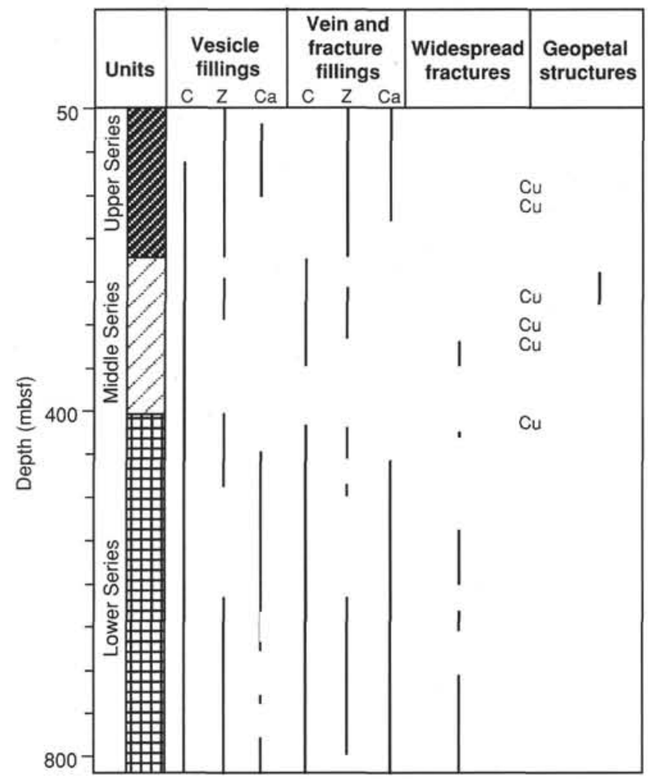

Figure 30. Distribution of secondary minerals in Hole 917A. C = clay minerals, Z = zeolites, Ca = calcite, Cu = native copper.

green to pale green are classically interpreted as reflecting changes in the Mg-Fe ratios. Some clay minerals having an intense green color, found at the base of the Upper Series, probably are celadonite. Olivine phenocrysts in the picritic and olivine-phyric lavas have been altered to colorless micalike clays (illite?).

Five different zeolites that fill or line the vesicles were identified by XRD: phillipsite, chabazite, natrolite, analcite, and scolecite. Analcite was recognized visually as euhedral crystals (icositetrahedra) lining vesicles of the olivine-rich basalts from the lower part of the Upper Series (Units 27–31). The most common zeolites seen in thin section are chabazite and natrolite. Chabazite appears as platy crystals with a pseudocubic morphology, and the characteristic feature is the presence of two sets of cleavage. Natrolite crystallizes as very fine radiating needles in close association with chabazite. The distribution of the types of zeolite in the volcanic pile does not seem to show the classical zoning pattern that is evident in the Tertiary lavas of Iceland. The three zones recognized in Iceland are, from top to bottom: chabazite + thomsonite, analcite, and mesolite + scolecite (Walker, 1960). Chabazite, natrolite, and analcite are all present between 160 and 200 mbsf in Hole 917A. The available data are not sufficient to determine a zonation with depth. However, replacement of analcite by scolecite in the vesicles of some units (Units 84 and 85) near the base of the volcanic pile seems to indicate late readjustment in response to burial-type, very low-grade metamorphism.

Calcite crystallizes with perfect prismatic habit in the larger fractures, but mostly as fan-shaped prismatic crystals or fine-grained assemblages in the smaller veins or vesicles. Close association of smectite and calcite was observed in vesicles of Units 62 to 69. In thin section, calcite was seen to replace zeolites in the vesicles and groundmass of the lavas from these same units. In general, calcite is the last mineral deposited in both vesicles and fracture zones.

Blebs of native copper were observed in voids and veins in some vesicular flow tops of the Upper Series (Units 25 and 29) or in fracture fillings in the thick Unit 52 (Middle Series) (Fig. 30). A two-stage process was proposed by LeHuray (1989) to explain native copper deposits in the lavas of the Vøring Plateau. Release of Cu from Fe-Ti oxides during subaerial weathering was followed by remobilization by seawater and precipitation as native metal.

The sequence of crystallization of the secondary minerals can be inferred to be initial alteration of the groundmass to, and lining of the vesicles with, smectites, followed by crystallization of zeolites. Calcite is the last mineral to form. Zeolites are present in the vesicles throughout the Upper Series, but clays are more abundant as secondary groundmass minerals in the olivine-rich lavas at the base of this series. In the Middle Series, zeolites are present only in the aphyric basalts of Units 48 to 51, and clays are the dominant secondary minerals in the vesicles and veins of all other units in the Middle Series (Fig. 30). This change in secondary mineral paragenesis from the Upper to the Middle Series probably reflects the change in composition of the lavas, rather than a drastic shift in the alteration processes. Some of the vesicles of the more evolved basalts (Units 44–47) have chalcedony and opal filling. Zeolites are an abundant alteration product in the Lower Series, except in the interval from 470 to 590 mbsf (Fig. 30), where calcite is dominant. The crystallization of calcite seems to be related to a late tectonic event of tilting and faulting, superimposed on the earlier late-magmatic transformation.

Zeolite assemblages found in vesicles in basaltic lavas can be used to estimate the temperature of alteration by comparison with the well-documented zeolite zonation in Iceland, calibrated by a series of drill holes (Kristmannsdóttir and Tómasson, 1978). The absence of laumontite suggests that the metamorphism of the Site 917 lavas corresponds to the low zeolite-facies zone ($T \leq 120°C$).

Stratigraphic Compositional Variation

This section summarizes the compositional variation of the lava units in the volcanic succession drilled in Hole 917A. Of the 92 igneous units identified in the succession, 64 were analyzed on board *JOIDES Resolution* by XRF methods. All of the samples were analyzed for major and trace elements (Tables 9 and 10). Procedures for sample preparation, run conditions for the spectrometer, and precision estimates based on replicate analyses of Icelandic basalt standard BIR-1 are given in the "Igneous Petrology" section of the "Explanatory Notes" chapter (this volume).

Compositional variation in the volcanic succession is closely related to stratigraphic changes in flow morphology and petrography of the lavas. This is illustrated in Figure 14, which shows the variation of Ni with depth. The Upper Series lavas are characterized by high and variable Ni contents (124–1487 ppm). All lavas in the Middle Series are differentiated with Ni <80 ppm. Lavas of the Lower Series show a wide range of composition (Ni = 67–466 ppm), but with smoother changes between units than in the Upper Series. Moreover, examination of trace-element systematics of the lavas shows that lavas erupted in the three series have distinct source characteristics and subsequent magmatic histories.

Upper Series

The Upper Series comprises intercalated picrites (Ni = 626–1487 ppm), olivine-phyric basalts (Ni = 128–438 ppm), and aphyric olivine basalts (Ni = 124–799 ppm) (Fig. 14). Although olivine phenocrysts are common in the Upper Series lavas, the presence of nearly aphyric lavas having up to 800 ppm Ni (Unit 14) and the observation that olivine phenocrysts are distributed throughout flows, not just confined to an accumulation zone at the base of the flows, suggest that the Upper Series really is dominated by lavas having primitive compositions. The only occurrence of picrites outside the Upper Series is two flows near the top of the Lower Series. The abundance of lavas having primitive compositions suggests that the Upper Series magmas made their way to the surface without extensive ponding in magma chambers. Most Upper Series lavas form pahoehoe flows, and the four identified as aa flows all have contents of Ni <170 ppm (Units 17, 18, 24, and 33).

Figure 31 shows the variation of TiO_2 with Ni in the lavas. Within the Upper Series data (filled circles), two parallel trends with different levels of TiO_2 can be observed. A few samples define a trend with relatively high TiO_2, while the main group of samples lies along a lower TiO_2 trend. In the main group, TiO_2 content increases from 0.62 to 1.50 wt% as Ni decreases from 1500 to 124 ppm, with an inflection at approximately 250 ppm Ni. This pattern can be accounted for by fractionation of olivine, followed by olivine and other phases. However, the only phenocryst phase present in Upper Series lavas is olivine; hence, the crystallization sequence is uncertain. The TiO_2 and Ni contents of the main group of Upper Series basalts are similar to those in the modern North Atlantic mid-ocean ridge basalts. Six of the Upper Series primitive (Ni >300 ppm) basalts have distinctly higher contents of TiO_2. The two groups cannot be bridged by fractionation or accumulation of any phase and thus require that there were two different parental magma compositions for the lavas. The high and low TiO_2 groups are also distinguished by their Zr/Y values. Samples having Zr/Y values greater than 2.75 are marked in Figure 31, and in the Upper Series, these correspond to the high TiO_2 group of lavas. Figure 32 shows the variation of Zr/Y with depth for lavas having more than 150 ppm Ni. The high TiO_2, high Zr/Y lavas of the Upper Series (Units 24–27, 30, 31A, and 33) all occur in a set of rapidly erupted pahoehoe lavas near the base of the Upper Series. They follow a magmatically quiescent period represented by a sediment horizon at the top of the Middle Series. Lavas having similarly high Zr/Y also erupted sporadically through the Lower Series and are generally correlated with high TiO_2 (Figs. 31 and 32). Zr/Y values are sensitive to the pressure at which mantle melting occurs because Y is compatible in garnet. Thus, the high- and low-Zr/Y groups within the Upper Series may represent parental magmas derived by different extents of melting at different depths.

Middle Series

The sediment horizon dividing the Upper and Middle Series marks a large change in lava composition and morphology. Lavas of the Middle Series are all differentiated with Ni <80 ppm and dominantly occur as aa flows. The two analyzed samples at the base of the Middle Series (Units 54 and 55) are dacitic in composition.

Compositional variation within the Middle Series appears largely controlled by fractionation, with the exception of the dacites. As Ni content declines from 80 to 10 ppm, TiO_2 decreases and Sr increases

Table 9. Shipboard X-ray fluorescence major-element analyses of Site 917 volcanic rocks.

Unit	Core, section, interval (cm)	Depth (mbsf)	SiO_2	TiO_2	Al_2O_3	Fe_2O_3	MnO	MgO	CaO	Na_2O	K_2O	P_2O_5	Total	LOI
Upper Series														
1	152-917A-6R-1, 94–96 (Piece 9)	42.64	47.56	1.18	16.16	12.53	0.17	10.45	9.49	2.22	0.47	0.07	100.27	4.79
2	152-917A-7R-1, 140–143 (Piece 22)	48.10	47.05	0.78	10.76	13.90	0.17	20.24	6.18	1.09	0.11	0.03	100.30	5.45
6	152-917A-8R-4, 11–15 (Piece 2)	60.16	47.04	1.40	15.37	13.05	0.21	10.31	10.53	1.74	0.26	0.07	99.96	4.31
7	152-917A-9R-1, 15–19 (Piece 30)	64.95	46.97	1.18	15.36	12.59	0.21	10.46	10.87	1.76	0.24	0.05	99.67	3.08
8	152-917A-9R-3, 58–63 (Piece 7A)	64.95	46.83	1.10	15.15	12.29	0.19	12.91	10.73	2.03	0.08	0.04	101.35	3.05
9	152-917A-10R-1, 66–70 (Piece 1F)	74.56	48.02	1.16	15.84	11.37	0.16	9.43	10.92	2.12	0.03	0.05	99.08	1.74
10	152-917A-10R-4, 52–56 (Piece 2B)	78.57	46.36	1.28	15.12	12.81	0.20	11.76	9.99	1.78	0.25	0.06	99.60	2.93
11	152-917A-10R-5, 121–125 (Piece 5A)	80.76	46.83	1.28	15.54	12.76	0.18	10.48	10.30	1.73	0.41	0.06	99.55	3.68
13	152-917A-11R-4, 31–35 (Piece 1B)	87.07	47.73	1.27	14.82	12.22	0.19	10.79	10.89	2.05	0.04	0.06	100.04	2.10
14	152-917A-12R-1, 35–39 (Piece 4A)	92.35	47.50	0.83	13.25	11.62	0.18	16.35	8.76	1.27	0.03	0.03	99.80	4.63
16	152-917A-13R-1, 77–81 (Piece 4)	101.87	47.02	0.92	13.07	11.35	0.17	16.50	9.00	1.30	0.07	0.05	99.44	3.65
17	152-917A-13R-5, 107–111 (Piece 10)	108.06	48.50	1.48	15.26	11.93	0.17	8.73	11.36	2.42	0.14	0.09	100.07	1.77
18	152-917A-14R-3, 97–101 (Piece 7)	113.62	48.62	1.30	15.32	11.73	0.16	8.64	11.34	1.94	0.16	0.07	99.28	1.83
18	152-917A-14R-4, 83–88 (Piece 2A)	114.52	48.29	1.31	15.36	11.85	0.18	9.29	11.08	2.00	0.10	0.07	99.51	2.70
19	152-917A-15R-2, 5–9 (Piece 1A)	120.70	47.59	1.55	14.81	12.79	0.19	9.43	11.17	1.90	0.15	0.07	99.62	2.84
21	152-917A-16R-4, 59–63 (Piece 8A)	133.13	44.34	1.12	10.34	13.63	0.21	25.35	4.07	0.70	0.02	0.07	99.84	9.51
23	152-917A-17R-2, 72–76 (Piece 2)	138.89	47.29	1.47	15.16	12.47	0.20	9.47	10.87	2.16	0.33	0.08	99.49	3.09
24	152-917A-17R-4, 73–77 (Piece 3B)	141.42	47.11	1.49	15.36	12.70	0.20	8.33	11.71	1.84	0.16	0.06	98.93	2.40
25	152-917A-18R-3, 32–36 (Piece 1)	148.90	46.86	1.69	12.02	14.11	0.23	18.09	7.92	1.42	0.13	0.12	102.57	5.51
26	152-917A-18R-4, 95–99 (Piece 7A)	150.94	47.58	1.92	13.93	13.49	0.20	10.53	10.03	1.94	0.11	0.14	99.85	3.83
27	152-917A-18R-6, 97–101 (Piece 5A)	153.91	47.00	1.87	13.55	13.26	0.18	11.69	10.33	2.15	0.18	0.14	100.34	3.93
30	152-917A-19R-2, 41–46 (Piece 1B)	157.11	46.80	1.92	13.92	13.54	0.21	10.86	9.53	1.99	0.13	0.13	99.00	2.84
31A	152-917A-19R-4, 44–48 (Piece 2B)	160.03	46.98	1.86	13.21	13.72	0.22	13.59	8.82	1.74	0.24	0.13	100.49	5.12
31B	152-917A-20R-1, 21–26 (Piece 2B)	164.71	46.08	1.47	11.52	13.47	0.18	18.41	7.36	1.28	0.13	0.10	99.97	5.01
32B	152-917A-20R-5, 36–41 (Piece 4)	170.50	44.79	0.80	10.67	11.75	0.17	23.76	6.92	0.96	0.07	0.03	99.91	3.45
33	152-917A-21R-3, 138–142 (Piece 5)	177.87	48.59	1.52	14.80	12.72	0.25	7.77	10.40	1.83	0.63	0.05	98.55	2.46
Middle Series														
34B	152-917A-23R-1, 68–73 (Piece 9)	192.58	48.69	2.73	14.04	15.07	0.22	4.79	9.74	2.80	0.40	0.20	98.68	–0.06
36	152-917A-25R-1, 82–86 (Piece 9A)	207.12	54.23	1.29	15.33	12.18	0.19	4.83	8.60	2.91	1.23	0.14	100.90	1.25
38	152-917A-26R-2, 5–11 (Piece 1)	212.32	52.88	1.59	15.51	11.94	0.16	5.84	7.83	2.99	0.69	0.17	99.59	1.16
39	152-917A-26R-2, 77–82 (Piece 12)	213.04	50.09	0.85	13.82	13.30	0.17	7.20	12.28	1.76	0.54	0.03	100.01	0.28
40	152-917A-27R-1, 70–75 (Piece 5B)	216.00	54.49	1.19	16.22	9.75	0.11	4.80	6.80	3.03	0.78	0.19	97.34	2.76
41	152-917A-27R-2, 45–50 (Piece 5)	217.22	53.21	1.30	15.27	12.23	0.13	5.59	7.60	3.01	0.73	0.09	99.13	2.47
43	152-917A-30R-1, 110–115 (Piece 15)	231.00	52.98	1.35	14.69	12.23	0.24	5.75	8.11	2.63	0.51	0.17	98.65	1.37
44	152-917A-30R-3, 37–41 (Piece 6)	233.02	56.25	1.25	15.61	10.87	0.18	4.38	6.37	3.17	0.65	0.26	98.98	2.02
46	152-917A-31R-3, 106–110 (Piece 11A)	238.66	51.16	1.51	16.39	10.55	0.20	6.70	10.08	2.68	0.46	0.12	99.83	1.79
47	152-917A-32R-3, 134–137 (Piece 13)	243.90	60.78	1.06	15.38	8.05	0.14	2.90	5.26	3.55	1.46	0.25	98.81	2.92
49	152-917A-34R-2, 41–46 (Piece 4A)	260.75												
50	152-917A-35R-2, 26–31 (Piece 1B)	265.06	51.33	1.51	16.00	10.70	0.27	6.42	10.07	2.76	0.19	0.14	99.39	1.41
52	152-917A-36R-6, 34–40 (Piece 1C)	275.56	50.26	1.48	14.77	13.21	0.16	5.84	10.03	2.64	0.39	0.13	98.89	0.94
52	152-917A-39R-3, 95–100 (Piece 6C)	296.14	51.68	1.45	14.62	12.40	0.18	4.86	9.53	2.78	0.69	0.13	98.29	0.86
54	152-917A-47R-3, 78–83 (Piece 5D)	349.41	68.12	0.64	13.77	4.27	0.12	2.11	3.27	3.24	3.44	0.03	98.99	1.49
55	152-917A-52R-1, 18–21 (Piece 5)	369.78	65.23	0.80	13.60	6.13	0.16	3.30	4.99	3.05	2.89	0.05	100.18	0.85
Lower Series														
58	152-917A-54R-5, 50–53 (Piece 1B)	390.18	49.89	1.11	16.15	10.33	0.17	6.97	12.57	2.22	0.15	0.08	99.61	2.16
60	152-917A-55R-4, 11–14 (Piece 1B)	398.05	48.78	1.55	14.71	12.15	0.17	9.25	12.11	2.06	0.12	0.12	101.01	0.12
61B	152-917A-57R-3, 81–83 (Piece 1)	416.50	45.85	1.01	13.83	11.61	0.17	16.44	10.08	1.26	0.14	0.09	100.47	4.77
62	152-917A-57R-7, 20–22 (Piece 1A)	421.49	46.33	0.95	16.04	10.72	0.16	13.59	9.85	1.77	0.46	0.08	99.92	5.35
63	152-917A-58R-2, 33–37 (Piece 1B)	423.89	50.26	1.02	15.76	10.87	0.18	8.90	11.24	2.10	0.10	0.07	100.50	1.45
66	152-917A-61R-2, 54–59 (Piece 1D)	443.16	50.09	1.17	15.81	10.82	0.17	7.31	11.94	2.29	0.21	0.09	99.88	2.36
68	152-917A-64R-1, 125–130 (Piece 5G)	471.95	48.79	1.41	15.52	11.14	0.16	7.94	12.19	1.91	0.29	0.13	99.47	1.61
70	152-917A-67R-4, 106–110 (Piece 5A)	504.99	52.24	1.49	15.29	11.33	0.16	5.81	9.96	2.74	0.76	0.18	99.93	0.73
71	152-917A-69R-2, 90–94 (Piece 3D)	521.20	52.01	1.25	15.58	10.46	0.15	7.12	10.23	2.36	0.49	0.12	99.75	1.90
73A	152-917A-72R-1, 90–96 (Piece 3E)	548.20	47.05	1.49	13.31	12.86	0.20	13.33	9.85	1.56	0.35	0.09	100.06	6.88
76	152-917A-78R-2, 136–138 (Piece 4B)	597.99												
78	152-917A-79R-2, 91–95 (Piece 1E)	607.35	49.01	0.93	15.61	11.16	0.20	11.84	9.65	1.78	0.15	0.10	100.42	4.30
79	152-917A-80R-4, 102–106 (Piece 1D)	619.91	49.69	1.19	16.32	11.17	0.16	7.86	10.29	2.32	0.33	0.13	99.43	2.84
82	152-917A-83R-3, 14–18 (Piece 1B)	646.89	49.79	1.08	16.29	10.68	0.16	8.19	10.40	2.12	0.25	0.11	99.05	2.72
83	152-917A-84R-2, 95–99 (Piece 3D)	655.95	49.56	1.14	16.44	11.25	0.18	8.71	9.88	2.59	0.29	0.13	100.14	3.03
84	152-917A-86R-3, 66–70 (Piece 1D)	675.99	49.23	1.06	16.09	10.41	0.15	8.75	11.15	2.10	0.29	0.11	99.33	2.17
85	152-917A-90R-1, 41–45 (Piece 2A)	710.51	48.30	1.06	15.89	11.24	0.18	9.31	11.55	1.87	0.17	0.10	99.66	3.66
86	152-917A-90R-5, 52–56 (Piece 1B)	715.60	48.56	1.08	15.62	11.18	0.17	9.43	11.52	2.09	0.19	0.12	99.95	3.32
87	152-917A-92R-4, 5–10 (Piece 5)	727.44	48.38	1.09	16.19	11.09	0.14	9.31	10.45	2.33	0.16	0.13	99.25	4.08
88	152-917A-96R-1, 128–132 (Piece 10B)	760.68	47.29	1.42	14.54	12.16	0.24	12.33	10.03	1.49	0.09	0.10	99.67	5.24
89	152-917A-97R-2, 42–44 (Piece 1B)	770.67	48.98	1.17	16.70	10.92	0.15	7.31	11.85	2.00	0.16	0.13	99.35	4.34
90	152-917A-99R-2, 78–80 (Piece 1F)	790.55												
91	152-917A-100R-1, 104–108 (Piece 1F)	799.04	48.92	1.17	16.44	9.36	0.20	6.43	14.26	2.03	0.16	0.14	99.09	4.09
92	152-917A-101R-4, 81–85 (Piece 5)	812.24	50.24	1.16	16.24	9.49	0.20	8.13	12.55	2.24	0.19	0.13	100.53	3.32

Note: Values are in weight percent. LOI = loss on ignition. Analysts were Don Sims and Mary Ann Cusimano.

sharply in the basalts (Figs. 31 and 33). These trends suggest that saturation with a Ti-bearing oxide mineral was reached at about 1.5 wt% TiO_2 and 80 ppm Ni and that oxide-mineral fractionation continued through the differentiation of the Middle Series basalts. The only exception is Unit 34B, the uppermost lava in the Middle Series, which has 2.7 wt% TiO_2. The steep increase in Sr in the basalts indicates that significant fractionation of plagioclase did not begin before the magma had nearly 600 ppm Sr (Fig. 33). The lavas are either aphyric or contain only very sparse plagioclase phenocrysts.

A gap in composition is seen between the most differentiated basalt and the dacites (Figs. 31 and 33). The dacites are mixed rocks that contain abundant partially digested xenoliths of basalt and occasional partially resorbed quartz and feldspar crystals. The lobate margins of some of the basalt xenoliths suggest that mixing of basaltic and silicic liquids may have been involved during generation of the dacitic magma. Dacites have also been found in Hole 642E on the Vøring Plateau (Parson et al., 1989), in commercial wells in the Rockall Trough (Morton et al., 1988), and in the Faeroe-Shetland

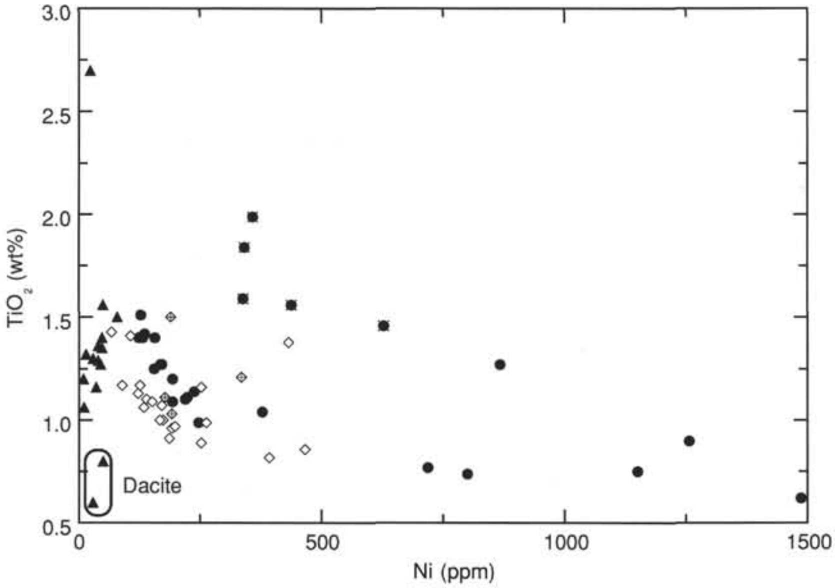

Figure 31. Diagram of TiO_2 vs. Ni. Solid circles = Upper Series, solid triangles = Middle Series, and open diamonds = Lower Series. The crossed circles and diamonds are basalts with Zr/Y values >2.75 and Ni values >150 ppm from the Upper and Lower Series, respectively. The dacites of the Middle Series are circled.

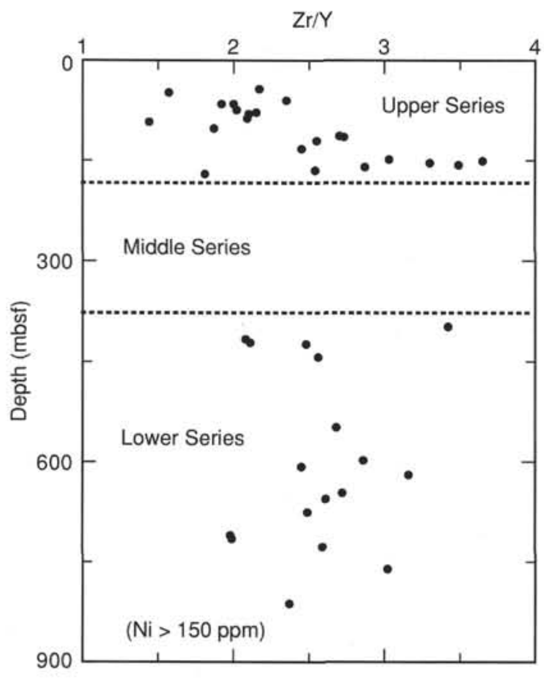

Figure 32. Diagram of Zr/Y vs. depth for basalts with Ni >150 ppm. Lines are not drawn between the points because samples with Ni <150 ppm have been omitted.

Basin (Kanaris-Sotiriou et al., 1993). The peraluminous character of these dacites suggests that they were generated through melting or assimilation of pelitic sediment. Metaluminous granophyre bodies within the East Greenland Tertiary macrodike complex have been shown by Blichert-Toft et al. (1992) to be hybrid rocks formed by mixing basaltic magma with melts from the granitic basement. The Middle Series dacites, which are also metaluminous, may have been formed in a similar way.

Lower Series

The Lower Series is characterized by cyclic variation in Ni content (Fig. 14). Basalts having the highest Ni (252–466 ppm) occur around 420, 550, 775, and 810 mbsf (Units 61B and 62, 73A and 78, 88, and 92), form pahoehoe flows, and five of the six units contain picrites or olivine-phyric basalts. The four peaks are separated by more differentiated lavas (Ni = 67–197 ppm) that show a relatively smooth progression of decreasing then increasing Ni between the peaks. This pattern contrasts with the flow-to-flow oscillations in composition evident in the Upper Series. Only two Lower Series basalts (Units 70 and 71) are as differentiated as the Middle Series basalts. These cyclic variations in composition, coupled with the large average size of Lower Series lava flows, may indicate the presence of relatively large and long-lived magma chambers.

Figure 31 shows the variation of TiO_2 with Ni in the lavas. Most of the Lower Series basalts (diamonds) follow a single trend at relatively low TiO_2 contents, although a few samples appear to follow a parallel trend at slightly higher TiO_2. The basalts on the higher-TiO_2 trend generally have higher Zr/Y values as well (Fig. 31). In the main group of Lower Series basalts, TiO_2 increases from 0.86 to 1.5 wt% as Ni decreases from 466 to 67 ppm, with an inflection at about 200 ppm Ni. Below 200 ppm Ni, the main group of Lower Series basalts lie on a trend having a shallower slope than the main group of Upper Series basalts (Fig. 31), indicating a slightly different liquid line of descent. The porphyritic lavas in the Lower Series show that the crystallization sequence is olivine, olivine + plagioclase, olivine + plagioclase + clinopyroxene, with plagioclase saturation reached at approximately 200 ppm Ni and 0.9 wt% TiO_2, and clinopyroxene at approximately 70 ppm Ni and 1.4 wt% TiO_2.

The behavior of alkalis and alkaline earths in the Lower Series is markedly different from that in the Upper Series and is demonstrated in Figure 33 by Sr. Between 500 and 100 ppm Ni, Sr varies from 100 to 200 ppm in the Upper Series and from 175 to 675 ppm in the Lower Series. Furthermore, no correlation is seen between Sr and Ni or phenocryst assemblage in the Lower Series samples. Despite the appearance of plagioclase phenocrysts in some Lower Series basalts, no decrease in Sr can be observed. These observations are not readily explainable by any crystallization processes and appear to require derivation of Lower Series magmas from a different mixture of sources and contaminants than the Upper Series magmas.

Magma Sources and Contaminants

Figure 34 shows the variation of Ba/Zr values with depth. Both elements are sufficiently incompatible that Ba/Zr values do not change much during differentiation of the basalts. Thus, Ba/Zr tracks enrich-

Table 10. Shipboard X-ray fluorescence trace-element analyses of Site 917 volcanic rocks.

Unit	Core, section, interval (cm)	Depth (mbsf)	TiO_2	V	Cr	Ni	Cu	Zn	Rb	Sr	Y	Zr	Nb	Ba	Ce
Upper Series															
1	152-917A-6R-1, 94–96 (Piece 9)	42.64	1.04	292	690	378	110	79	7.8	201.5	26.5	57.5	1.9	71	4
2	152-917A-7R-1, 140–143 (Piece 22)	48.10	0.62	151	1422	1487	68	80	6.0	61.5	22.2	34.9	0.1	30	0
6	152-917A-8R-4, 11–15 (Piece 2)	60.16	1.25	333	277	156	131	76	6.1	163.9	26.9	63.3	2.3	39	4
7	152-917A-9R-1, 15–19 (Piece 3)	64.95	1.09	304	359	194	59	74	6.9	95.9	26.1	52.2	1.0	72	6
8	152-917A-9R-3, 58–63 (Piece 7A)	64.95	0.99	272	383	247	124	72	4.3	110.9	26.0	49.9	1.0	33	2
9	152-917A-10R-1, 66–70 (Piece 1F)	74.56	1.10	311	421	220	99	72	4.7	128.7	25.8	52.1	1.4	12	3
10	152-917A-10R-4, 52–56 (Piece 2B)	78.57	1.14	330	387	238	150	77	5.0	120.9	26.0	55.9	1.2	37	4
11	152-917A-10R-5,121–125 (Piece 5A)	80.76	1.20	321	350	193	144	77	6.5	159.2	25.9	54.4	1.8	33	6
13	152-917A-11R-4, 31–35 (Piece 1B)	87.07	1.11	286	365	223	126	74	4.6	116.1	26.4	55.1	1.2	20	3
14	152-917A-12R-1, 35–39 (Piece 4A)	92.35	0.74	235	1016	799	74	70	5.2	52.0	24.5	35.2	0.0	9	1
16	152-917A-13R-1, 77–81 (Piece 4)	101.87	0.77	214	1085	718	76	69	5.3	83.0	24.3	45.5	0.1	42	3
17	152-917A-13R-5,107–111 (Piece 10)	108.06	1.40	379	239	124	88	83	4.6	138.3	27.8	79.4	3.3	75	11
18	152-917A-14R-3, 97–101 (Piece 7)	113.62	1.27	340	282	169	74	79	4.7	135.0	26.9	72.7	1.4	82	10
18	152-917A-14R-4, 83–88 (Piece 2A)	114.52	1.27	330	285	171	107	78	4.2	132.1	26.9	73.5	2.3	62	16
19	152-917A-15R-2, 5–9 (Piece 1A)	120.70	1.40	400	279	157	105	77	4.7	123.8	27.1	69.2	2.1	32	7
21	152-917A-16R-4, 59–63 (Piece 8A)	133.13	0.90	222	998	1257	62	76	5.1	22.6	23.8	58.4	2.3	24	4
23	152-917A-17R-2, 72–76 (Piece 2)	138.89	1.40	379	230	132	138	78	5.6	187.9	26.5	72.1	2.2	41	5
24	152-917A-17R-4, 73–77 (Piece 3B)	141.42	1.42	379	252	135	96	80	5.4	149.5	26.3	93.1	2.3	39	8
25	152-917A-18R-3, 32–36 (Piece 1)	148.90	1.46	383	753	626	86	89	6.9	100.2	27.3	82.7	3.7	48	8
26	152-917A-18R-4, 95–99 (Piece 7A)	150.94	1.84	476	485	342	153	90	5.2	139.7	29.8	108.8	4.9	44	15
27	152-917A-18R-6, 97–101 (Piece 5A)	153.91	1.59	406	456	339	94	87	9.1	134.5	29.1	96.1	4.9	49	14
30	152-917A-19R-2, 41–46 (Piece 1B)	157.11	1.99	554	624	359	99	92	6.0	134.4	29.4	102.5	5.2	54	15
31A	152-917A-19R-4, 44–48 (Piece 2B)	160.03	1.56	386	518	438	116	88	9.8	119.5	28.5	81.7	4.4	67	14
31B	152-917A-20R-1, 21–26 (Piece 2B)	164.71	1.27	328	995	866	103	83	8.0	92.0	26.2	66.6	3.5	40	9
32B	152-917A-20R-5, 36–41 (Piece 4)	170.50	0.75	170	1694	1150	88	67	6.6	78.8	22.3	40.3	1.1	23	0
33	152-917A-21R-3,138–142 (Piece 5)	177.87	1.51	377	274	128	150	77	10.8	133.9	26.1	78.0	2.6	69	11
Middle Series															
34B	152-917A-23R-1, 68–73 (Piece 9)	192.58	2.70	950	18	24	41	114	5.8	334.3	31.0	144.4	6.2	362	46
36	152-917A-25R-1, 82–86 (Piece 9A)	207.12	1.30	347	17	30	47	95	37.6	462.0	26.9	133.8	5.6	405	54
38	152-917A-26R-2, 5–11 (Piece 1)	212.32	1.29	319	23	40	55	95	12.5	438.5	25.8	139.4	5.0	475	49
39	152-917A-26R-2, 77–82 (Piece 12)	213.04	0.90	300	120	73	87	81	35.8	56.9	27.3	37.4	1.1	12	0
40	152-917A-27R-1, 70–75 (Piece 5B)	216.00	1.16	242	22	36	46	96	11.0	576.5	25.0	163.1	6.0	486	70
41	152-917A-27R-2, 45–50 (Piece 5)	217.22	1.27	289	26	45	61	115	14.1	499.3	25.1	142.3	5.7	310	49
43	152-917A-30R-1,110–115 (Piece 15)	231.00	1.36	329	18	40	80	101	11.0	366.4	26.1	146.8	5.0	688	49
44	152-917A-30R-3, 37–41 (Piece 6)	233.02	1.20	246	6	10	24	94	15.9	549.4	26.2	212.7	7.8	559	89
46	152-917A-31R-3,106–110 (Piece 11A)	238.66	1.50	432	37	79	151	103	6.7	323.7	26.3	94.7	3.8	199	24
47	152-917A-32R-3,134–137 (Piece 13)	243.90	1.06	180	12	10	25	86	36.6	540.1	25.4	218.1	7.3	743	94
49	152-917A-34R-2, 41–46 (Piece 4A)	260.75	1.32	323	8	16	36	99	9.7	569.3	25.7	184.4	6.5	576	72
50	152-917A-35R-2, 26–31 (Piece 1B)	265.06	1.56	429	20	50	206	77	5.4	404.5	25.9	56.4	4.3	205	29
52	152-917A-36R-6, 34–40 (Piece 1C)	275.56	1.40	376	18	48	89	103	9.9	373.2	27.5	101.4	3.5	249	26
52	152-917A-39R-3, 95–100 (Piece 6C)	296.14	1.35	394	16	48	83	97	15.3	350.9	27.5	105.0	2.9	291	25
54	152-917A-47R-3, 78–83 (Piece 5D)	349.41	0.60	75	47	30	40	85	40.5	109.7	30.8	376.8	14.7	1199	119
55	152-917A-52R-1, 18–21 (Piece 5)	369.78	0.80	127	87	50	59	75	53.2	124.7	29.5	303.3	12.4	992	91
Lower Series															
58	152-917A-54R-5, 50–53 (Piece 1B)	390.18	1.10	287	234	140	106	72	4.9	310.8	24.8	59.6	2.3	143	11
60	152-917A-55R-4, 11–14 (Piece 1B)	398.05	1.50	393	309	189	133	73	4.9	183.5	26.8	91.6	7.6	84	16
61B	152-917A-57R-3, 81–83 (Piece 1)	416.50	0.86	188	586	466	57	68	6.1	170.1	22.6	47.0	5.4	83	8
62	152-917A-57R-7, 20–22 (Piece 1A)	421.49	0.82	175	524	392	88	64	11.6	301.0	22.2	46.9	5.0	294	10
63	152-917A-58R-2, 33–37 (Piece 1B)	423.89	1.07	259	288	171	121	70	4.3	251.4	24.4	60.6	2.4	115	16
66	152-917A-61R-2, 54–59 (Piece 1D)	443.16	1.09	262	207	152	92	76	5.5	271.7	25.4	64.9	2.2	132	13
68	152-917A-64R-1, 125–130 (Piece 5G)	471.95	1.41	333	240	107	107	74	7.8	228.3	26.1	93.3	8.3	138	17
70	152-917A-67R-4, 106–110 (Piece 5A)	504.99	1.43	324	75	67	67	79	9.4	331.8	27.5	143.3	15.7	397	40
71	152-917A-69R-2, 90–94 (Piece 3D)	521.20	1.17	278	54	90	104	80	6.5	278.8	26.6	115.9	4.3	285	24
73A	152-917A-72R-1, 90–96 (Piece 3E)	548.20	1.38	420	786	432	121	77	11.4	202.7	26.3	70.4	2.5	566	16
76	152-917A-78R-2, 136–138 (Piece 4B)	597.99	1.03	274	281	192	93	74	8.5	657.9	25.9	74.2	2.5	411	23
78	152-917A-79R-2, 91–95 (Piece 1E)	607.35	0.89	255	405	252	85	74	4.9	286.5	24.3	59.6	2.4	173	18
79	152-917A-80R-4, 102–106 (Piece 1D)	619.91	1.11	311	167	177	127	79	4.4	342.1	25.8	81.5	2.9	226	18
82	152-917A-83R-3, 14–18 (Piece 1B)	646.89	1.00	291	136	174	97	75	4.3	341.7	25.2	68.6	2.3	205	18
83	152-917A-84R-2, 95–99 (Piece 3D)	655.95	1.00	280	120	167	101	69	4.9	313.1	25.2	65.7	2.9	275	20
84	152-917A-86R-3, 66–70 (Piece 1D)	675.99	0.96	262	300	192	110	72	4.7	310.7	24.9	62.1	2.5	218	18
85	152-917A-90R-1, 41–45 (Piece 2A)	710.51	0.97	259	410	198	92	71	6.0	410.8	24.8	49.0	1.2	256	13
86	152-917A-90R-5, 52–56 (Piece 1B)	715.60	0.91	252	368	186	69	71	3.9	378.3	25.1	50.0	1.1	189	13
87	152-917A-92R-4, 5–10 (Piece 1)	727.44	0.99	260	416	262	74	77	4.3	318.8	24.7	64.0	2.4	220	14
88	152-917A-96R-1, 128–332 (Piece 10B)	760.68	1.21	322	558	334	117	68	3.9	318.1	25.9	78.1	3.4	95	7
89	152-917A-97R-2, 42–44 (Piece 1B)	770.67	1.06	280	264	135	73	71	5.4	490.2	25.0	62.9	2.0	439	21
90	152-917A-99R-2, 78–80 (Piece 1F)	790.55	1.13	296	266	122	110	73	3.8	372.5	26.1	66.8	1.3	161	14
91	152-917A-100R-1, 104–108 (Piece 1F)	799.04	1.17	293	279	126	93	73	3.8	389.7	25.0	67.2	1.9	208	18
92	152-917A-101R-4, 81–85 (Piece 5)	812.24	1.16	302	678	252	115	80	4.2	360.0	25.5	60.4	3.6	168	18

Notes: Analysts were Don Sims and Mary Ann Cusimano. Values are in parts per million except for TiO_2 (weight percent).

ment of alkalies and alkaline earths in the source regions or contaminants of the magmas. Both the Upper and Middle Series basalts have relatively restricted, but different, ranges of Ba/Zr values (except for Unit 43 in the Middle Series). In contrast, Lower Series basalts display a wide range of Ba/Zr values (Fig. 34). The enrichment in Sr (Fig. 33) and Ba in the Lower Series samples is not likely to be the result of alteration. Ba and Sr correlate well with Zr (which is immobile during alteration) in both the Upper and Middle Series basalts. The Lower Series lavas, on average, are less altered than those of the Upper Series, but do show a similar degree of alteration to the Middle Series lavas. We suggest that this enrichment in alkaline earths may result from contamination by components from the continental lithosphere. With the data available, it is not possible to determine whether lithospheric mantle or crust is the culprit. Uniformly low Ba/Zr values (Fig. 34) in the Upper Series basalts indicate that the lithospheric component was no longer contributing to the magmas at that time.

Figure 35 shows the variation of Zr/Nb values with Zr in all the lavas. Zr/Nb values vary from 10 to 50, and the complete range is

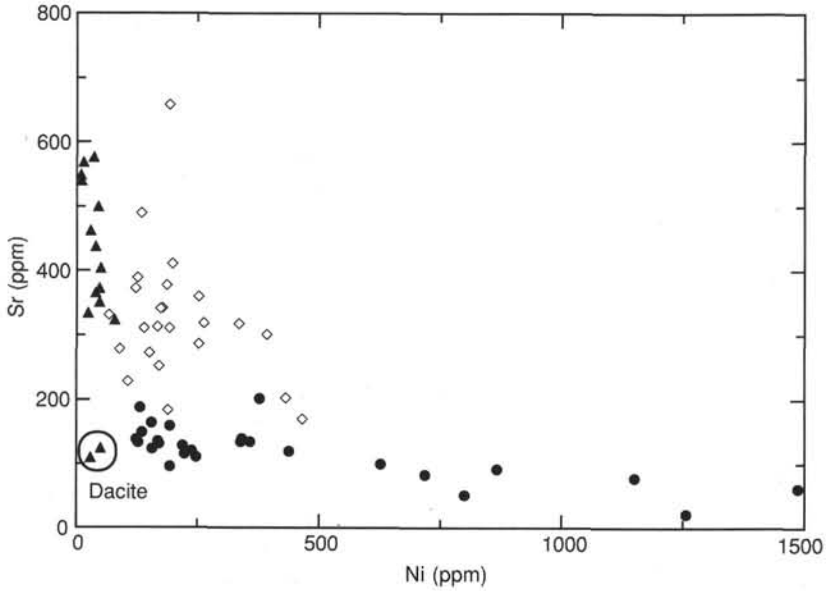

Figure 33. Diagram of Sr vs. Ni. Solid circles = Upper Series, solid triangles = Middle Series, and open diamonds = Lower Series. Dacites of the Middle Series are circled.

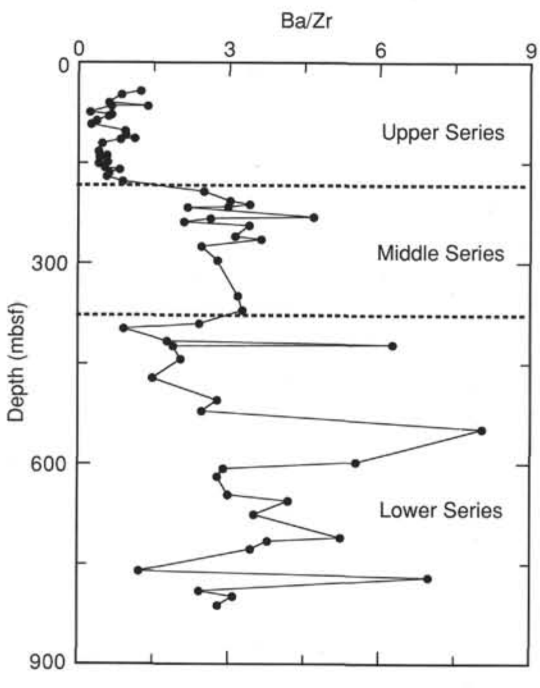

Figure 34. Diagram of Ba/Zr vs. depth.

shown by Lower Series basalts. The Upper Series basalts have Zr/Nb values that range from 18 to 50. Both Zr and Nb are incompatible, so Zr/Nb is little affected by low-pressure fractional crystallization. Furthermore, because little correlation exists between Zr/Nb and Ba/Zr values, Zr-Nb ratios may be relatively unaffected by lithospheric contamination. We postulate that Zr/Nb values may reflect depletion of the mantle source region and that the high values presented here indicate an important role for depleted mantle source regions for generating almost all of the magmas. The values measured in the Upper Series basalt and picrite lavas are similar to those found in normal MORB (Sun et al., 1979). The lowest Zr/Nb values occur near the top of the Lower Series (Units 60, 61B, 62, 68, and 70). Thus, if low Zr/Nb values do reflect a contribution from undepleted mantle, then no smooth stratigraphic progression occurs in the compositions of the mantle regions tapped during melting.

Style of Magmatism

The abrupt change in magma composition at the sediment horizon separating the Upper and Middle Series coincides with a marked change in the style of magma storage, evolution, and eruption. The Lower and Middle Series magmas appear to have evolved in large, long-lived reservoirs. These were periodically replenished, as shown by peaks in the Ni content (Fig. 14), but the overall trend is toward more evolved compositions with time. This trend culminated in the eruption of the evolved magmas of the Middle Series. Such long-term evolution of magma composition is inconsistent with evolution in small, temporary reservoirs. The flow units of the Lower and Middle Series tend to be thick (22 flows over 10 m, five flows over 20 m) and are probably extensive. These thick flows also tend to be moderately evolved in composition and, judging from their incompatible-element concentrations, would have been the product of at least 50% fractional crystallization from a parental olivine basalt magma. Large storage systems would be needed to accommodate the volumes of parental magma involved.

By contrast, the Upper Series units tend to be thin pahoehoe flows of magnesian basalt. Rapid oscillations in Ni content (Fig. 14) imply short-term storage in smaller reservoirs accompanied by crystallization and accumulation of olivine phenocrysts. Evolved magmas are absent from the Upper Series.

The indeterminate time interval represented by the sediment horizon (Unit 34A, between the Middle and Upper Series) saw the demise of a system of magma reservoirs that had been in operation throughout the Lower and Middle Series. A new system was established in which magma was transported rapidly from the mantle to the surface in small conduits. All three series include thin pahoehoe flows, so the center of eruption could not have moved very far during this interval. The simplest explanation for these changes would be a transition from a plumbing system based on large sill complexes to one dominated by dikes. It is tempting to speculate that this transition might mark the final phase of the breakup of the southeast Greenland margin.

Summary and Conclusions

Hole 917A penetrated the landward edge of the southeast Greenland SDRS all the way to the tectonic breakup unconformity, and the

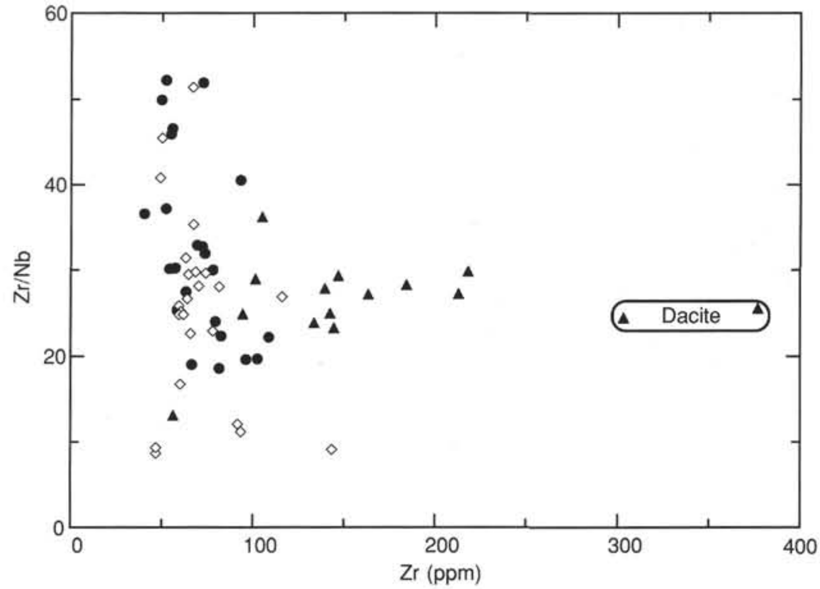

Figure 35. Diagram of Zr/Nb vs. Zr. Solid circle = Upper Series, solid triangles = Middle Series, and open diamonds = Lower Series. Dacites of the Middle Series are circled.

cores recovered have preserved a unique record of the structure and composition of such a volcanic sequence. However, because the breakup unconformity was penetrated at, or very near, a faulted contact (see Fig. 1, "Shelf Stratigraphic Summary" chapter, this volume), the lowermost part of the volcanic sequence was not recovered at Site 917. The main points to emerge from shipboard studies of the volcanic rocks are summarized as follows:

1. The 778.9 m succession is composed of at least 92 volcanic units, divisible into three stratigraphic series: an Upper (olivine basalt and picrite) Series, a Middle (evolved) Series, and a Lower (basaltic) Series. The Middle and Upper Series are separated by a thin (67 cm recovered) fluvial sandstone unit.
2. The volcanic units are mostly lava flows that range from thin pahoehoe to thick, massive aa flows, but include at least two pyroclastic units, one of them a welded ash-flow tuff. One unit is an inclined intrusive basalt sheet.
3. The thickness of the lava flows tends to increase downward through the sequence; the Upper Series is dominated by thin pahoehoe flows, the Middle Series by aa flows, and the Lower Series consists of alternating pahoehoe and aa flows.
4. The entire sequence was erupted subaerially judging by the common presence of red, oxidized flow tops and scattered intercalated red soil horizons. Hyaloclastite breccia at the base of two flows may have been caused by lava flowing into shallow water or onto a wet surface.
5. The lava sequence dips at about 25°. The lower 280 m of the sequence is highly fractured and brecciated in places as a result of faulting. One fault (at 576.5 mbsf) is marked by a mylonite zone.
6. The rock types range from picrite to dacite, with aphyric lavas more common than porphyritic types. The sequence of phenocryst assemblages seen in the Lower and Middle Series lavas is olivine, olivine + plagioclase, olivine + plagioclase + augite(± magnetite), plagioclase + augite + magnetite (in dacite).
7. Three dacite flows at the base of the Middle Series contain abundant basalt xenoliths, often with lobate margins. These, together with the disequilibrium phenocryst assemblage, suggest magma mixing. The dacites are not peraluminous.
8. Alteration ranges from slight to complete; the thick flows of the Lower Series are generally fresher than the thin flows of the Upper Series.
9. Distribution of zeolite species is not systematic and the assemblage indicates that the temperature was probably not over 120°C. Calcite was superimposed on the earlier zeolite-clay assemblage and seems to be associated with the later tilting and faulting of the lava sequence.
10. Upper Series lavas have high Zr/Nb values (18–50) and low concentrations of Ba and Rb, comparable with values from MORBs, which suggests derivation from a depleted MORB-like mantle source.
11. High Ba/Zr values in the Lower and Middle Series suggest variable interaction between the earlier magmas and the continental lithosphere. The Upper Series lavas show no evidence for such contamination.
12. Systematic variations in composition with stratigraphic height in the sequence suggest that the Lower and Middle Series magmas evolved in large, long-lived reservoirs. Rapid oscillations in Ni content in the Upper Series lavas imply short-term storage in smaller reservoirs.

PHYSICAL PROPERTIES

Introduction

The excellent recovery of basalts and a successful downhole logging program at Hole 917A provide an opportunity to quantitatively link specific hard rock lithologies to their physical properties and MST signatures, and precise downhole location.

All cores were processed through the MST for GRAPE bulk density, natural gamma, and magnetic susceptibility. Selected discrete samples were measured for bulk and grain density, compressional *P*-wave velocity, and thermal conductivity. The Leg 152 cruise was the first time that the new natural gamma detector on the MST (installed during Leg 149) was used to evaluate basalts. As explained in detail below, the data generated with this system are useful for separating distinct lava flows and for grouping flows of similar physical properties. The MST data also are extremely useful for correlating recovered rocks with downhole logging stratigraphy.

Multisensor Track (MST)

On the basis of the MST data, Hole 917A may be divided into eight distinct mechanical units (Fig. 15). Mechanical Unit M1 comprises all the soft sediments recovered from Hole 917A (lithologic Units I–III). Mechanical Units M2 through M7 comprise lavas (basalts and dacites of the Upper, Middle, and Lower Series) and interbedded sediments (lithologic Unit IV). Mechanical Unit M8 comprises clastic and low-grade metamorphic sediments recovered at the bottom of Hole 917A (lithologic Units V–VI). Within the lava pile, numerous inflections can be correlated with changes in the petrological and geochemical characteristics of the lavas. For details regarding basalts and sediments, see the "Igneous Petrology" and "Lithostratigraphy" sections (this chapter). Below are brief descriptions of the general features of the sedimentary and primary lava series (see Table 11) and their MST signatures.

To compensate for the reduced core diameter resulting from RCB-coring, the MST GRAPE bulk density was corrected empirically on the basis of the correlation of discrete bulk density samples to GRAPE bulk density (see "Physical Properties" section, "Explanatory Notes" chapter, this volume). For Site 917, we calculated the following equation:

$$y = 0.839x + 0.925,$$

where y = corrected GRAPE density and x = raw GRAPE density, which empirically corrects for the reduced diameter.

Sediment Cover

Mechanical Unit M1 comprises sediments recovered from Cores 152-917A-1R, -4R, and -6R. The uppermost sediments (lithologic Subunit IA, 0–3.0 mbsf) consist of glaciomarine silts. These sediments have high natural gamma (>900 TC) and low magnetic susceptibility (250 cgs). Volcanic conglomerates (lithologic Unit III, 37.7–41.9 mbsf) were recovered immediately above the basalts. These sediments bear similar MST signatures as those of the underlying basalts. For the upper sedimentary package, the most noticeable change is the steady reduction downcore of natural gamma, from 900 TC at the surface to less than 400 TC immediately above the basalts (41.9 mbsf).

Intercalated Sediments

Sediments of lithologic Unit V are intercalated between individual lava flows of the Upper, Middle, and Lower Series. These sediments are expressed in the MST records by high counts of natural gamma and low GRAPE bulk density (Figs. 15 and 36). Note that the magnetic susceptibility of these sediment bands is highly variable, that is, Unit 32A Paleosol shows an increase in magnetic susceptibility and natural gamma, relative to the basalts; Unit 34A Paleosol shows a similar increase in natural gamma, but a decrease in magnetic susceptibility (the unit is flanked by high magnetic susceptibility spikes). These differences in MST signature probably reflect differences not only in the composition of the weathering material, but also the manner in which the weathering was accomplished; for example, the leaching vs. concentration of magnetic minerals (e.g., metallic oxides).

Lavas (Upper Series)

Mechanical Unit M2 comprises the lava flows of the Upper Series (41.9–183.4 mbsf). The Upper Series is composed of 26 olivine-bearing lava flows (picrites, olivine-phyric basalts, aphyric-olivine basalts). The lava flows average 4.2 m in thickness and usually have oxidized and vesicular flow tops. These flow tops are prominent in the MST records and generate positive magnetic susceptibility (presence of magnetic metal oxides) peaks and lower GRAPE bulk densities (enhanced porosity and clay replacement). Figure 36 shows details from Cores 152-917A-20R, -21R, and -22R. The GRAPE bulk density record for Unit 32B shows a clear break at 169 mbsf; below this depth, Unit 32B has an average bulk density of 2.70 g/cm^3; above this depth, the density decreases steadily to 2.50 g/cm^3.

All of the lavas of the Upper Series have relatively low contents of K_2O (average composition of 0.18%), which is reflected in the low natural gamma signal (generally less than 400 TC and stable). Most of the small spikes observed in the natural gamma-ray record result from high background counts generated by the GRAPE source, which saturates the natural gamma detector at the end of each core section run. The lower boundary (at 183.4 mbsf) of the Upper Series is represented by a 67-cm-thick sandstone unit (Unit 34A), which shows a distinct spike in natural gamma (1150 TC) and magnetic susceptibility (2500 cgs) (Fig. 36).

Lavas (Middle Series)

Mechanical Units M3 and M4 constitute the Middle Series basalts and dacites. The Middle Series is composed of 15, in part differentiated, lava units that range in composition from basalts to dacites. Compared to the Upper Series, natural gamma signal increases from ≈350 TC for the Upper Series, to more than 450 TC for the basalts of the Middle Series (Fig. 36), and greater than 650 total counts for the dacites of the Middle Series (Fig. 15, mechanical Unit M4). This can be attributed to the increase in K_2O content (Middle Series average composition of 1.0%, up from 0.18% for the Upper Series; K_2O is still 0.67% for the Middle Series basalts without including the lower dacitic flows) and probably U and Th, as these increase with the degree of differentiation of magma. A slight increase in the magnetic susceptibility (to approximately 500 cgs) coincides with a decrease in MgO, suggesting an increasingly differentiated magma, and hence, a higher content of Fe and Ti oxides. The decrease in density coincides with a decrease in olivine content and in grain size.

Igneous Unit 52 (mechanical Subunit M3b) is a thick aphyric basalt flow that occurs between 271.6 and 326 mbsf and can be distinguished in the MST record by an increase in GRAPE bulk density. Relative to the other lavas of the Middle Series, this unit has higher FeO and a relatively massive (nonvesicular) central region below the flow top.

The base of the Middle Series is represented by dacites and a dacitic tuff unit. This corresponds with a sharp increase in natural gamma (maximum >750 TC) and a decrease in density (2.30 g/cm^3). The dacites have K_2O contents five to six times greater than those of Unit 52 basalts.

Lavas (Lower Series)

The Lower Series is composed of 23 basalt flows, varying from picrites to evolved aphyric basalts, and is broadly divisible into three mechanical units. Mechanical Unit M5 shows considerable small-scale variation relative to the rest of the Lower Series. Mechanical Unit M6 is unique in its high magnetic susceptibility (>2000 cgs) and natural gamma (>500 TC). Mechanical Unit M7 is denoted by very low, consistent counts of natural gamma and a smoother, more cyclic, density curve. The low counts of natural gamma coincide with a reduction in K_2O (average composition of 0.25%) relative to the Middle Series. A number of fault-brecciated zones (540–580 mbsf) in some of the flows coincide with the increases in magnetic susceptibility. The matrix of the fault breccias is composed of clays (which are paramagnetic minerals) and other alteration products (frequently metal oxides).

Pre-basaltic Sediments

The deepest rocks recovered at Site 917 consist of a thin (0.14 m) coarse-grained, quartzose sandstone (lithologic Unit V; 821.06–821.20 mbsf), and low-grade metamorphic clastic sediments of presumed marine origin (lithologic Unit VI, 821.2–EOH). These rocks have been grouped in mechanical Unit M8. An interesting feature of mechanical Unit M8 is its extremely low magnetic susceptibility (<25 cgs). This contrasts strongly with the presumed volcanogenic origin of the sediment ("Lithostratigraphy" section, this chapter). The density and natural gamma records show considerably more variation, with the latter varying from 500 to 1400 TC.

Table 11. Index property data for Site 917.

Core, section, interval (cm)	Depth (mbsf)	Water content W_t (%)	Bulk density (g/cm^3) MB	Grain density (g/cm^3) MC	Dry density (g/cm^3) MB	Porosity (%) MC	Void ratio MC	Basalt pycnometer density (g/cm^3)	Basalt cube density (g/cm^3)
152-917A-									
1R-2, 12–14	0.23	45.87	1.83	2.74	1.25	56.11	1.23		
1R-2, 85–87	0.96	35.88	1.94	2.76	1.43	50.05	0.97		
1R-3, 84–86	2.45	50.21	1.83	2.87	1.22	59.60	1.41		
4R-1, 58–60	29.28	32.69	1.99	2.74	1.50	47.78	0.87		
4R-1, 122–124	29.92	34.07	1.97	2.74	1.47	48.77	0.91		
4R-2, 49–51	30.69	30.74	2.03	2.75	1.55	46.51	0.83		
4R-2, 110–112	31.3	30.33	2.03	2.76	1.56	46.12	0.82		
4R-2, 20–22	31.9	28.78	2.05	2.75	1.59	44.79	0.77		
6R-1, 94–96	42.64								2.61
7R-1, 140–142	48.1								2.66
8R-4, 11–13	60.16								2.81
9R-1, 15–17	64.95								2.70
9R-3, 61–63	68.22								2.79
10R-1, 66–68	74.56								2.69
10R-4, 52–54	78.57								2.73
10R-5, 121–23	80.76								2.55
11R-4, 31–33	87.07								
12R-1, 35–37	92.35								2.65
13R-1, 77–79	101.87								2.70
13R-5, 107–109	108.06								2.78
14R-3, 97–99	113.62								2.87
14R-4, 83–88	114.52								2.78
15R-2, 7–9	120.72								2.15
16R-4, 61–63	133.15								
17R-2, 74–76	138.91								2.64
17R-4, 75–77	141.44								2.79
18R-3, 32–34	148.9							2.78	2.68
18R-4, 94–96	150.93							3.20	2.25
18R-6, 99–101	153.93							2.84	2.78
19R-2, 40–42	157.1								2.63
19R-4, 44–46	160.03							2.78	
20R-1, 21–23	164.71							2.80	2.77
20R-5, 36–38	170.5							2.91	2.87
21R-3, 68–70	177.17								
21R-3, 138–141	177.87							2.65	
23R-1, 68–70	192.58							2.81	2.73
25R-1, 82–84	207.12							2.69	2.62
26R-2, 5–11	212.32								2.27
27R-1, 70–72	216							2.23	
27R-2, 48–50	217.25								
30R-1, 110–12	231							2.68	2.37
30R-3, 38–40	233.03							2.36	2.11
31R-3, 106–108	238.66							2.72	
31R-3, 106–108	238.66							2.69	2.61
32R-3, 134–136	243.9							2.42	2.25
34R-2, 41–43	260.75							2.55	2.41
35R-2, 26–28	265.06							2.76	2.61
36R-6, 34–36	275.56							2.90	2.87
39R-3, 95–97	296.14							2.87	2.82
54R-5, 16–18	389.84							2.85	2.75
55R-4, 11–13	398.05							2.95	2.90
57R-3, 81–83	416.5							2.85	2.83
57R-6, 89–91	420.7							2.76	2.71
57R-7, 20–22	421.49							2.77	2.77
59R-1, 102–104	433.12							2.77	2.70
60R-1, 75–77	437.45							2.75	2.63
61R-2, 54–56	443.16							2.86	2.86
64R-1, 125–127	471.95							2.93	2.90
67R-4, 106–108	504.99							2.83	
69R-2, 90–92	521.2							2.84	
7IR-4, 32–34	542.12							2.79	2.75
72R-1, 100–102	548.3							2.84	2.83
73R-2, 42–44	558.83							2.36	2.23
77R-2, 101–103	588.21								
78R-2, 136–138	597.99							2.58	2.54
79R-2, 91–93	607.35							2.76	2.71
79R-5, 90–92	611.37							2.66	2.56
80R-4, 102–104	619.91							2.79	
81R-3, 97–99	628.25							2.55	2.47
82R-2, 109–111	636.66							2.75	2.67
83R-2, 129–131	646.59							2.84	
84R-2, 95–97	655.95							2.81	2.70
86R-3, 66–68	675.99							2.89	2.83
87R-2, 31–33	683.59							2.90	2.80
89R-2, 6–8	702.35							2.91	2.85
90R-1, 41–43	710.51							2.80	2.71
90R-5, 52–54	715.6							2.85	
92R-4, 5–7	727.44							2.77	2.72
94R-4, 8–10	744.11							2.89	2.83
95R-2, 61–63	751.91							2.86	2.78
96R-1, 123–125	760.63							2.72	2.61
97R-2, 42–44	770.67							2.75	2.68
99R-2, 78–80	790.55							2.84	
100R-1, 104–106	799.04							2.79	2.65
101R-4, 81–83	812.24							2.74	
101R-5, 81–83	812.24							2.75	

Note: Data were calculated according to Method B (MB) or Method C (MC), as defined in "Physical Properties" section, "Explanatory Notes" chapter (this volume).

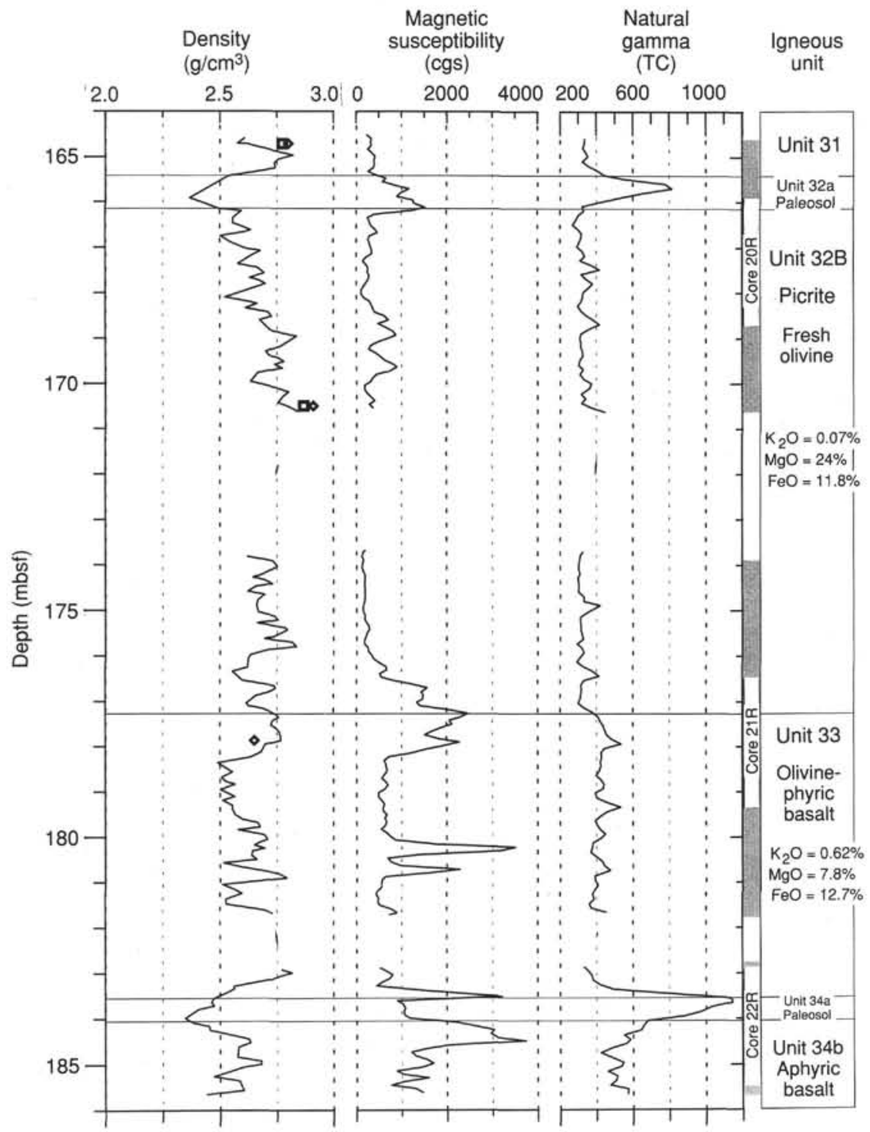

Figure 36. Detailed MST plot for Cores 152-917A-20R, -21R, and -22R (164.5–185.5 mbsf). Wet bulk density = open squares, grain density = open diamonds. See text for interpretation.

Index Properties

Discrete index property samples were tested for all mechanical units except Unit M8. Data are tabulated in Table 11 and illustrated in Figure 15. For the sediments of mechanical Unit M1 (lithologic Units I and II), the grain density is uniform at 2.74 ± 0.01 g/cm^3. This indicates that the dominant particle lithology is consistent and closely resembles the grain density of basalt (≈2.76 ± 0.04 g/cm^3, as discussed below). With depth, the porosity and water content decrease from ≈55 to ≈45% and from ≈45 to ≈30%, respectively, indicative of a normally consolidating sedimentary sequence.

For the basalts, only bulk (60 samples) and grain density (56 samples) were measured (methodology explained in the "Physical Properties" section, "Explanatory Notes" chapter, this volume). All samples were chosen from relatively unaltered flows and, hence, a sampling bias exists toward this material. For all basalts, the average grain density is 2.76 ± 0.04 g/cm^3, with a standard deviation of 0.16 g/cm^3, the average bulk density is 2.67 ± 0.02 g/cm^3, with a standard deviation of 0.19 g/cm^3. This yields an average porosity of 9.6%. Note that for the grain density, the estimate is probably too light, as the pycnometer method of whole-rock grain density is dependent on the interconnection of all porosity in the sample (if so, then we also have underestimated the porosity). However, the similarity in standard deviations for the independently measured parameters led us to conclude that the calculated values are good within the specified error limits.

Velocimetry

Compressional *P*-wave velocity was measured for the indurated sediments, basalts, and metasediments with the Hamilton Frame. Sonic velocity data are tabulated in Table 12 and illustrated in Figure 36. Soft sediments suitable for using the digital sonic velocimeter (DSV) were too badly disturbed by drilling to warrant their testing. In total, four samples were tested from the indurated sediments of Core 152-917A-4R (29.93–31.90 mbsf), 26 samples from the Upper Series, 13 from the Middle Series, 20 from the Lower Series, and four from the metasediments. Most samples from the basalts were chosen from the least-altered portions of individual lava flows. As such, the overall velocity profile is biased toward this unaltered material, with the resulting average and RMS velocities being faster than the true average.

Within the basalts, acoustic velocity fluctuates widely (Fig. 37). This variation may be attributed to differences in mean crystal size and sorting, vesicularity (and the presence of infilling minerals), flow lamination, and glass content. The most important controlling feature

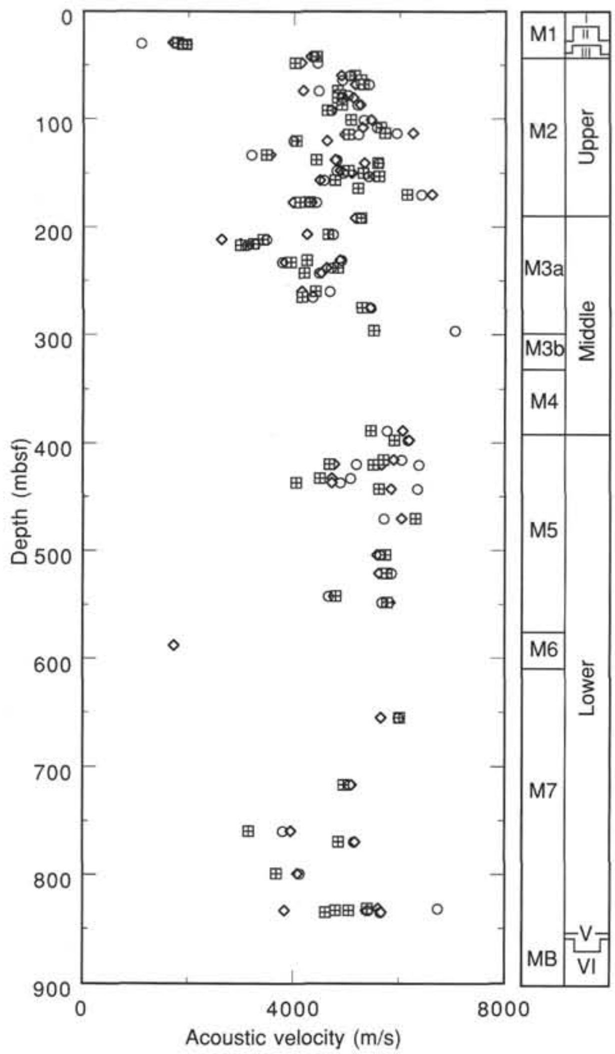

Figure 37. Discrete longitudinal V_z (open diamonds) and transverse V_x (hatched squares) sonic velocity for sediments recovered at Site 917 (V_y = open circles).

seems to be the ratio of phenocrysts to groundmass, with the more fine-grained, homogeneous basalts possessing the faster traveltimes. Acoustic anisotropy for the basalts is slight, with transverse and longitudinal velocities rarely differing by more than 10%.

The comparison of discrete sample to sonic-log acoustic velocities between 192.6 and 548.3 mbsf (Fig. 38) shows that the discrete velocities are consistently faster. This is to be expected because of our sampling bias toward unaltered basalt. The sonic log shows no such bias and averages its measurements over a 0.5-m interval.

Thermal Conductivity

Thermal conductivities were measured for the upper sediments (three samples; lithologic Units I and II), volcanic rocks (68 samples; Upper, Middle, and Lower Series), and metasediments (four samples; lithologic Unit VI) recovered at Site 917. For soft sediments, the full-space thermal conductivity method was employed, while for the volcanic and metasedimentary rocks, the half-space method was used (see "Physical Properties" section, "Explanatory Notes" chapter, this volume). The results are tabulated in Table 13 and illustrated in Figure 39. Also included in Table 13 are the mean thermal conductivities for the principal lithological units. Considerable scatter can be seen in the thermal conductivity data. However, a slight increase in mean thermal conductivity, from 1.54 ± 0.15 W/(m·K) in the upper sediments and lavas of the Upper Series, to 1.71 ± 0.21 W/(m·K) for the lavas of the Middle Series, to 1.78 ± 0.28 W/(m·K) for the lavas of the Lower Series can be discerned. The metasediments are markedly different, yielding a mean thermal conductivity of 2.65 ± 0.17 W/(m·K).

Table 12. *P*-wave velocity measurements for Site 917.

Core, section, interval (cm)	Depth (mbsf)	Calculated velocity V_z (m/s)	V_x (m/s)	V_y (m/s)	Comments
152-917A-					
4R-1, 123–125	29.93	1704	1788	1731	Medium-firm sediment
4R-2, 48–50	30.68	1856	1806	1106	Medium-firm sediment
4R-2, 110–120	31.30	1929	1955	1977	Firm sediment
4R-3, 20–22	31.90	1853	1884	1886	Firm sediment
6R-1, 94–96	42.64	4329	4433	4378	Basalt
7R-1, 140–142	48.10	4142	4023	4440	Basalt
8R-4, 11–13	60.16	4907	5157	5047	Basalt
9R-1, 15–17	64.95	5246	5283	4920	Basalt
9R-3, 61–63	68.22	5170	5323	5426	Basalt
10R-1, 66–68	74.56	4180	4830	4465	Basalt
10R-4, 52–54	78.57	4897	4882	5024	Basalt
10R-5, 121–125	80.76	5132	4828	4920	
11R-4, 31–35	87.07	5258	4918	5209	
12R-1, 35–3	92.35	4712	4639	4712	
13R-1, 77–81	101.87	5466	5088	5323	
13R-5, 107–111	108.06	5299	5654	5565	Flow-banded basalt
14R-3, 97–101	113.62	6257	5726	5938	Flow-banded basalt
14R-4, 83–88	114.52	4965	5035	5218	Flow-banded basalt
15R-2, 7–9	120.72	4621	4044	3985	Very vesicular basalt
16R-4, 61–63	133.15	3549	3480	3187	Friable basalt
17R-2, 74–76	138.91	4787	4416	4810	Small vesicles
17R-4, 75–77	141.44	5340	5591	5602	Homogeneous basalt
18R-3, 32–34	148.90	4884	5035	4810	
18R-4, 94–96	150.93	5094	5314	4931	
18R-6, 99–101	153.93	5530	5612	5416	
19R-2, 40–42	157.10	4492	4787	4573	Calcite–filled vesicles
20R-1, 21–23	164.71	5218	5213		Basalt
20R-5, 36–38	170.50	6615	6145	6416	Basalt
21R-3, 68–70	177.17	3984	4114	4306	Basalt
21R-3, 138–141	177.87	4341	4294	4419	Basalt
23R-1, 68–70	192.58	5170	5283	5267	Basalt
25R-1, 82–84	207.12	4253	4654	4743	Basalt
26R-2, 5–11	212.32	2629	3414	3472	Very vesicular
27R-1, 70–72	216.00	2999	3242	3257	Very vesicular
27R-2, 48–50	217.25	3048	2991	3115	Very vesicular
30R-1, 110–112	231.00	4882	4253	4897	Fine-grained basalt
30R-3, 38–40	233.03	3838	3953	3774	Vesicular
31R-3, 106–108	238.66	4631	4848	4712	Fine-grained basalt
32R-3, 134–136	243.90	4524	4203	4486	Vesicular
34R-2, 41–43	260.75	4157	4415	4683	Minor filled vesicles
35R-2, 26–28	265.06	4162	4167	4353	Devitrified and vesicular
36R-6, 34–36	275.56	5462	5305	5459	
39R-3, 95–97	296.14	5530	5524	7053	Basalt
54R-5, 16–18	389.84	6080	5466	5780	Basalt
55R-4, 11–13	398.05	6196	5913	6167	Basalt
57R-3, 81–83	416.50	5910	5718	6051	Olivine basalt
57R-6, 89–91	420.70	4787	4683	5194	Devitrified
57R-7, 20–22	421.49	5676	5516	6380	Devitrified
59R-1, 102–104	433.12	4735	4502	5084	
60R-1, 75–77	437.45	4735	4064	4887	Vesicular, devitrified
61R-2, 54–56	443.16	5858	5625	6350	Basalt
64R-1, 125–127	471.95	6051	6320	5718	Poor geometry
67R-4, 106–110	504.99	5597	5753	5640	
69R-2, 90–94	521.20	5628	5780	5858	
71R-4, 32–34	542.12	4765	4801	4661	
72R-1, 100–102	548.30	5829	5786	5676	
73R-2, 42–44	558.83				Breccia
77R-2, 101–103	588.21	1743			Poor cube
84R-2, 95–97	655.95	5668	6022	5994	Basalt
92R-4, 5–10	717.44	5102	4961	5071	Fine-grained basalt
96R-1, 123–125	760.63	3967	3166	3808	Zeolites
97R-2, 42–44	770.67	5180	4870	5156	
100R-1, 104–106	799.04	4085	3686	4119	Poor signal
104R-1, 128–230	832.78	5615	5416	6739	Metasediment
104R-2, 50–52	833.50	3842	5059		Metasediment
104R-2, 98–100	833.98	5390	4810	5423	Metasediment
104R-3, 95–97	835.06	5676	4610	5647	Metasediment

Note: Longitudinal velocity V_z is perpendicular to core axis, transverse velocity V_x is parallel to bedding strike, transverse velocity V_y is perpendicular to bedding strike (see "Physical Properties" section, "Explanatory Notes" chapter, this volume).

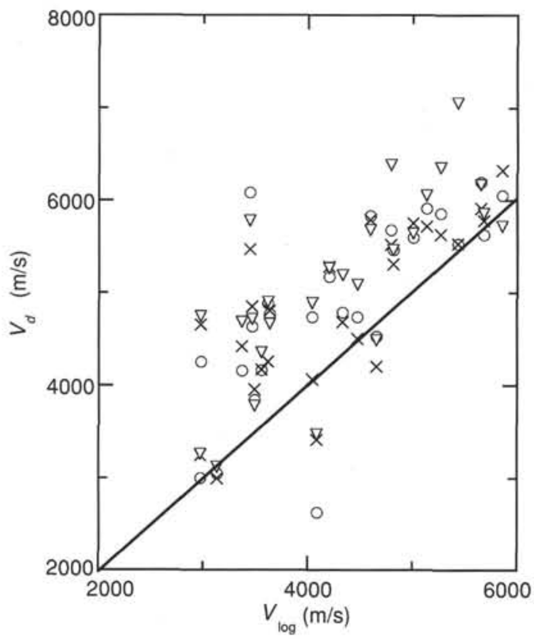

Figure 38. Crossplot of sonic log and discrete sample acoustic velocity for volcanic rocks of Site 917. Note the consistently higher velocities for the discrete samples. V_z = open circles; V_x = crosses; V_y = inverted triangles.

Variability in the thermal conductivity is highest for the lavas of the Middle and Lower Series, with standard deviations of ±0.21 and ±0.28 W/(m·K), respectively. This variability reflects differences in composition, alteration, and vesicularity. Figure 40 illustrates the relationship between alteration and vesicularity and the thermal conductivity of the basalts. One can readily see that the thermal conductivity of basalts has been reduced by increasing degrees of alteration (glass devitrification; increasing clay content) and by vesiculation (physical discontinuities).

The high thermal conductivities (mean = 2.65 ± 0.17 W/[m·K]) of the metasediments of lithologic Unit VI reflect their fine-grained, crystalline nature. An inverse relationship between the thermal conductivity and magnetic susceptibility can be observed within metasediments (Figs. 15 and 40).

For the basalts, magnetic susceptibility and natural gamma highs (and thermal conductivity lows) tend to be associated with increasing alteration. For the metasediments, extremely low magnetic susceptibilities are associated with high thermal conductivity and natural gamma.

Summary

Physical properties data were collected for sediments, lavas, and metasediments recovered at Site 917. MST data (GRAPE bulk density, magnetic susceptibility, and natural gamma) correlate well with trends in the geochemistry (see "Igneous Petrology" section, this chapter) and demonstrate the validity of the MST for defining lithologic and compositional units in volcanic rocks. Differences in flow morphology (e.g., vesicularity) may be interpreted from the GRAPE density records (e.g., the rate of change of density). Variations in bulk chemistry may be qualitatively (and perhaps crudely quantitatively) evaluated using the magnetic susceptibility and natural gamma-ray data.

DOWNHOLE MEASUREMENTS

In Hole 917A, drilling was terminated at a total depth of 874.9 mbsf and was followed by release of the drill bit at the bottom of the hole. After cleaning the hole in preparation for logging, the drill pipe was raised to 124.5 mbsf and the first downhole sensor was rigged up. Given the main scientific priorities of Leg 152, one of the targets of Hole 917A was to characterize tectonic features of the sedimentary unit located beneath the basaltic SDRS at the bottom of the hole. Because of this clear scientific priority, the first run consisted of the formation microscanner (FMS). The tool was run down the hole, where it encountered a bridge at 664.0 mbsf. After several unsuccessful attempts to cross the bridge, the pads of the FMS were opened and logging was started upward from 664.0 mbsf. No resistivity data were recorded at the beginning of the run because gain was too low, compared to the expected electrical properties of the formations in the borehole wall. Following increase of gain, the recording of data started efficiently above 595.0 mbsf. The 430-m interval from 595.0 to 165.0 mbsf was successfully logged by the FMS. A second pass or, at least, a short repeat with the FMS was not conducted because of the need to pull out of the hole owing to an approaching iceberg.

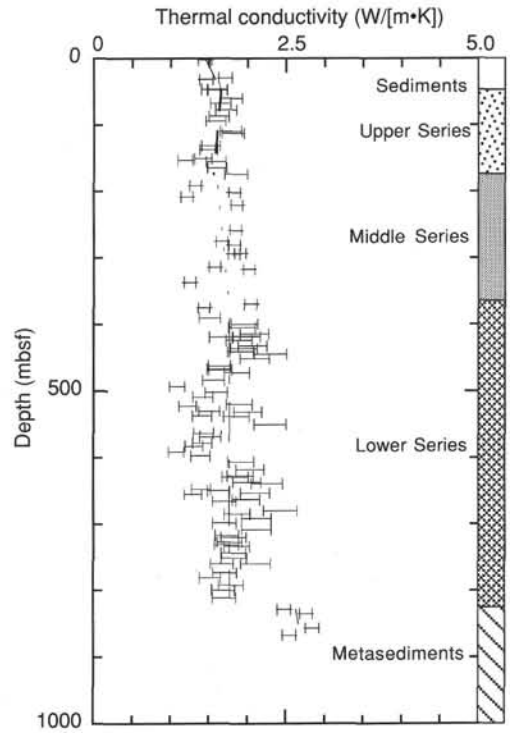

Figure 39. Thermal conductivity as a function of depth (mbsf) for cores recovered at Site 917.

A combination of geophysical sensors was rigged up for the second run. It consisted, from top to bottom, of natural gamma (NGT), velocity (SDT), density (HLDT), resistivity (DIT) and temperature (TLT) sensors. The tool string was logged downhole for temperature measurements and hit a bridge at 586.0 mbsf. After several attempts to cross this bridge, the tool was calibrated on an upward run above this obstruction. The tool was run down the hole again, but encountered another bridge at 573.0 mbsf. Logging started from this depth up to 181.0 mbsf. Given the length of this tool assembly (31.4 m), the interval of 360 m from 535.0 to 181.0 mbsf was successfully logged.

After these two logs, we decided to try to lower the drill pipe into the hole to penetrate its lower parts. Unfortunately, during this operation, part of the borehole collapsed and the drill pipe encountered and became jammed by a mixture of dropstones and volcanic sand. Consequently, logging was terminated at this site.

In the interval logged, the borehole is slightly elliptical, with an average diameter of 11 in., except for the section from 320.0 to 360.0 mbsf, where the hole was caved and was about 13 in. in diameter. Deviation of the borehole axis is about 6° to the west. Except at the

Table 13. Summary of thermal conductivity measurements for Site 917.

Core, section, interval (cm)	Piece	Method full-/half-space	Depth (mbsf)	Thermal conductivity (W/[m•K])	SD
152-917A-					
1R-3, 60		F	2.21	1.443	0.00012
4R-1, 80		F	29.50	1.706	0.00028
4R-3, 25		F	31.95	1.456	0.00120
7R-1, 41–47	10	H	46.73	1.517	0.00079
7R-1, 136–145	22	H	47.10	1.603	0.00140
8R-4, 10–20	2	H	60.15	1.785	0.00240
9R-3, 40–52	5	H	68.01	1.647	0.00970
11R-4, 35–45	1C	H	87.11	1.628	0.00097
12R-2, 115–125	8	H	94.62	1.585	0.00110
16R-3, 58–68	3A	H	131.69	1.518	0.00086
17R-1, 30–40	2D	H	137.51	1.489	0.00091
18R-4, 100–114	7B	H	150.98	1.418	0.00078
18R-6, 9–21	2	H	153.03	1.185	0.00510
20R-1, 48–54	4	H	164.98	1.596	0.00079
21R-1, 70–77	8B	H	174.30	1.844	0.00130
23R-1, 27–36	4	H	192.17	1.323	0.00089
24R-1, 111–120	13	H	202.11	1.823	0.00063
28R-1, 12–139	10	H	221.55	1.861	0.00086
37R-3, 9–20	2	H	281.03	1.823	0.00110
38R-5, 125–139	5	H	293.31	1.904	0.00048
39R-2, 90–100	1F	H	294.74	1.816	0.00078
42R-2, 125–135	2D	H	314.32	1.571	0.00100
53R-1, 89–100	2	H	375.4	1.434	0.00110
54R-5, 95–104	1B	H	390.63	1.509	0.00100
55R-5, 65–69	9A	H	399.97	1.959	0.00085
56R-2, 72–80	1F	H	405.59	1.925	0.00085
57R-4, 89–97	5	H	418.45	1.991	0.00100
57R-5, 129–138	8C	H	419.43	1.651	0.00097
58R-2, 98–113	2B	H	424.54	1.889	0.00088
59R-1, 50–62	2E	H	432.60	2.064	0.00100
63R-1, 9–18	2A	H	436.79	1.952	0.00110
63R-2, 42–56	1A	H	462.69	1.630	0.00081
69R-2, 19–27	6	H	520.49	1.890	0.00110
69R-4, 0–12	4	H	523.03	1.220	0.00140
70R-2, 135–145	11	H	530.60	1.501	0.00140
71R-1, 0–9	1A	H	537.70	1.402	0.00820
71R-1, 80–88	1G	H	538.50	1.851	0.00130
72R-3, 62–74	2B	H	550.70	2.294	0.00110
74R-2, 42–52	5	H	568.52	1.514	0.00120
75R-2, 54–65	4A	H	578.34	1.413	0.00100
77R-5, 0–12	1	H	591.70	1.074	0.00190
78R-2, 120–131	4A	H	597.83	1.386	0.00074
79R-1, 112–122	8B	H	606.32	1.914	0.00086
80R-3, 98–105	10	H	618.58	2.031	0.00120
82R-3, 70–80	1B	H	637.50	1.995	0.00150
82R-5, 14–21	1A	H	639.74	2.256	0.00086
83R-3, 61–70	5	H	647.36	1.398	0.00120
83R-5, 80–88	3	H	650.19	1.622	0.00094
83R-8, 30–38	2A	H	653.71	2.101	0.00100
84R-2, 54–65	3A	H	655.54	1.293	0.00080
85R-1, 7–15	2	H	663.27	1.979	0.00120
85R-2, 136–147	12	H	665.99	1.701	0.00100
86R-6, 55–70	1	H	680.05	2.426	0.00093
87R-3, 80–91	1B	H	685.50	1.863	0.00140
88R-1, 40–50	5	H	692.20	2.118	0.00110
88R-6, 0–8	1A	H	698.42	1.697	0.00110
89R-6, 55–58	1G	H	708.30	2.120	0.00098
90R-6, 70–77	3A	H	716.99	1.731	0.00150
91R-1, 27–36	ic	H	720.27	1.821	0.00090
92R-1, 57–67	20	H	727.82	1.766	0.00072
92R-4, 43–53	3	H	731.46	1.726	0.00074
93R-1, 106–117	3A	H	733.83	1.858	0.00920
93R-3, 86–94	1E	H	744.56	1.816	0.02700
94R-4, 53–66	2	H	751.94	1.829	0.00710
95R-2, 64–74	1E	H	760.55	2.106	0.00140
96R-1, 115–128	10A	H	760.55	1.668	0.00290
97R-6, 62–70	6	H	773.46	1.708	0.01000
98R-2, 125–132	5	H	781.31	1.516	0.00850
99R-4, 20–30	1A	H	792.62	1.788	0.00910
100R-2, 83–87	1F	H	800.03	1.685	0.00700
101R-4, 13–21	1B	H	811.56	1.696	0.00760
103R-2, 91–99	4A	H	829.18	2.475	0.01000
104R-3, 123–131	2A	H	835.34	2.762	0.00850
108R-2, 33–44	3B	H	857.50	2.838	0.00790
110R-2, 64–74	10	H	867.44	2.543	0.00730

Unit/Series	Mean	Std. dev.	n
Sediment (lithologic Units I and II)	1.54	0.15	3
Upper Series volcanics	1.54	0.15	11
Middle Series volcanics	1.71	0.21	9
Lower Series volcanics	1.78	0.28	48
Metasediments (lithologic Unit VI)	2.65	0.17	4
Total:			75

Notes: SD = standard drifting (see "Physical Properties" section, "Explanatory Notes" chapter, this volume). Mean thermal conductivities and standard deviations are given for each principal lithologic/petrologic unit/series. Std. dev. = standard deviation, and n = number.

very bottom, the borehole's shape and conditions were favorable for downhole experiments. As a consequence, the data recorded in Hole 917A are of excellent quality. The sampling distance of 2.52 mm for FMS images is the smallest of any presently available downhole sensor. The other records presented here have been sampled with a 0.152-m digitization interval, except for the density data, which have been sampled in high-resolution mode at an interval of 0.0254 m. A detailed description of each sensor and measurement principles are provided in the "Explanatory Notes" chapter (this volume). A summary of the log is given in Figures 16 and 41.

Run 1: FMS Electrical Images—Natural Gamma Rays

The formation microscanner (FMS) produces high-resolution borehole images and thus allows for visual characterization of the structures located in the near vicinity of the borehole wall (Ekstrom et al., 1986). The natural gamma sonde was also included for depth correlation purposes.

The data were acquired by a MAXIS 500 unit, which also produced a real time display of FMS images of the borehole wall at 1/200 scale. This scale is not detailed enough to see or to quantify fracturing or dip of the basaltic flows, but the main features, such as the boundaries between flows and scoriaceous horizons within each flow, can be seen clearly. Further shore-based processing of the raw FMS data into electrical images at 1/10 scale will be conducted, which will allow for detailed observation of the tectonic features within and in between basaltic flows.

The size and shape of the borehole as well as deviation from vertical, and drift azimuth with respect to north of the borehole can be described from data recorded by the calipers and by the general purpose inclination tool. In the logged section, Hole 917A tends to drift to the southwest in the upper part, with trends more to the northwest in the lower part. Deviation of the borehole axis from vertical is approximately 5°, with values between 6° and 7° in the upper part to 350.0 mbsf, decreasing to 4° until 480.0 mbsf and increasing to 5° at the bottom of the logged section (595.0 mbsf).

The hole size measured by the FMS shows an average diameter of 11 inches. Differences between the two perpendicular calipers (C1 and C2) of the FMS pads allow us to monitor the elliptical shape of the borehole wall. Throughout the hole, the west-east oriented caliper always gave a smaller diameter than north-south one (Fig. 42). As a consequence, elliptical elongation of the borehole is close to a north-northeast/south-southwest axis. The presence of an elliptical borehole shape is generally interpreted as breakouts (Bell and Gough, 1979; Morin et al., 1990), with the long axis of the borehole pointing toward the minimum horizontal stress direction. Caliper differences recorded within Hole 917A reinforce this correlation. The C1–C2 difference is of the order of 1 in. between 165.0 and 340.0 mbsf, and after a 90° rotation of the tool at this latter depth, of 0.5 in. until 595.0 mbsf (Fig. 42).

In the upper part of basaltic SDRS, resistivity values are low (less than 10 Ωm until 280.0 mbsf) as a result of the thin nature of the flows and, perhaps, fractures. In the lower part, the basaltic units are thicker and the values of resistivity are higher, except in the scoriaceous part of basaltic flows (up to 100 Ωm from 380.0 to 535.0 mbsf). Therefore, a direct correlation exists between the C1–C2 difference and the rheology of the basalts: massive and thick sequences are less deformed than thin and fractured ones, in which concentration of breakouts implies an important elongation of the hole.

The two caliper measurements obtained with the FMS tool show a bimodal distribution of enlargements, with azimuthal orientation of elongation at about N015° (Fig. 42). This constrains the maximum horizontal stress in the basaltic SDRS of Hole 917A to N105° significantly, in accordance with the direction of motion of the North American Plate in this area (Srivastava and Tapscott, 1986).

In conclusion, the FMS data recorded in the basaltic SDRS of Hole 917A and processed onshore should help to provide constraints on the lithostratigraphy, structure, and stress environment encountered while drilling.

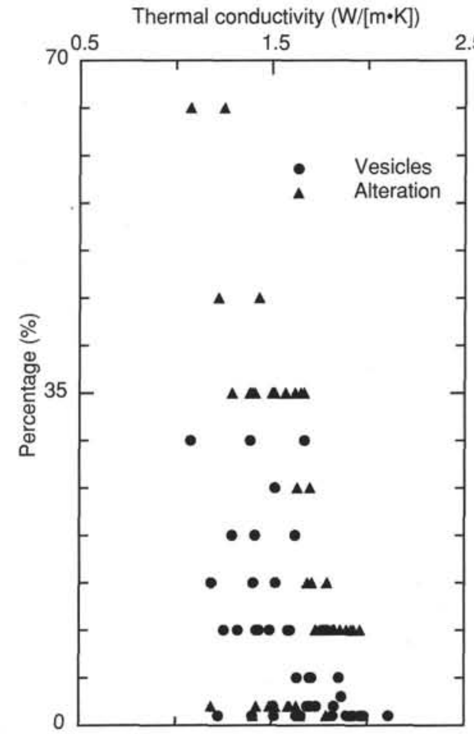

Figure 40. Crossplot of thermal conductivity vs. degree of alteration and vesicularity. Percentages were estimated for each hand specimen tested.

Run 2: Geophysical Combination

The geophysical combination consisted, from the bottom to the top, of the temperature sonde (TLT), the induction resistivity (DIT) sonde, the lithodensity (HLDT) sonde, the acoustic velocity array (SDT) sonde, and the natural gamma (NGT) sonde.

Damaged by attempts to cross bridges, the internal acquisition system of the temperature logging tool, which is only mechanically connected to the Schlumberger string, provided a discontinuous record of data, which does not allow one to establish a profile of temperature vs. depth. However, temperature at seafloor level (5.2°C) and at total depth (20.3°C) were recorded. As these measurements were recorded during the second run, these data may be unsatisfactory because of the thermal disequilibrium of the hole at this time.

The electrical resistivities determined by the deep (IDPH) and medium induction (IMPH) tools are essentially the same. The spherically focused electric tool (SFLU) shows a similar trend, except in the most resistive formations, where the shallow measurements are lower than the deep one. This effect is a manifestation of conductive fluids in the borehole, but its consequence for log interpretation is negligible. In particular, the deep resistivity induction tool measured the true formation resistivities in Hole 917A. The formation resistivity measured in Hole 917A shows a large range as a function of depth (Fig. 41). In the upper part of the hole (from 181.0 mbsf), the average resistivity is low (10 Ωm). A resistivity increase occurred at 270.0 mbsf and measurements peaked at 50 Ωm, but dropped back to 10 Ωm in the interval from 320.0 to 350.0 mbsf. While the resistivity shows a smooth trend down to 320.0 mbsf, below this point, it shows sharp fluctuations, oscillating from 10 to 80 Ωm.

The density data correlate well with the resistivity data and show the same trend. Average density is 2.2 g/cm^3 from the top of the logging interval to 260.0 mbsf, 2.8 g/cm^3 from 260.0 to 320.0 mbsf,

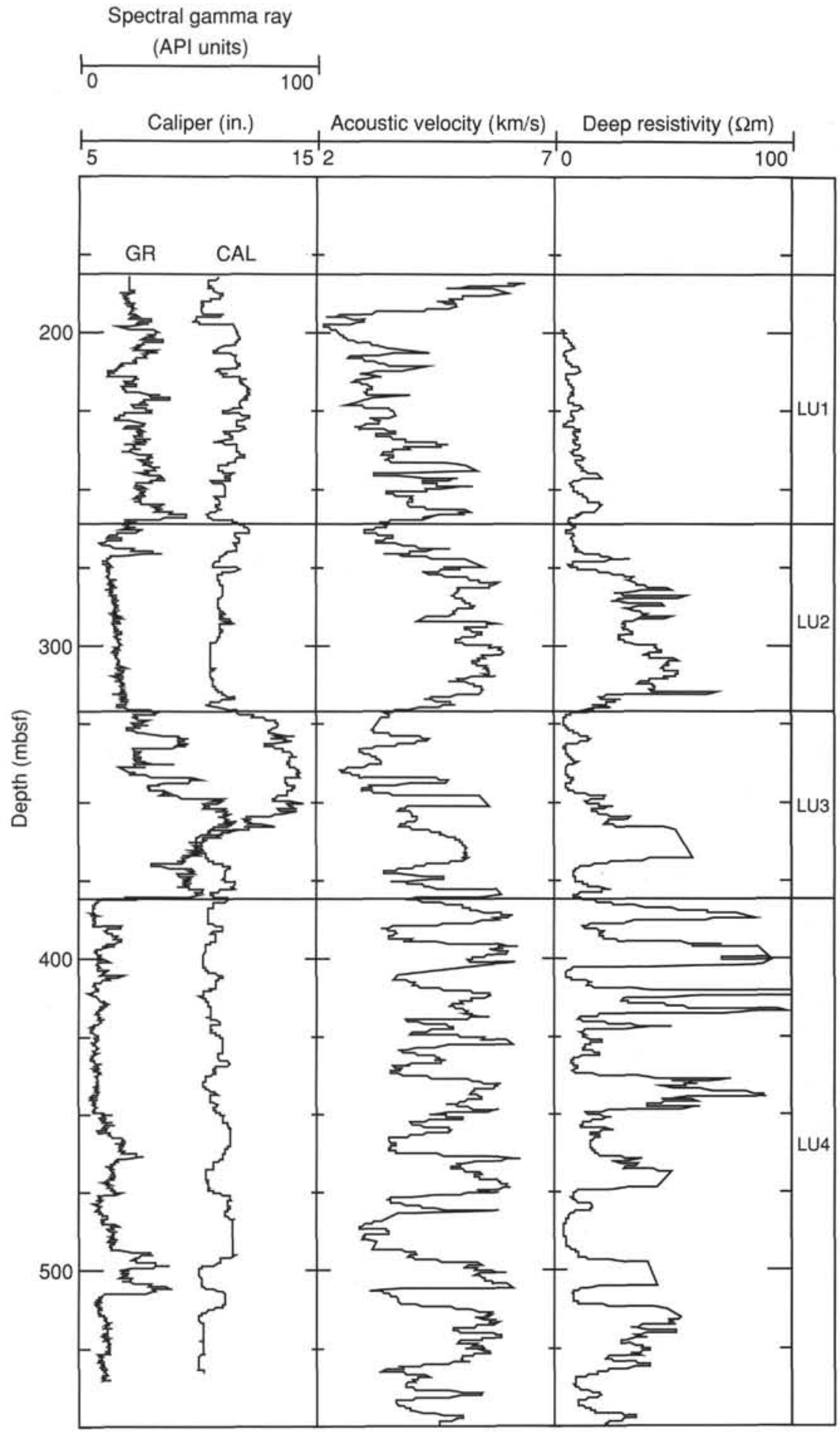

Figure 41. Summary log from NGT (gamma-ray), SDT (acoustic), and DIT (resistivity) tools.

2.2 g/cm^3 from 320.0 to 380.0 mbsf, and 2.6 g/cm^3 for the remainder of the measured interval. Density readings have to be corrected for the caliper effect, especially in the section from 320.0 to 360.0 mbsf, where the enlargement is important.

During acquisition of the sonic data, the noise level was high, which interfered with the signal from the formation. This noise was primarily a result of the absence of adequate centralization of the sonic tool, because it was used in combination with other geophysical sensors. This lack of centralization resulted in asymmetrical arrivals at the level of the receivers and in "road noise" caused by occasional direct contact between the tool and the formation. Consequently, the final velocity profile was computed to smooth the induced background noise. Acoustic data, however, are distinguished by extreme variability. An attempt to provide an absolute value to a given interval will depend on the averaging procedure.

The velocity curve as a function of depth shows a similar trend to the resistivity curves and can be also split into three major intervals (high resistivity corresponding to high velocity): an interval from 181.0 to 260.0 mbsf at 3.5 km/s; an interval from 260.0 to 320.0 mbsf at 5 km/s; an interval from 320.0 mbsf to bottom at 4.5 km/s having tremendous peaks at 6 km/s, and a small, slow velocity interval (3.5 km/s) between 320.0 and 350.0 mbsf.

Caliper information is useful for evaluating hole conditions. In cross section the hole shape is regular at a diameter of about 11 in. An important enlargement is seen between 320.0 and 360.0 mbsf that will cause underestimation of the velocity, resistivity, and density data over that interval.

Natural Gamma-ray Spectrometry

Measurement of natural gamma-ray is included in each tool combination for correlating depth among different logs. The two records are of good quality and well correlated, with a generally low stable concentration of uranium throughout the analyzed section. The main variations are shown by K_2O and thorium, which are positively correlated (Fig. 16). Gamma-ray values are intermediate from the top of the measured interval (181.0 mbsf) to 260.0 mbsf (30 API), decrease from 260.0 to 320.0 mbsf (20 API), peak at 60 API from 320.0 to 380.0 mbsf, and decrease to a low rate (10 API) below 380.0 mbsf until the bottom of the measured interval (535.0 mbsf).

Preliminary Stratigraphic Results from Downhole Measurements and Log-core Integration

Synthetic Seismogram

Because of the absence of a centralizer on the sonic tool (SDT), the acoustic measurements sometimes are obliterated by background noise and must be smoothed and cleaned of the main parasitic effects. After this processing, the density and sonic traveltime data logged in Hole 917A can be used to generate a reflection coefficient series (Fig. 43). Convolved with an appropriate wavelet (see Fig. 2, "Pre-Cruise Site Survey" chapter, this volume) provided from data acquired during the *Magnus Heinasson* site survey, this series resulted in the synthetic seismogram shown in Figure 43. The synthetic seismogram is compared with the seismic line of the site survey. Two reflectors clearly are correlated at 216 and 245 ms and correspond to the limits of a dacitic layer marked by hyaloclastic breccias.

The main synthetic reflectors (Fig. 43) correlate well with the major changes in lithology observed in the cores and allow us to define the limits of the main logging units. The highest amplitude reflector is located at 145 ms two-way traveltime from the seafloor (about 190 mbsf) and corresponds to the occurrence of tuff and hyaloclastite (igneous Units 35 and 36), which marks the transition between olivine basalt (Upper Series) and more differentiated basalt (Middle Series). Among the other significant reflectors, we can see the following correlations:

1. At 180 ms (about 275 mbsf), the reflector corresponds to an oxidized basaltic layer (Unit 51) that marks the transition between aphyric basalts and aphyric olivine basalt.
2. At 215 ms (about 340 mbsf), the reflector correlates with the top of a zone of dacite (Unit 54) and at 240 ms (about 380 mbsf), with the bottom of the same zone (Unit 56).

The slight differences between these time and depth values (Fig. 38) and the values obtained from the core observation (see "Igneous Petrology" section, this chapter) can probably be attributed to the hole conditions and the noncentralized acoustic measurements (unreliable acoustic data have been forwarded to the entire section through the integrating process of the convolution). At any rate, the synthetic seismogram results correlate well with other logging parameters, and the location of the main reflectors fits with the boundaries of the principal igneous units observed in the cores.

Logging Units

Four logging units were identified in Hole 917A on the basis of log response. These logging units should not be confused with the lithologic units defined earlier (see "Igneous Petrology" section, this chapter). The boundaries between adjacent logging units were placed at a significant inflection point that resulted from simultaneous variations on at least several of the logs illustrated in Figures 16, 41, and 43. These logging units display consistent log response or distinct overall trends. In particular, in this case, gamma-ray and synthetic seismogram data were used to define the main logging units, which were later adjusted with the help of the other logging parameters.

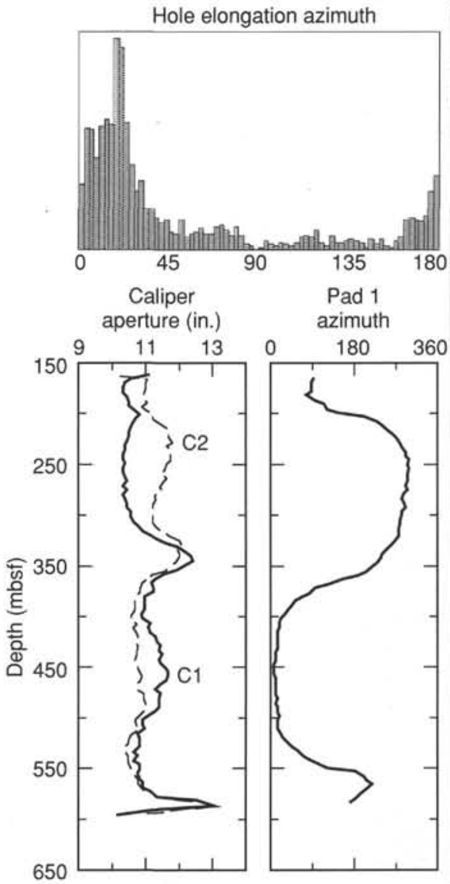

Figure 42. Example illustrating the constant hole elongation direction, as observed with FMS calipers in the basalts. The tool rotated 90° at 350.0 mbsf. The largest hole diameter remains oriented near the north-south axis.

Logging Unit 1 (180.0–260.0 mbsf)

The top of logging Unit 1 was established from the gamma-ray profile acquired during the FMS run (Fig. 44), which shows an increase from 10 to 30 API at 180.0 mbsf. The record during the geophysical assembly run was interrupted just below this depth. The synthetic seismogram, however, shows a major reflector at 190.0 mbsf, which can correspond to this unit. Logging Unit 1 is characterized by intermediate gamma-ray values (30 API), produced by the high thorium content (3 ppm), with low K_2O content at 1%. Acoustic velocity increases slightly from 2.5 to 3.5 km/s in this unit and covaries with resistivity data (from 5 to 10 Ωm). Density values are about 2.2 g/cm^3.

Logging Unit 1 corresponds to the succession of aphyric basaltic lava flows (Middle Series: Units 35 to 51, see "Igneous Petrology" section, this chapter), which is overlain by a picritic olivine basalt. The medium to high gamma counts, and particularly thorium behavior, are related to the differentiated nature of these basaltic flows.

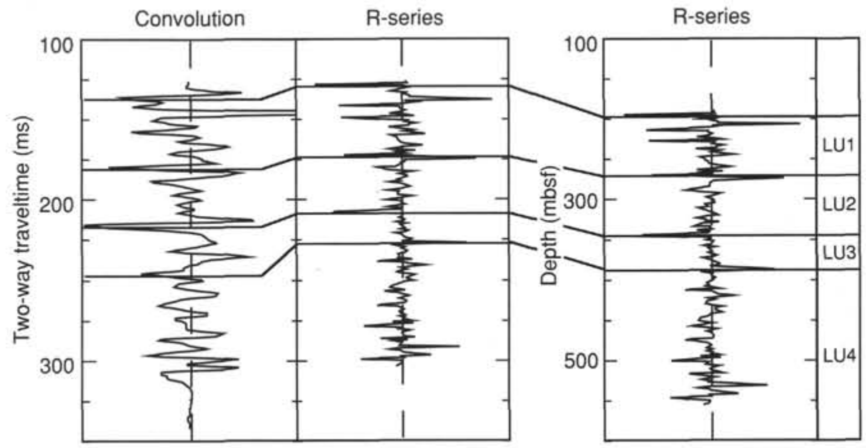

Figure 43. Synthetic seismogram from logging data for Hole 917A.

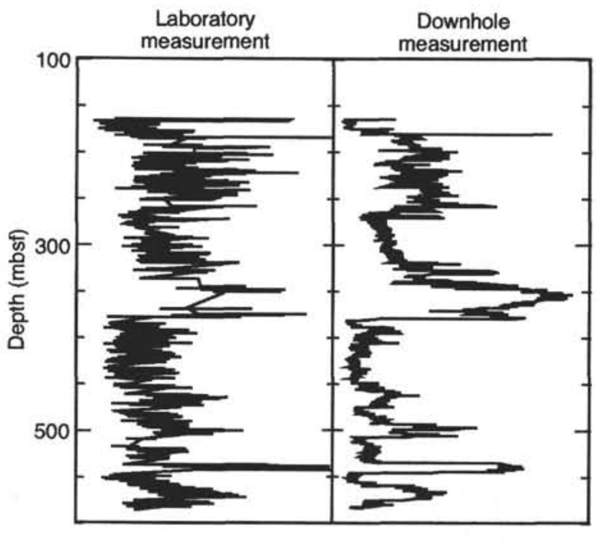

Figure 44. Summary log for natural gamma rays from core measurements and from NGT-FMS.

Logging Unit 2 (260.0–320.0 mbsf)

The top of logging Unit 2 is delimited both by a decrease of gamma ray values from 25 to less than 20 API and by a major reflector of the synthetic seismogram. The transition is especially well marked by a sharp decrease of thorium content from 3 to less than 1 ppm. Logging Unit 2 is characterized by a constantly increasing profile of gamma rays with increasing depth, which could be interpreted as a differentiation trend in the thick lava flow, and by an abrupt increase in density (2.8 g/cm^3), velocity (5 km/s), and resistivity (50 Ωm).

Logging Unit 2 corresponds to a massive and single flow of aphyric olivine basalt (igneous Unit 52). The continuity of lithology in this depth interval readily explains the noticeable stability on the logging parameters.

Logging Unit 3 (320.0–380.0 mbsf)

The upper limit of logging Unit 3 is defined by both an abrupt increase in gamma-ray values from 20 to 60 API and by a major reflector on the synthetic seismogram. Spectroscopy measurements of gamma rays exhibit high contents of K_2O (3.5 wt%) and thorium (3 ppm). Density is low at about 2.2 g/cm^3. Velocity and resistivity correlate well together and show a peaky profile. Velocity changes from 3.5 to 5.0 km/s and resistivity from 10 to 60 Ωm. This variability of both acoustic and resistive parameters is the major feature of the lower part of the logged interval.

Logging Unit 3 corresponds to the occurrence of dacite (Units 54–56) within the basalt flows. The chemical signature of this differentiated formation is well marked by sharp increases in K_2O and thorium, so that gamma-ray spectrometry is important for defining this logging unit. Geophysical parameters do not show important differences between Unit 3 and the underlying unit.

Logging Unit 4 (380.0 mbsf–535.0 mbsf)

The upper limit of logging Unit 4 is defined both from a major reflector seen in the synthetic seismogram and from a sharp decrease in the gamma-ray profile from 60 to 20 API. The average density is about 2.8 g/cm^3. Acoustic and resistivity data are still well correlated and show a fluctuating profile as in logging Unit 3. However, higher peak amplitudes are recorded: velocity varies from 3.5 to 6.0 km/s and resistivity varies from 10 to 80 Ωm. Gamma-ray spectrometry shows low and smooth profiles, except for noticeable peaks of both K_2O and thorium at 460.0 and 500.0 mbsf and at the bottom of the profile (535.0 mbsf).

Logging Unit 4 correlates with the recurrence of less differentiated basalt flows. The succession of the flows is well recorded by the velocity and resistivity parameters: sharp peaks correspond to the lower massive part of a single flow sandwiched between lower-resistivity, scoriaceous, upper and lower horizons. These scoriaceous horizons often contain an increased proportion of vesicles. The structure of vesicular basalt is less coherent and less continuous than nonvesicular basalt. These two characteristics explain the low acoustic velocity recorded in the scoriaceous level. Low electrical resistivity at the same level results from the alteration minerals within the vesicles, which generally contain clays. Gamma-ray spectroscopy profiles are generally low and flat in logging Unit 4, except for abrupt K_2O and thorium peaks. These patterns can be interpreted as the occurrence of more differentiated flows or by local contamination of the flows by thorium introduced along faults.

Comparison with Laboratory Measurements in Cores

The reliability of physical measurements taken deeply in a hole may be questioned, because the pressure and temperature conditions can be very difficult to assess and sensors are far from the acquisition system. The reliability of the data can be tested by comparison of logging data with the measurements performed directly on recovered cores (see "Physical Properties" section, this chapter). A step-by-step correlation shows a good fit between the two sets of data. This observation is illustrated by gamma-ray curves in Figure 44, where good depth correlation can be observed between the two sets of data

(±1 m). The laboratory measurements are noisy compared to logging data, because gamma-ray intensity there was estimated from a given section and, generally, the diameters of cores are always smaller and variable. As a consequence, the gamma-ray count has been influenced by a changing proportion of air in the section. Further shore-based processing can correct this effect. Other differences are related to the large section surveyed during downhole measurement of gamma-ray intensity. As a consequence, logging data are less sensitive to minor changes in lithology.

Conclusions

A suite of downhole logs was successfully recorded at Site 917, resulting in the identification of four distinct logging units. These logging units correlate well with major lithologic changes defined from core descriptions.

At Hole 917A, the recovery of volcanic rocks was remarkably high, and hole conditions allowed us to record excellent logging data. As a consequence, Hole 917A provides a major opportunity to calibrate accurately variations of logging parameters with observations from the cores. Results of such a study might be helpful for interpreting logs during any future cruises devoted to volcanic passive margins.

Ms 152IR-109

NOTE: For all sites drilled, core-description forms ("barrel sheets") can be found in Section 4, beginning on page 303. Forms containing smear-slide data can be found in Section 5, beginning on page 925. Thin-section data are given in Section 6, beginning on page 947. Conventional log, FMS, Dipmeter, Sonic waveforms, GRAPE, Index property, MAGSUS and Natural gamma-ray data are presented on CD-ROM (back pocket).

Shore-based Log Processing for Hole 917A

Bottom felt: 519 mbrf (used for depth shift to seafloor)
Total penetration: 874.9 mbsf
Total core recovered: 454.88 m (52%)

Logging Runs

Logging String #1: FMS/GPIT/NGT
Logging String #2: DIT/SDT/HLDT/NGT

Wireline heave compensator was used to counter ship's heave.

Drill pipe/Bottom-hole Assembly/ Casing

Neither drill string reached the bottom of the pipe.

Processing

Depth shift: All logs have been interactively depth-shifted with reference to the NGT from the FMS/GPIT/NGT run and to the seafloor (–519 m). A list of the amount of differential depth shifts applied at this hole is available upon request.

Gamma-ray processing: NGT data were processed to correct for borehole size and type of drilling fluid.

Acoustic data processing: The sonic logs have been processed to eliminate some of the noise and cycle skipping experienced during recording.

Quality Control

Hole diameter was recorded by the hydraulic caliper on the HLDT tool (CALI) and the caliper on the FMS string (C1 and C2).

The density data are locally affected by the irregular hole size: invalid spikes were detected at 199, 233, 324, 351, 377, and 556.5 mbsf.

The resistivity logs show invalid data at 321–322 mbsf.

Invalid gamma-ray readings were detected at 20, 86, and 97 mbsf (DIT/SDT/NGT string) and at 105 mbsf (DIT/SDT/HLDT/NGT string).

NOTE: Details of standard shore-based processing procedures can be found in the "Explanatory Notes" chapter (this volume). For further information about the logs, please contact:

Cristina Broglia or Elizabeth PratsonPhone: (914) 365-8343Phone: (914) 365-8313
Fax: 914-365-3182Fax: 914-365-3182
E-mail: chris@ldeo.columbia.eduE-mail: beth@ldeo.columbia.edu

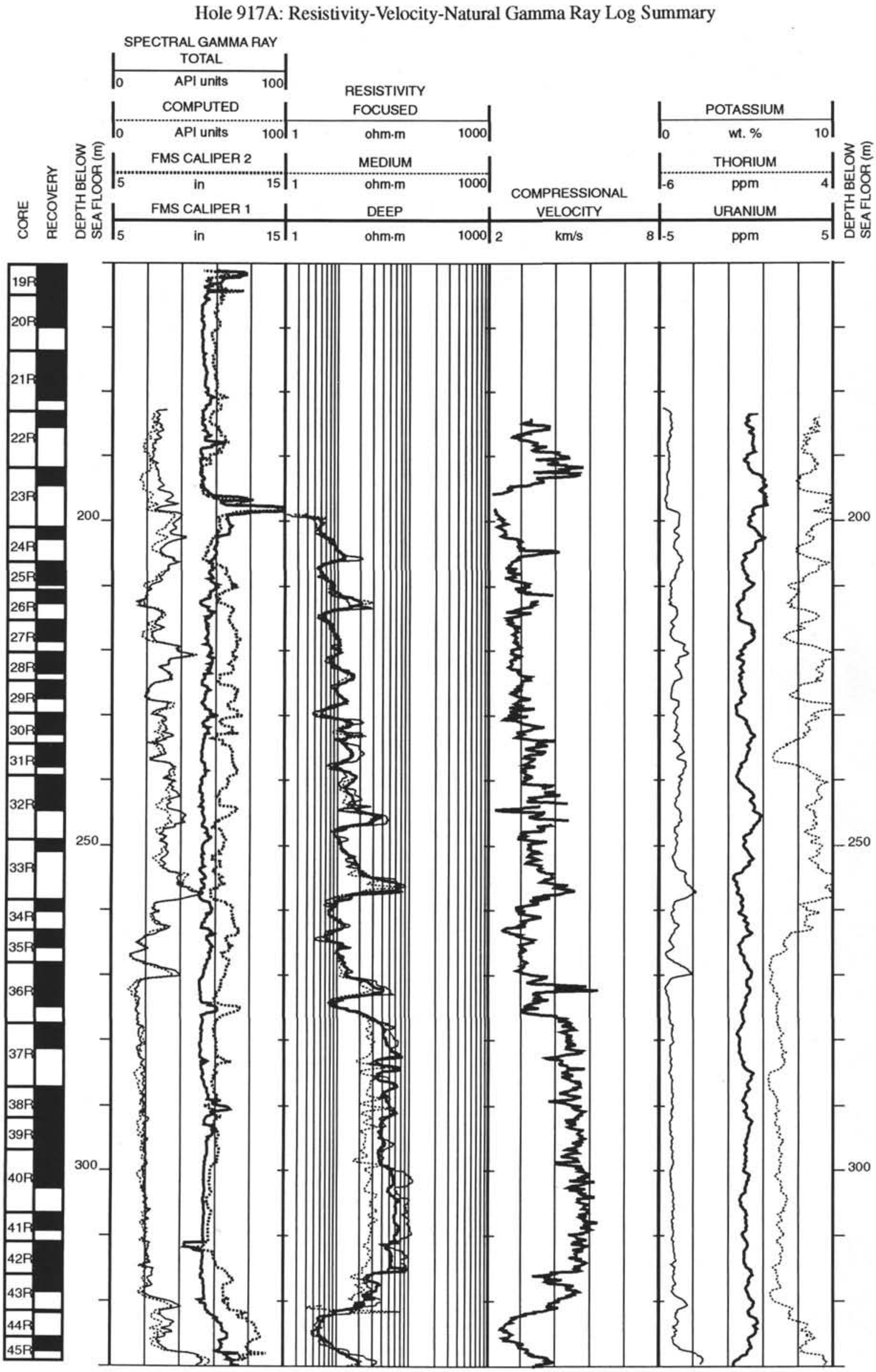
Hole 917A: Resistivity-Velocity-Natural Gamma Ray Log Summary
CORE
RECOVERY
DEPTH BELOW SEA FLOOR (m)
SPECTRAL GAMMA RAY
TOTAL
0 API units 100
COMPUTED
0 API units 100
FMS CALIPER 2
5 in 15
FMS CALIPER 1
5 in 15
RESISTIVITY
FOCUSED
1 ohm-m 1000
MEDIUM
1 ohm-m 1000
DEEP
1 ohm-m 1000
COMPRESSIONAL VELOCITY
2 km/s 8
POTASSIUM
0 wt. % 10
THORIUM
-6 ppm 4
URANIUM
-5 ppm 5
DEPTH BELOW SEA FLOOR (m)
19R
20R
21R
22R
23R
24R
25R
26R
27R
28R
29R
30R
31R
32R
33R
34R
35R
36R
37R
38R
39R
40R
41R
42R
43R
44R
45R
200
250
300

Hole 917A: Resistivity-Velocity-Natural Gamma Ray Log Summary (continued)

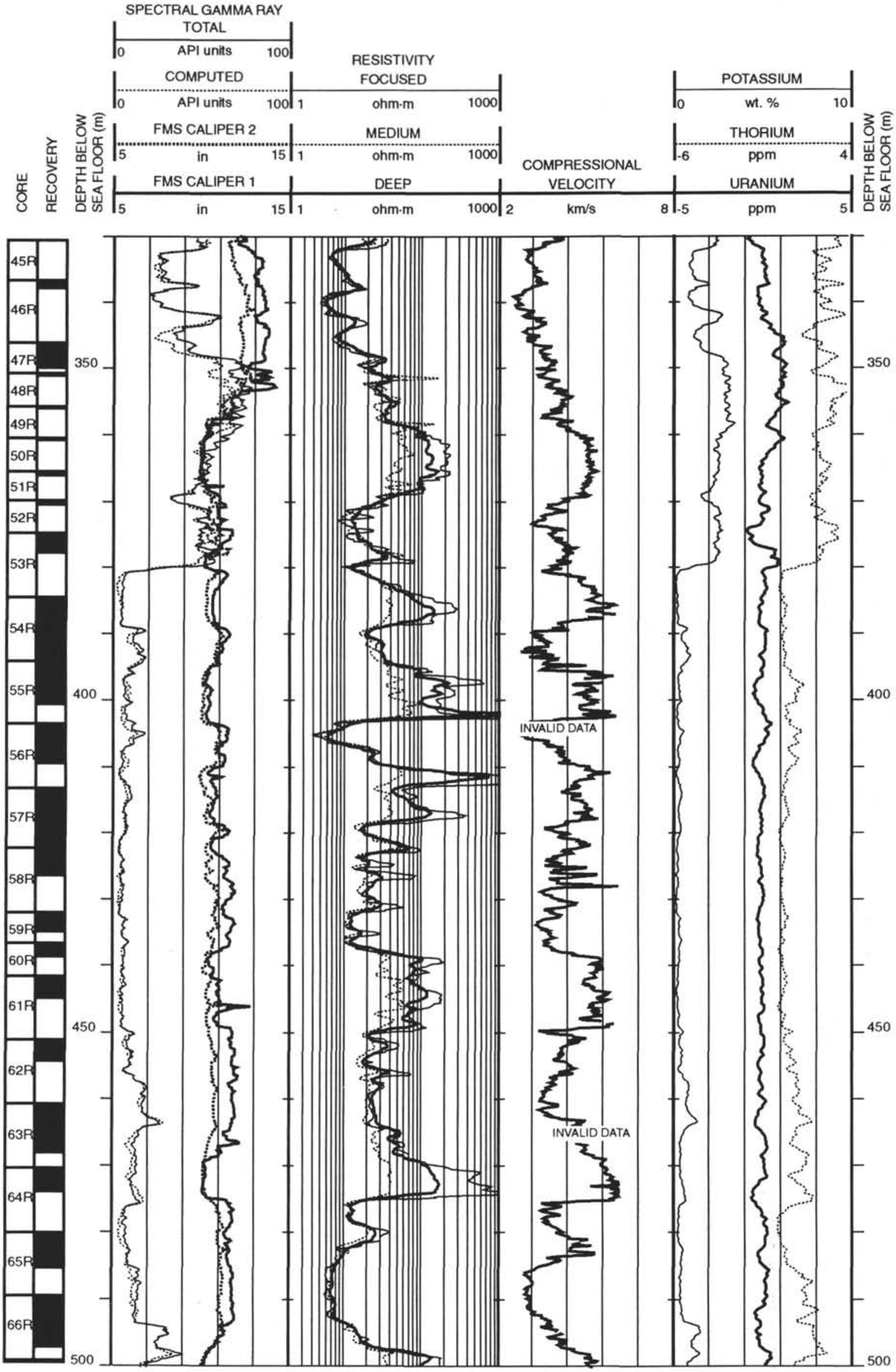

Hole 917A: Resistivity-Velocity-Natural Gamma Ray Log Summary (continued)

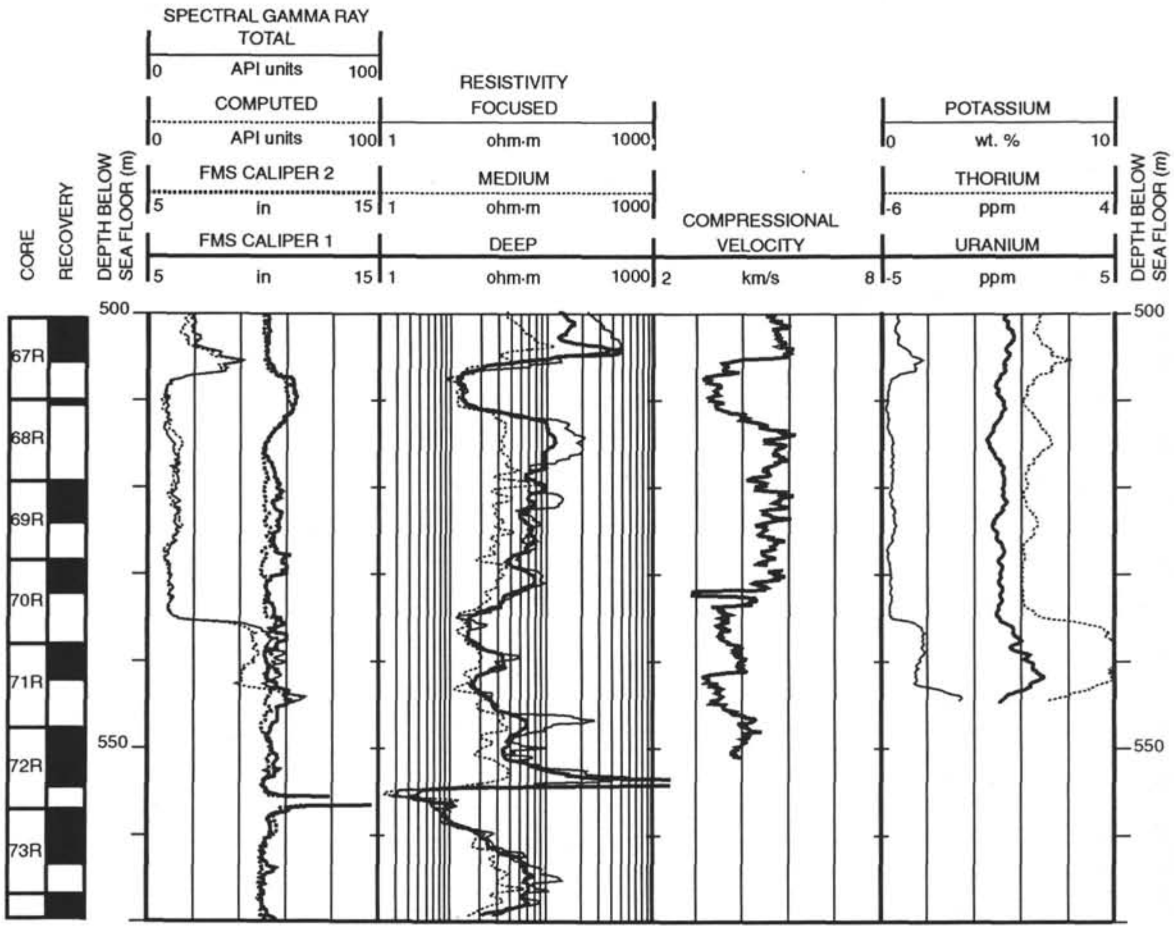

Hole 917A: Density-Natural Gamma Ray Log Summary

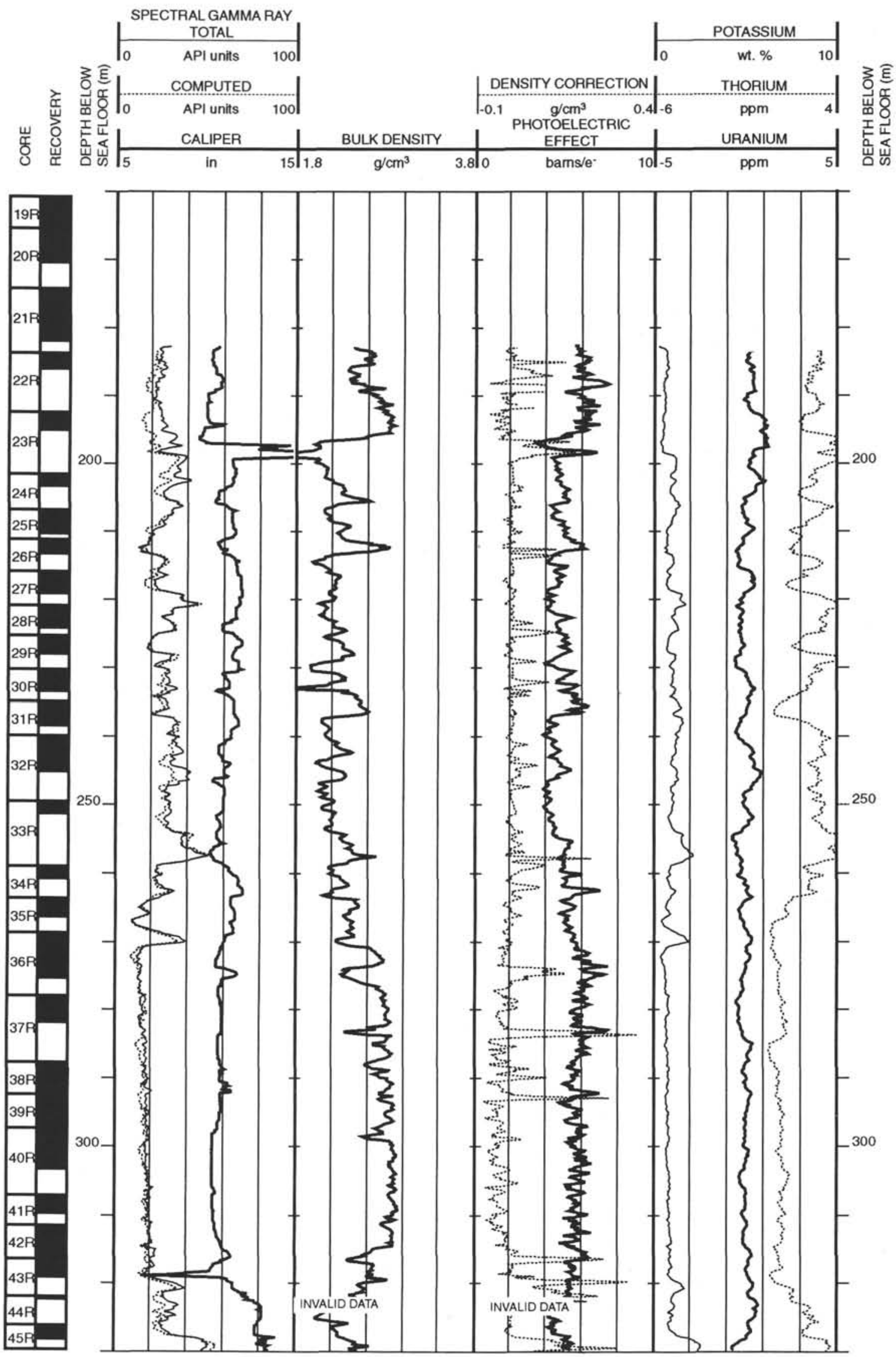

Hole 917A: Density-Natural Gamma Ray Log Summary (continued)

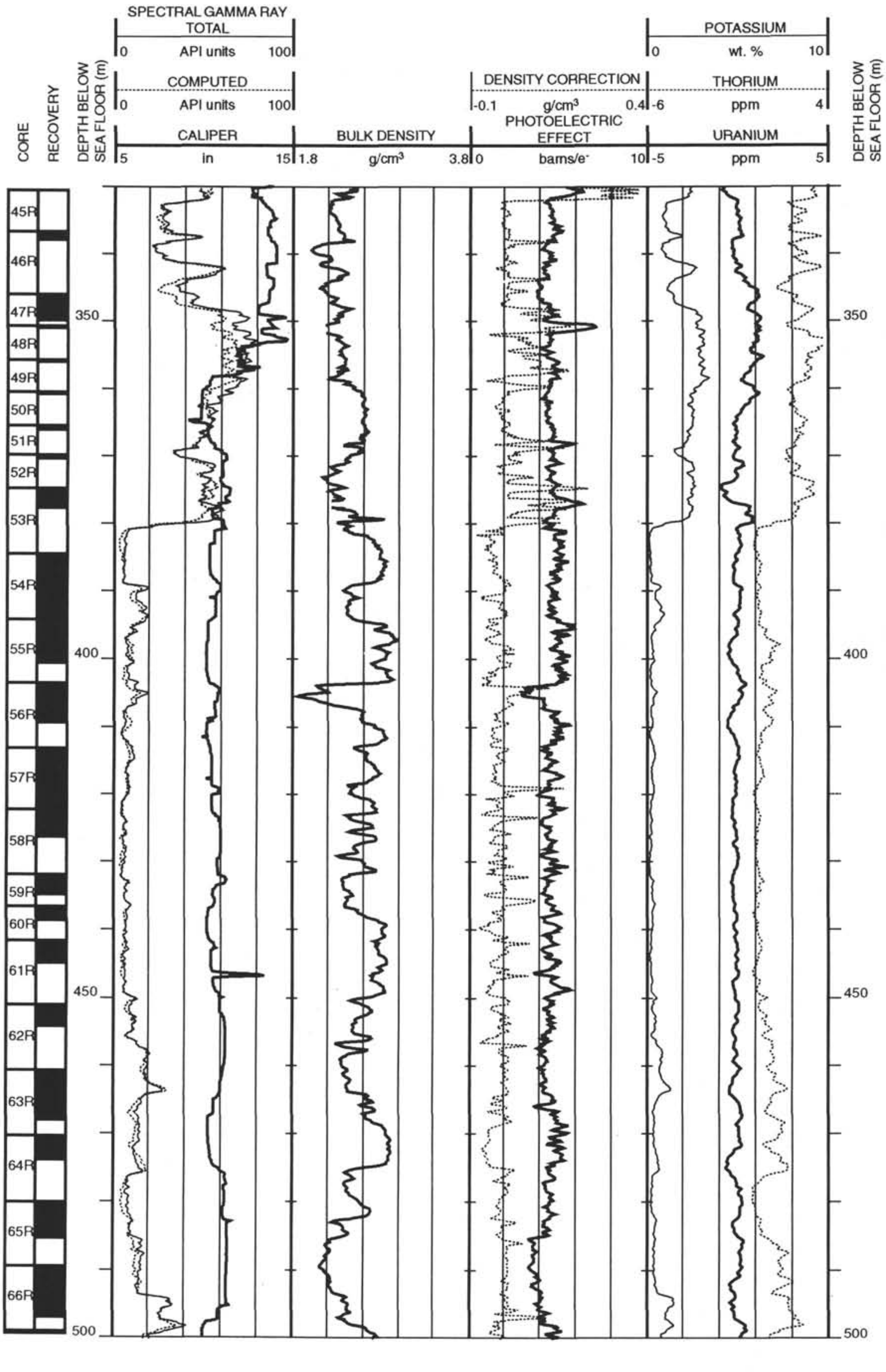

Hole 917A: Density-Natural Gamma Ray Log Summary (continued)